Theoretical Modelling of Electronic Properties of Bilayer Graphene-Based van der Waals Heterostructures

Leech, Damien

Award date:
2018

Awarding institution:
University of Bath

Theoretical modelling of electronic properties of bilayer graphene-based van der Waals heterostructures

Damien Jon Leech

A thesis presented for the degree of
Doctor of Philosophy

University Of Bath
Department Of Physics
June 2018

Declaration of authorship

I am the author of this thesis, and the work described therein was carried out by myself personally, with the exception of Chapters 3 and 4 that were worked on alongside J. J. P. Thompson, with pre-print text available for Chapter 4 at arXiv:1802.08100 - the level of contribution per project is defined more precisely at the beginning of these two chapters.

Damien Leech

Acknowledgements

I would first like to thank my supervisor Dr. Marcin Mucha-Kruczyński, without whom this work would not have been possible and who spent countless, tireless hours explaining both the minutiae and the very basics. Additionally, I would like to thank to the group that emerged around him; Josh 'fried eggs and gravy' Thompson, Aitor 'funky, not fancy' Garcia-Ruiz and Surani 'Subroni' Gunasekera, for their help and support. And to Dr. Daniel Wolverson, who sparked my interest in the topic in the first place.

I would also like to thank Jon and Lorraine Leech, my extended family and Chris and Teresa Lovell for their support throughout my PhD. And, last but definitely not least, a huge thanks to my finacée Hannah for her endless help and support.

Dedicated in loving memory of Brian O'Rourke.

Abstract

Following the successful isolation of a continuously growing number of layered materials in monolayer forms, these can now be assembled into stacks, referred to as van der Waals heterostructures. In this thesis, we investigate theoretically the electronic properties of heterostructures based on bilayer graphene, two coupled layers of carbon. We first study the minibands of bilayer graphene placed on a semiconducting substrate with a unit cell about, but not exactly, three times larger than that of graphene. While the former introduces asymmetry in the distribution of the electronic wave function between the layers and opens a band gap in the electronic spectrum, the latter generates a long wavelength moiré perturbation that couples states in inequivalent graphene Brillouin zone corners. We show that, depending on the details of the moiré perturbation, the miniband structure can be tuned to a situation where a single narrow miniband is separated from the rest of the spectrum by small gaps. We then discuss electron tunneling between bilayer and monolayer graphene across a hexagonal boron nitride barrier in the presence of a strong perpendicular magnetic field. We demonstrate that in such a device, valley-polarization close to unity can be produced in fields of order 1 T. Finally, we discuss electron transport in a van der Waals tunnelling transistor in which the electronic density of states in one of the electrodes has been modulated by a superlattice perturbation. Using the example of twisted bilayer graphene and a similar system of monolayer graphene on hexagonal boron nitride, we show that negative differential resistance is possible in such transistors as a consequence of the moiré-induced changes in the density of states and without the need of momentum conserving tunnelling.

Table of Contents

1 Introduction to Graphene & van der Waals Heterostructures 1
1.1 Physics in Flatland . . . 2
1.1.1 Graphene & 2DACs . . . 2
1.1.2 Bilayer Graphene . . . 2
1.1.3 van der Waals Heterostructures . . . 3
1.1.4 Thesis Outline . . . 4
1.2 The Tight-Binding Model of Monolayer and Bilayer Graphene . . . 6
1.2.1 Monolayer Graphene . . . 6
1.2.2 Bands In The Vicinity Of the Valley . . . 11
1.2.3 Bilayer Graphene . . . 12
1.2.4 Two-Band Bilayer Graphene Hamiltonian . . . 16
1.3 Moiré Patterns & Superlattices . . . 18
1.3.1 Twisted Bilayer Graphene . . . 20
1.3.2 Monolayer Graphene on hBN . . . 21
1.3.3 Bilayer Graphene on hBN . . . 25
1.3.4 Monolayer Graphene on an Almost Commensurate $\sqrt{3}\times\sqrt{3}$ Substrate . . . 26

2 Bilayer graphene on an almost commensurate $\sqrt{3}\times\sqrt{3}$ substrate 29
2.1 Introduction . . . 30
2.2 Electronic Hamiltonian . . . 32
2.3 Effective Hamiltonian at High-Symmetry Points . . . 36
2.3.1 μ Point . . . 37
2.3.2 γ Point . . . 38
2.3.3 κ Point . . . 39
2.4 Description of Matlab Procedure for Calculation of Dispersion . . . 41
2.4.1 Energy Bands . . . 41
2.4.2 Density Of States . . . 43
2.5 Miniband Spectrum . . . 43

2.6 Summary . . . 46
2.A Superlattice Periodicities for Graphene on Incommensurate $\sqrt{3}\times\sqrt{3}$ Substrate . . . 49
2.B Alternative Substrates . . . 50
2.C Closing the Central Gap . . . 52

3 Valley-polarised tunnelling current in a vertically stacked MLG-hBN-BLG heterostructure 54
3.1 Introduction . . . 55
3.2 Device Setup . . . 55
3.3 Electronic Structure in a Perpendicular Magnetic Field . . . 58
3.3.1 Monolayer . . . 58
3.3.2 Bilayer . . . 60
3.4 Tunnelling Current . . . 62
3.5 Description of Matlab Procedure for Current Calculation . . . 67
3.6 Tunnelling Current & Polarisation . . . 69
3.6.1 B = 4T . . . 69
3.6.2 B = 1T . . . 72
3.6.3 Rotational Misalignment . . . 74
3.7 Summary . . . 76
3.A Inclusion of Top Gate, $V_t \neq 0$V . . . 77

4 Negative differential resistance in van der Waals heterostructures due to moiré-induced van Hove singularities 79
4.1 Introduction . . . 80
4.2 Generic Device Model . . . 81
4.2.1 Device Schematic . . . 81
4.2.2 Tunnelling Current & Electrostatics . . . 83
4.3 Highly-Aligned Graphene/hBN . . . 84
4.4 Twisted Bilayer Graphene . . . 87
4.5 Summary . . . 90
4.A Density Of States Probe . . . 91

5 Summary 94

Abbreviations

2DACs Two-Dimensional Atomic Crystals

BZ Brillouin Zone

DOS Density Of States

hBN hexagonal Boron Nitride

LL Landau Level

NDR Negative Differential Resistance

sBZ Superlattice Brillouin Zone

tBLG Twisted Bilayer Graphene

TMDs Transition Metal Dichalocogenides

vdW van der Waals

vHS van Hove Singularity

Chapter 1

Introduction to Graphene & van der Waals Heterostructures

1.1 Physics in Flatland

1.1.1 Graphene & 2DACs

As with many discoveries within the scientific world, the underlying premise of 2D materials had been discussed prior to the actual isolation of such materials, due to the interest in bulk layered materials such as graphite. In 1917, Hull [1], using x-ray analysis data, suggested that graphite was a layered structure comprised of 'building blocks' of carbon atoms in hexagonal arrangements that were vertically periodic with every bilayer - a form that was later finalised by Bernal [2] in 1924. The unusual gapless semi-conductor electronic properties that became a focal point of graphene were discussed as early as 1947 by Wallace [3], in which he utilised one of these single layer constructs in order to probe the properties of the electronic structure of the full layered material, providing the basis for later work on the band structure of graphite [4, 5]. However, it was believed that two-dimensional, semi-metallic materials would be inherently unstable when isolated [6] and this became the limit of the work undertaken in this area. Alongside this, this area of the field lost some allure with the discovery of more immediately interesting carbon allotropes, such as fullerenes [7] and nanotubes [8].

Yet in 2004, graphene was isolated unexpectedly alongside other few-layer graphene constructs using simple mechanical exfoliation techniques [9, 10] - work that led to the pairing of A. Geim and K. Novoselov being awarded the Nobel Prize in 2010. Graphene was found to be surprisingly stable, leading to a profusion of work describing the mechanical, electronic and optical peculiarities of the material, including the aforementioned linear electronic dispersion, high flexibility [11] and visible spectrum absorption uniformity [12]. This also had the knock-on effect of reigniting interest in many other bulk layered materials for the production of Two-Dimensional Atomic Crystals (2DACs), including hexagonal Boron Nitride (hBN) [10, 13], Transition Metal Dichalocogenides (TMDs) [14, 15] and silicene [16].

1.1.2 Bilayer Graphene

Though much of the spotlight within 2DACs has lied solely on the properties and linear band structure of monolayer graphene (MLG), bilayer graphene (BLG) provides its own selection of interesting physical properties that can be exploited for device purposes, particularly under the application of external fields.

Comprised of two monolayer sheets and typically stacked in an AB (Bernal) stacking formation, the coupling between the layers of bilayer transforms the

electronic structure from the distinct linear cones of the monolayer system to a similarly-gapless but quadratic form [17, 18]. It also shares many properties with its monolayer counterpart, such has high mobilities ($4 \times 10^4 \mathrm{cm}^2\mathrm{V}^{-1}\mathrm{s}^{-1}$) [13] and a Young's modulus of 0.872TPa [19]. This gapless quadratic spectrum, however, can become gapped through the breaking of inversion symmetry within the system, attained through affecting the on-site energies of each layer differently and most easily achieved via the introduction of a perpendicular electric field to the bilayer. Not only does this open a gap in the spectrum, but the size of the gap can be controlled via tuning of the electric field strength [20]. In the case of MLG instead, gap opening in a similar manner is more complicated and requires an in-plane periodic potential that affects the on-site energies of each sublattice atom differently, usually via precise matching with substrate sites [21].

In a similar manner, the introduction of a magnetic field perpendicularly to the bilayer can be used to manipulate the band structure. The structure exhibits an anomalous quantum Hall effect behaviour and the energy bands, as in the monolayer system, become quantised, distinct Landau Level (LL) that are eightfold degenerate at the neutrality point [22, 23], as opposed to the fourfold degeneracy seen in the monolayer. At this low energy point as well, the electrons become spatially polarised between the two layers in terms of valley, a quantum number in graphene that assigns electrons to distinct low-energy corners of the Brillouin zone and can be conserved and manipulated in a similar manner to spin. Additionally, the combination of both magnetic and electric fields can be used to lift the energy degeneracy of the two valleys, again with a magnitude controlled by the strength of the electric field.

Altogether, bilayer graphene is a material that maintains many of the interesting features of the monolayer material, whilst introducing additional degrees of freedom to probe. This is especially true when considering stacked structures that utilise perturbations of the electronic structure in order to probe novel phenomena and thus we use it as a primary component in many of the device structures we suggest.

1.1.3 van der Waals Heterostructures

Since the advent of graphene and other two-dimensional atomic crystals, the vertical layering of these materials into van der Waals (vdW) has remained an important point of interest [24]. This involves precise vertical stacking of these 2D materials into thin devices that span large numbers of atoms in plane, but only a handful out of plane. Many structures have been proposed [25] that exploit

and manipulate the individual properties of the constituent layers via; interactions between neighbouring layers, the reduction of this interaction with increasing distance, the ordering of materials within the stack, the introduction of defects or adatoms to the system, the application of external fields, superlattice formation, layer strain and the rotational misalignment of the crystallographic axes with respect to one another, amongst other approaches.

The most common example of such a construction is that of a simple graphene and hexagonal boron nitride bilayer, in which the flatness and lack of charge impurities in the substrate provide an ideal environment to preserve the electronic properties of the graphene [13]. Previously, graphene sheets were commonly placed onto SiO_2 substrates that directly negatively affected the electronic properties [26] and flatness [27] of the graphene sheets. An unforeseen side effect of this simple graphene and hBN substrate system was the introduction of a moiré superlattice potential felt by the graphene system due to a mismatch of 1.8% in the lattice constants of the two hexagonal materials [28, 29, 30]. This leads to a larger-scale hexagonal potential on the order of nano-metres felt by the electrons within the graphene, known as a moiré pattern, that folds and perturbs the energy bands into a much smaller Brillouin zone and can be further modified by rotational misalignment of the two crystalline directions. These superlattice interactions represent one powerful facet in the construction of van der Waals heterostructures that aim to tune the properties of the individual layers and an understanding of their effects allow us to hypothesise more complicated layered devices.

1.1.4 Thesis Outline

Firstly, we discuss the key background theory needed within the rest of the thesis, including the construction of a tight-binding description of the electronic structure of both monolayer and bilayer graphene, models that describe purely the low-energy energy bands of such structures and the modelling of a handful of simple moiré patterned superlattices, made from mismatched 2DAC bilayers, and their band structure. We then utilise these ideas to discuss a relatively simple 'graphene and substrate' system comprised of BLG on an almost commensurate $\sqrt{3} \times \sqrt{3}$ lattice substrate in the presence of an external electric field. We highlight how those individual perturbations affect the band structure of the bilayer and predict a highly isolated mini-band separated on either side by band gap when in combination, under general conditions. Chap. 3 expands upon a family of graphene-based vertical tunnelling transistor systems that display rich I-V characteristics in devices a handful of layers thick. Through construction of a

BLG/hBN/MLG stack in a magnetic field, we show the tunnelling electrons can be tuned not only in magnitude but in polarisation of their valley number using magnetic field strength, tunnelling potentials and rotational mismatch between the electrodes. Chap. 4 begins from the same vertical tunnelling setup, cutting the magnetic field, and replacing the bilayer electrode with one of two bilayer superlattice electrodes, either a twisted bilayer or a graphene-aligned hexagonal boron nitride electrode. This is in order to show how the appearance of van Hove Singularity (vHS) in the reconstruction of Density Of States (DOS) of superlattice materials can be exploited to induce Negative Differential Resistance (NDR), by abusing the flattening of bands and opening of mini-gaps that are typical of such a structure, with a result that should be generalisable across many other superlattice electrodes. A summary of the work and some ideal future reasearch is provided in Chap. 5.

1.2 The Tight-Binding Model of Monolayer and Bilayer Graphene

1.2.1 Monolayer Graphene

Throughout this thesis we use a tight binding formulation, in order to describe the electronic structure of graphene, which underpins all of the following work. This assumes electrons in the material belong to particular atoms and adjacent atoms have minimal overlap in their atomic orbitals and thus minimal interactions. It requires an understanding of not only the electronic properties of the individual atoms, but also the geometry of the system and therefore for each individual few-layer graphene construct we take care to describe them structurally, before discerning a tight-binding Hamiltonian that describes the low-energy band structure of each.

Graphene itself is defined as a single atomic layer of graphite, although we consider many variations on this few-layer graphite construct. It is comprised of a honeycomb lattice of carbon atoms, with two atomic sites per unit cell, each belonging to a sublattice labelled A or B, and a set of rhombohedral primitive lattice vectors, as seen in Fig. 1.1a. These two distinct sublattices are considered non-equivalent atomic sites, as they cannot be connected by these primitive lattice vectors, that are written as [31]

$$\boldsymbol{a}_1 = a\left(\frac{1}{2}, \frac{\sqrt{3}}{2}\right), \boldsymbol{a}_2 = a\left(-\frac{1}{2}, \frac{\sqrt{3}}{2}\right), \tag{1.1}$$

where the lattice constant has value $a = 2.46\text{Å}$ and defines the distance between two atoms of the same sublattice. For an arbitrary A sublattice atom, the three neighbouring B sublattice atoms can instead be reached by

$$\boldsymbol{\delta}_1 = \frac{a}{\sqrt{3}}(0, 1), \quad \boldsymbol{\delta}_2 = \frac{a}{\sqrt{3}}\left(\frac{\sqrt{3}}{2}, -\frac{1}{2}\right), \quad \boldsymbol{\delta}_3 = \frac{a}{\sqrt{3}}\left(-\frac{\sqrt{3}}{2}, -\frac{1}{2}\right). \tag{1.2}$$

Out of plane, individual layers of graphene in a multi-layer system are separated by 3.35Å [32, 33]. Provided a perfect Bernal stacking formation (this will be discussed in more depth later in this chapter), all of these distances remain constant with an increasing number of adjacent graphene layers [34].

In reciprocal space, the Brillouin zone is also hexagonal, with reciprocal lattice vectors that satisfy $\boldsymbol{b}_i \cdot \boldsymbol{a}_j = 2\pi\delta_{ij}$, such that

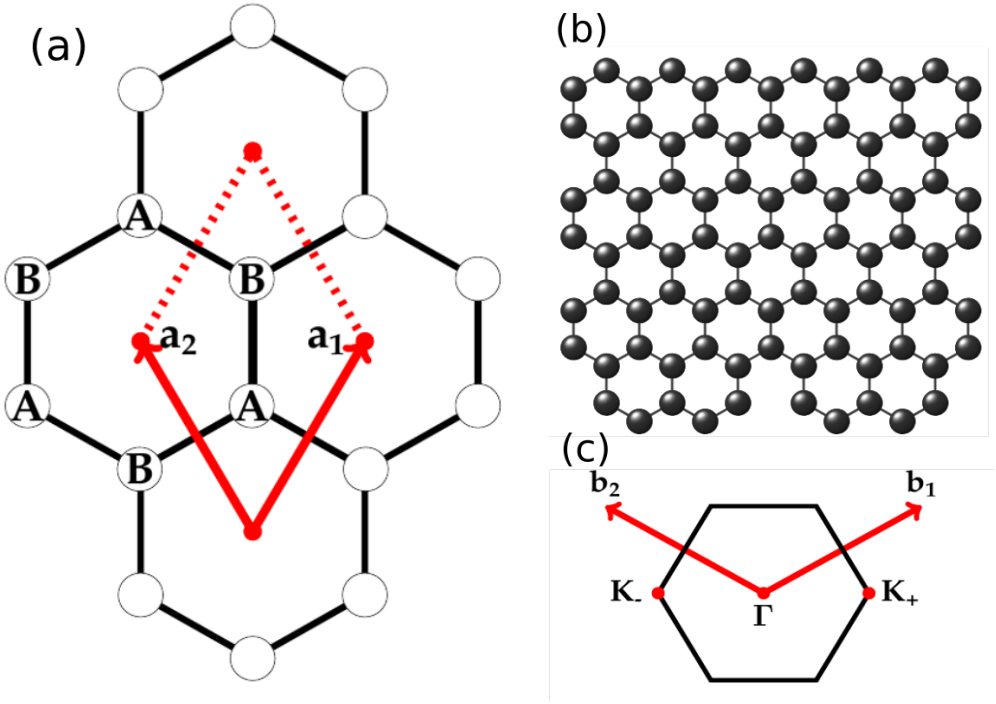

Figure 1.1: (a) Graphene lattice in real space, displaying unit cell vectors and hexagonal unit cell comprising of two inequivalent atomic sites, A and B. (b) A larger scale representation of the unit cell and the periodicity that provides. (c) The graphene Brillouin zone and corresponding reciprocal lattice vectors.

$$\boldsymbol{b}_1 = \frac{2\pi}{a}\left(1, \frac{1}{\sqrt{3}}\right), \boldsymbol{b}_2 = \frac{2\pi}{a}\left(-1, \frac{1}{\sqrt{3}}\right), \tag{1.3}$$

within which there exists two inequivalent corners of the Brillouin zone, denoted by $\boldsymbol{K}_\pm$ in Fig. 1.1c, that define the valleys of the system with index $\xi = \pm 1$ and sit at

$$\boldsymbol{K}_\xi = \left(\xi\frac{4\pi}{3a}, 0\right). \tag{1.4}$$

The tight binding approach depends on solving the eigenvalue problem of the material Hamiltonian, in a basis of the individual atomic orbitals that comprise the unit cell. Each carbon atom contains six electrons in total, only four of which are valence electrons. These four valence electrons occupy the $2s$ and the $2p_{x,y}$ orbitals, within which the $2s$ and the in-plane $2p$ orbitals are hybridized to form the three C-C bonds at 120° that construct the honeycomb structure. The remaining $2p_z$ orbital is out-of-plane and forms π bonds with adjacent $2p_z$ orbitals, which alone can describe the electronic structure close to the Fermi level and provides the one electron per atomic site that the tight-binding model uses. Hence, our tight-binding model is described by a 2×2 matrix, alluding to the single electron per

atom within the unit cell.

Considering our graphene system to be infinite and periodic, such that there is no translational variance between unit cells, the wave function $\psi(\boldsymbol{r})$ may be described by

$$\hat{\boldsymbol{T}}_{\boldsymbol{a}_i}\psi(\boldsymbol{r}) = e^{i\boldsymbol{k}\cdot\boldsymbol{a}_i}\psi(\boldsymbol{r}), \tag{1.5}$$

where $\hat{\boldsymbol{T}}_{\boldsymbol{a}_i}$ is a translation operator that links the neighbouring unit cell via Eq. (1.1) and $\boldsymbol{k}$ represents the wave vector. As such, the system may be described by Bloch functions $\Phi_j(\boldsymbol{k}, \boldsymbol{r})$ of form

$$\Phi_j(\boldsymbol{k}, \boldsymbol{r}) = \frac{1}{\sqrt{N}} \sum_{i=1}^{N} e^{i\boldsymbol{k}\cdot\boldsymbol{R}_{j,i}} \phi_j(\boldsymbol{r} - \boldsymbol{R}_{j,i}), \tag{1.6}$$

where $\boldsymbol{R}$ defines the atomic position, N is the number of unit cells labelled $i = 1, ..., N$ and ϕ, in our case, is the atomic wave function of the $2p_z$ orbital in a state j that labels the two unit cell atoms, A and B.

The general electronic wave function can be represented as a linear superposition of these Bloch functions [31, 35]

$$\psi_n(\boldsymbol{k}, \boldsymbol{r}) = \sum_{l=1}^{n} C_{j,l}\Phi_j(\boldsymbol{k}, \boldsymbol{r}), \tag{1.7}$$

where $C_{j,l}$ are coefficients of expansion and n is the number of atoms within the unit cell, such that $n = 2$.

In order to construct the graphene Hamiltonian, we use a nearest neighbour approximation utilising the π states only. As such we require a description of the couplings between the sites using the two Bloch functions previously described in Eq. (1.6)

$$\hat{\boldsymbol{H}}_{j,j'} = \langle \Phi_j | \, \hat{\boldsymbol{H}}_{\mathrm{MLG}} \, | \Phi_{j'} \rangle \,, \tag{1.8}$$

where the apostrophe notation represents the initial state property and the lack of an apostrophe represents the final state property. We can therefore feasibly construct an $n \times n$ sized Hamiltonian, where, again, we use $n = 2$.

The diagonal elements, using the A sublattice as an example, can therefore be written as [35]

$$\hat{\boldsymbol{H}}_{AA} = \frac{1}{N} \sum_{\boldsymbol{R}} \sum_{\boldsymbol{R'}} \exp\left(i\boldsymbol{k} \cdot (\boldsymbol{R}'_A - \boldsymbol{R}_A)\right) \langle \phi_A(\boldsymbol{r} - \boldsymbol{R}_A) | \, \hat{\boldsymbol{H}}_{\mathrm{MLG}} \, | \phi_A(\boldsymbol{r} - \boldsymbol{R}'_A) \rangle \,.$$

The maximum contribution for this element arises from the case where $\boldsymbol{R} = \boldsymbol{R'}$, therefore we can state that

$$\hat{\boldsymbol{H}}_{AA} \approx \frac{1}{N} \sum_{\boldsymbol{R}} \langle \phi_A(\boldsymbol{r} - \boldsymbol{R}_A)| \, \hat{\boldsymbol{H}}_{\text{MLG}} \, |\phi_A(\boldsymbol{r} - \boldsymbol{R}_A)\rangle \, .$$

As we measure the energy relative to this onsite energy, we can therefore also set $\langle \phi_A(\boldsymbol{r} - \boldsymbol{R}_A)| \, \hat{\boldsymbol{H}}_{\text{MLG}} \, |\phi_A(\boldsymbol{r} - \boldsymbol{R}_A)\rangle = 0$, zeroing this diagonal element. A similar treatment occurs for $\hat{\boldsymbol{H}}_{BB}$ due to the identical structure it holds, producing an identical solution.

The off diagonal elements represent the hopping between the A and B sublattice and are described by [35]

$$\hat{\boldsymbol{H}}_{BA} = \frac{1}{N} \sum_{\boldsymbol{R}} \sum_{\boldsymbol{R'}} \exp\left(i\boldsymbol{k} \cdot (\boldsymbol{R}'_B - \boldsymbol{R}_A)\right) \langle \phi_A(\boldsymbol{r} - \boldsymbol{R}_A)| \, \hat{\boldsymbol{H}}_{\text{MLG}} \, |\phi_B(\boldsymbol{r} - \boldsymbol{R}'_B)\rangle \, .$$

Again the largest contribution occurs when the distances between the atoms are minimised, in other words the three nearest-neighbour separations defined in Eq. (1.2) with index $l = 1, ..., 3$.

$$\hat{\boldsymbol{H}}_{BA} \approx \frac{1}{N} \sum_{\boldsymbol{R}} \sum_{l=1}^{3} \exp\left(i\boldsymbol{k} \cdot \left(\boldsymbol{R}'_{B,l} - \boldsymbol{R}_A\right)\right) \langle \phi_A(\boldsymbol{r} - \boldsymbol{R}_A)| \, \hat{\boldsymbol{H}}_{\text{MLG}} \, |\phi_B(\boldsymbol{r} - \boldsymbol{R}'_{B,l})\rangle \, .$$

As all three nearest neighbours are the same distance away, the matrix element is independent in magnitude of the index l and we therefore set it to a constant $\gamma_0 = -\langle \phi_A(\boldsymbol{r} - \boldsymbol{R}_A)| \, \hat{\boldsymbol{H}}_{\text{MLG}} \, |\phi_B(\boldsymbol{r} - \boldsymbol{R}'_{B,l})\rangle$ where $\gamma_0 \approx 3\text{eV}$ [3].

$$\hat{\boldsymbol{H}}_{BA} \approx -\frac{\gamma_0}{N} \sum_{\boldsymbol{R}} \sum_{l=1}^{3} \exp\left(i\boldsymbol{k} \cdot \left(\boldsymbol{R}'_{B,l} - \boldsymbol{R}_A\right)\right) = -\gamma_0 \sum_{l=1}^{3} \exp\left(i\boldsymbol{k} \cdot \boldsymbol{\delta}_l\right) = -\gamma_0 f(\boldsymbol{k}).$$

$f(\boldsymbol{k})$ describes the hopping to the three neighbouring opposite sublattice atoms via the $\boldsymbol{\delta}_l$ vectors [31]

$$f(\boldsymbol{k}) = \sum_{l=1}^{3} e^{i\boldsymbol{k}\cdot\boldsymbol{\delta}_l} = \exp\left(\frac{ik_y a}{\sqrt{3}}\right) + 2\exp\left(-\frac{ik_y a}{2\sqrt{3}}\right) \cos\left(\frac{k_x a}{2}\right). \tag{1.9}$$

In all, this produces [35]

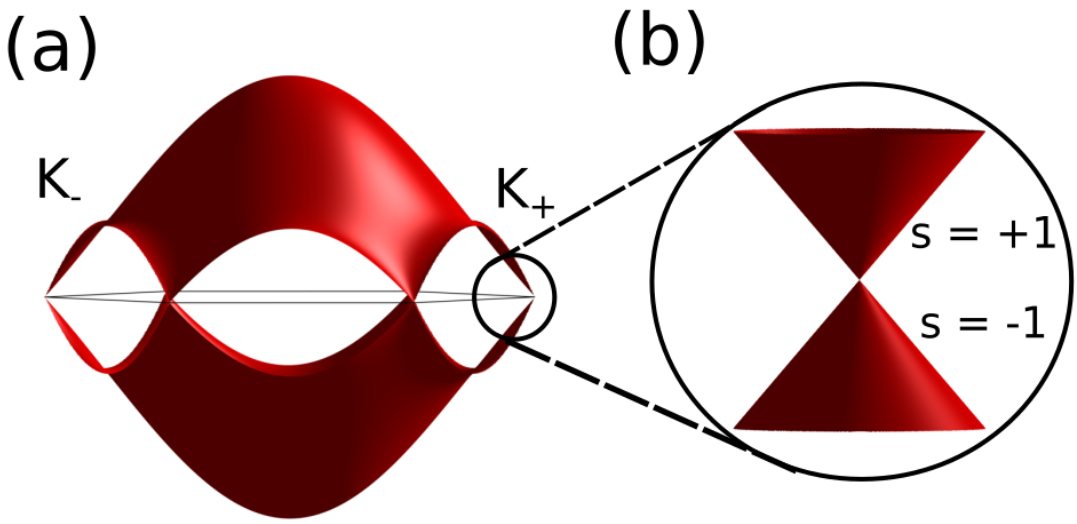

Figure 1.2: (a) Electronic structure throughout the Brillouin zone, displaying the linear dependence found at the zone corners or valleys. (b) Focus on the low-energy linear spectrum, that we primarily utilise.

$$\hat{\boldsymbol{H}}_{\mathrm{MLG}} = \begin{pmatrix} \hat{\boldsymbol{H}}_{AA} & \hat{\boldsymbol{H}}_{BA} \\ \hat{\boldsymbol{H}}_{AB} & \hat{\boldsymbol{H}}_{BB} \end{pmatrix} . = \begin{pmatrix} 0 & -\gamma_0 f(\boldsymbol{k}) \\ -\gamma_0 f(\boldsymbol{k})^\dagger & 0 \end{pmatrix} . \tag{1.10}$$

The full energy band dispersion throughout the Brillouin Zone (BZ) can be seen in Fig. 1.2a, using the energy equation obtained from diagonalisation of the Hamiltonian above

$$E_s = s\gamma_0 |f(\boldsymbol{k})|, \quad s = \pm 1. \tag{1.11}$$

The energy band structure changes noticeably throughout the BZ - at the centre Γ the bands are split by $\pm 3\gamma_0$ and the corners of the Brillouin zone are inhabited by Dirac cones with a linear dispersions that touch at zero energy, leaving no gap, seen more easily in Fig. 1.2b.

By substitution of the valley point $\boldsymbol{K}$ of the BZ into the coupling in Eq. (1.9), we note it vanishes as

$$f(\boldsymbol{k}) = e^0 + e^{i\frac{2\pi}{3}} + e^{-i\frac{2\pi}{3}} = 0, \tag{1.12}$$

suggesting there is no coupling between the sublattices at this point and an inherent inequivalence. Since they are identical in periodicities however, they support a degeneracy at this point in the BZ.

1.2.2 Bands In The Vicinity Of the Valley

We have given a description of the energy bands of monolayer graphene through the BZ defined by the vectors in Eq. (1.3). However, if we shift our perspective to that around the aforementioned $\boldsymbol{K}_\xi$ points of the Brillouin zone, as seen in Fig. 1.2, we can focus on a low-energy description of the graphene and reduce our Hamiltonian and thus wave functions to much simpler forms, as $f(\boldsymbol{K}_\xi) = 0$. This suggests that the sublattices are entirely uncoupled here and are degenerate in energy. Expanding around this point and taking into account the two distinct valleys, we use a momentum measured from the Dirac point

$$\boldsymbol{p} = \hbar\boldsymbol{k} - \hbar\boldsymbol{K}_\xi. \tag{1.13}$$

Using Eq. (1.9) as the starting point and the momentum term above, we find that [35]

$$f(\boldsymbol{k}) = \exp\left(\frac{ip_y a}{\sqrt{3}}\right) + 2\exp\left(-\frac{ip_y a}{2\sqrt{3}}\right)\cos\left(\frac{p_x a}{2\hbar} + \frac{\xi 2\pi}{3}\right).$$

As $\cos(A+B) = \cos(A)\cos(B) - \sin(A)\sin(B)$ and $\cos(x) \approx 1$ and $\sin(x) \approx x$, for small values of x, we can expand the last term as

$$\cos\left(\frac{p_x a}{2\hbar} + \frac{\xi 2\pi}{3}\right) = \frac{1}{2}\cos\left(\frac{p_x a}{2\hbar}\right) - \xi\frac{\sqrt{3}}{2}\sin\left(\frac{p_x a}{2\hbar}\right) = \left(-\frac{1}{2} - \frac{\xi\sqrt{3}p_x a}{4\hbar}\right).$$

Combining with an expansion of the exponential terms, $\exp(x) \approx 1 + x + ...$, Eq. (1.9) becomes

$$f(\boldsymbol{k}) = \left(1 + \frac{ip_y a}{\sqrt{3}}\right) + 2\left(1 - \frac{ip_y a}{2\sqrt{3}}\right)\left(-\frac{1}{2} - \frac{\xi\sqrt{3}p_x a}{4\hbar}\right).$$

Then we expand and approximate the coupling to purely linear terms, acceptable for energies around the K_ξ point where $\frac{pa}{\hbar} \ll 1$, producing

$$f(\boldsymbol{k}) \approx -\frac{\sqrt{3}a}{2\hbar}(\xi p_x - ip_y). \tag{1.14}$$

And similarly the Hamiltonian becomes purely the Dirac Hamiltonian, maintaining the basis of $\{\Phi_A, \Phi_B\}$, and reduces to

$$\hat{\boldsymbol{H}}_{\mathrm{MLG},\xi} = v\begin{pmatrix} 0 & \xi p_x - ip_y \\ \xi p_x + ip_y & 0 \end{pmatrix} = \begin{pmatrix} 0 & v\pi^\dagger \\ v\pi & 0 \end{pmatrix}, \tag{1.15}$$

in which we define the velocity as $v = \sqrt{3}a\gamma_0/2\hbar \approx 10^6 \text{ms}^{-1}$, $\pi = \xi p_x + ip_y = pe^{i\xi\varphi}$, φ as the polar angle of the momentum and p as simply the absolute of the momentum, that is measured with respect to the valley centre.

Solutions of the time-independent Schrödinger equation can be used to obtain solutions of the energies and wave functions of the system

$$\hat{\boldsymbol{H}}\psi = E\psi.$$

From which we can obtain the eigenvalues and states, for the monolayer graphene system, as

$$E_{\text{MLG}} = svp, \quad \psi_{\text{MLG}} = \frac{1}{\sqrt{2}} \begin{pmatrix} 1 \\ s\xi e^{i\xi\varphi} \end{pmatrix} e^{i\boldsymbol{k}\cdot\boldsymbol{r}}, \tag{1.16}$$

where $s = \pm 1$ and defines the band index, distinguishing between the conduction and valence bands. This produces a rotationally and electron-hole symmetric conical dispersion, that was previously isolated to regions surrounding the valley points. Again, these hold most significantly for low energies, as can be seen by the purely linear dispersion they describe, much like Fig. 1.2b.

1.2.3 Bilayer Graphene

Bilayer graphene refers to the vertical stacking of two monolayer graphene sheets. With the two sheets rotationally aligned, it manifests in two primary forms - AA and AB (Bernal) stacked. AA-stacked BLG consists of two layers with all atoms aligned vertically, such that every A and B sublattice atom is partnered and directly coupled with a respective A and B atom in the opposite layer. AB stacking, seen in Fig. 1.3, is more structurally stable [36] and refers to a stacking in which only one atom per layer is directly vertically adjacent to another, denoted as the A2 and B1 atoms, where the number simply defines the layer number. As such, in a nearest-neighbour description of the structure, the band structure is dominated by the effects of the in-plane coupling described in the monolayer case and the inter-layer coupling of these vertically adjacent atoms. As it is more stable and more commonly found in nature, it can be assumed any reference to bilayer graphene is that of a Bernal stacked formation.

As bilayer graphene is simply the stacking of two individual and parallel monolayer sheets with an interlayer separation of 3.35Å, see Fig. 1.3a and 1.3b, in the tight binding framework the Hamiltonian can be built using these individual components as the basis and constructing a transfer Hamiltonian between them. The primitive lattice vectors, lattice constant and reciprocal lattice vectors remain the

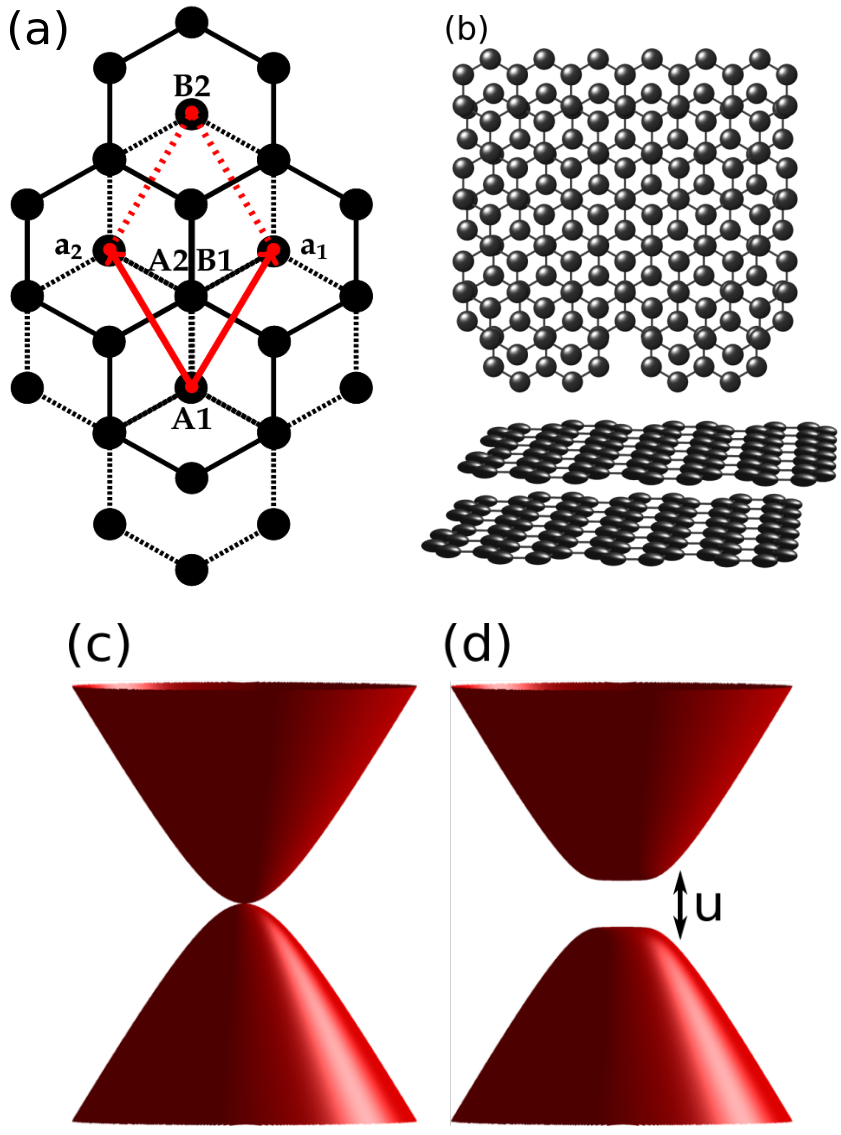

Figure 1.3: (a) Bilayer graphene unit cell, highlighting the differing layers using solid and dashed lines. The dimer state is highlighted by the overlapping B1 and A2 atoms that are vertically adjacent. (b) Real space larger-scale lattice, from both in and out of plane, displaying Bernal stacking and overall periodicity. (c) The two lowest energy bands, displaying the parabolic band structure around the valley point. (d) Band structure in the presence of an electric field perpendicular to the layers, displays the opening of a gap with a magnitude proportional to the strength of the field.

same as in the monolayer construction (with the addition of a z-axis vector spanning the two layers). As such the unit cell contains four atoms, now distinguished by sublattice (A and B) and layer (1 and 2), in a basis $\{\Phi_{A1}, \Phi_{B1}, \Phi_{A2}, \Phi_{B2}\}$, the Hamiltonian can be described in terms of the individual monolayer components with a coupling

$$\hat{\boldsymbol{H}}_{\mathrm{BLG}} = \begin{pmatrix} \hat{\boldsymbol{H}}_{\mathrm{MLG}} & \hat{\boldsymbol{H}}_{\mathrm{T}} \\ \hat{\boldsymbol{H}}_{\mathrm{T}}^{\dagger} & \hat{\boldsymbol{H}}_{\mathrm{MLG}} \end{pmatrix}. \tag{1.17}$$

The Bernal stacking formation as previously discussed, standard amongst nearly all grown and isolated graphene samples, means that for nearest neighbour interactions the only interlayer hopping we must consider is that between the B1 and A2 atoms that are directly vertically adjacent, with the coupling $\gamma_1 = 0.39\mathrm{eV}$. Known as the dimer state, due to the strong overlap of the electronic orbitals, these atoms influence the higher-energy bands that construct the bilayer electronic structure. Within the plane however, we maintain the same intralayer hopping as in the standalone MLG case, obtaining [17, 35]

$$\hat{\boldsymbol{H}}_{\mathrm{BLG}} = \begin{pmatrix} 0 & v\pi^{\dagger} & 0 & 0 \\ v\pi & 0 & \gamma_1 & 0 \\ 0 & \gamma_1 & 0 & v\pi^{\dagger} \\ 0 & 0 & v\pi & 0 \end{pmatrix}. \tag{1.18}$$

From this we can obtain the wavefunction, in a basis $\{\Phi_{A1}, \Phi_{B1}, \Phi_{A2}, \Phi_{B2}\}$ of form

$$\psi_{\mathrm{BLG}} = \frac{1}{\sqrt{C}} \begin{pmatrix} 1 \\ \xi \frac{E_{\mathrm{BLG}}}{vp} e^{i\xi\varphi} \\ \xi \frac{E_{\mathrm{BLG}}}{vp} e^{i\xi\varphi} \\ e^{i2\xi\varphi} \end{pmatrix} e^{i\boldsymbol{k}\cdot\boldsymbol{r}}. \tag{1.19}$$

Above, the term C is the normalisation constant of the wave function. By extension these produce an energy equation of

$$E_{\mathrm{BLG}} = s\left(\frac{\sqrt{\gamma_1^2 + 4v^2p^2}}{2} + \alpha\frac{\gamma_1}{2}\right), \tag{1.20}$$

in which the four distinct solutions are separated and defined by the band index s and the upper ($\alpha = 1$) and lower ($\alpha = -1$) index within that. Within the lowest energy regime of this equation, $vp > \gamma_1$, this displays a quadratic dispersion, however above that, $vp < \gamma_1$, this tends to a linear dependence, as in Fig. 1.3c.

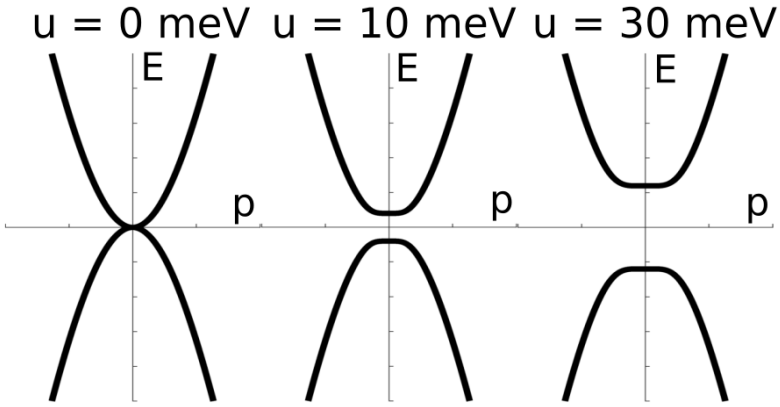

Figure 1.4: A cross section of the parabolic band structure for bilayer graphene shown in Fig. 1.3c and d, highlighting more precisely the dependence of Eq. (1.23) on the external potential u and how the band gap can be manipulated directly.

One additional and important caveat concerning the BLG system is that, through the application of an electric field u perpendicular to the sheets, we can affect the on-site energies of the bilayer, breaking the inversion symmetry of the system and opening a band gap [20]. This transforms the leading diagonal of the Hamiltonian in Eq. (1.18) to

$$\hat{\boldsymbol{H}}_{\mathrm{BLG}} = \begin{pmatrix} \frac{u}{2} & v\pi^{\dagger} & 0 & 0 \\ v\pi & \frac{u}{2} & \gamma_1 & 0 \\ 0 & \gamma_1 & -\frac{u}{2} & v\pi^{\dagger} \\ 0 & 0 & v\pi & -\frac{u}{2} \end{pmatrix}. \tag{1.21}$$

And by extension the wave function to

$$\psi_{\mathrm{BLG}} = \frac{1}{\sqrt{C}} \begin{pmatrix} 1 \\ \xi \frac{\left(E_{\mathrm{BLG}} - \frac{u}{2}\right)}{vp} e^{i\xi\varphi} \\ \xi \frac{1}{\gamma_1} \left[\frac{\left(E_{\mathrm{BLG}} - \frac{u}{2}\right)^2 - v^2p^2}{vp} \right] e^{i\xi\varphi} \\ \frac{1}{\gamma_1} \left[\frac{\left(E_{\mathrm{BLG}} - \frac{u}{2}\right)^2 - v^2p^2}{\left(E_{\mathrm{BLG}} + \frac{u}{2}\right)} \right] e^{i2\xi\varphi} \end{pmatrix} e^{i\boldsymbol{k}\cdot\boldsymbol{r}}. \tag{1.22}$$

The four valley-degenerate eigenenergy solutions of this version of the Hamiltonian therefore have the form

$$E_{\mathrm{BLG}} = s\frac{1}{2}\sqrt{2\gamma_1^2 + u^2 + 4v^2p^2 + \alpha\sqrt{\gamma_1^4 + 4v^2p^2(\gamma_1^2 + u^2)}}. \tag{1.23}$$

Without an external field u present, there are four bands that are parabolic for $vp < \gamma_1$, two of which are degenerate in energy at the neutrality point and two

that are offset by $\pm\gamma_1$. The introduction of the field affects the two bands at the neutrality point, inducing a gap that is proportional to the strength of the field and the difference in the on-site energies u, meaning that we can control the gap size via an external medium [20], as in Fig. 1.4.

There are additional higher-order hopping processes that can be taken into account in the Hamiltonian, most notably a trigonal warping term that affects the low energy bands, however as we are primarily interested in a combination of stacking and external manipulation, these effects are typically surpressed and the core Hamiltonians previously described can provide a fair insight into the electronic properties of the material.

1.2.4 Two-Band Bilayer Graphene Hamiltonian

Alternatively it may be preferable to account purely for the lowest energy bands in the vicinity of the valley - this involves neglecting the two bands separated by γ_1 and distinguished as the upper bands by $\alpha = +1$, as in Eq. (1.23). This is achieved by folding the high-energy dimer state atom contributions, that arise from the direct vertical overlap of the B1 and A2 atoms, onto the lower energy bands.

The full four-band BLG Hamiltonian in Eq. (1.21) can instead be represented as 2×2 matrix, via the Pauli matrices $\boldsymbol{\sigma}_i$, and placed into the Schrödinger equation as

$$\begin{pmatrix} \xi\frac{u}{2}\sigma_z & \xi v\boldsymbol{\sigma}\cdot\boldsymbol{p} \\ \xi v\boldsymbol{\sigma}\cdot\boldsymbol{p} & \left(\gamma_1\sigma_x - \xi\frac{u}{2}\sigma_z\right) \end{pmatrix} \begin{pmatrix} \psi_1 \\ \psi_2 \end{pmatrix} = \epsilon \begin{pmatrix} \psi_1 \\ \psi_2 \end{pmatrix}.$$

The basis of this form is $\{\Phi_{A1}, \Phi_{B2}, \Phi_{A2}, \Phi_{B1}\}$ so that the high-energy dimer state atoms are located in the lower-right quadrant of the Hamiltonian. We then take the two coupled equations that represent this

$$\begin{aligned} \xi\frac{u}{2}\sigma_z\psi_1 + \xi v\boldsymbol{\sigma}\cdot\boldsymbol{p}\psi_2 &= \epsilon\psi_1, \\ \xi v\boldsymbol{\sigma}\cdot\boldsymbol{p}\psi_1 + \left(\gamma_1\sigma_x - \xi\frac{u}{2}\sigma_z\right)\psi_2 &= \epsilon\psi_2, \end{aligned}$$

and placing the second into the first so that we represent the system purely in terms of ψ_1

$$\xi\frac{u}{2}\sigma_z\psi_1 - v^2\left(\boldsymbol{\sigma}\cdot\boldsymbol{p}\right)\left[\gamma_1\sigma_x - \left(\epsilon + \xi\frac{u}{2}\sigma_z\right)\right]^{-1}\left(\boldsymbol{\sigma}\cdot\boldsymbol{p}\right)\psi_1 = \epsilon\psi_1.$$

The inverse middle term uses the fact that for two inverse matrices $(AB)^{-1} =$

$B^{-1}A^{-1}$ and that a term of form $1/(1-x)$ can be approximated to the linear term as $\approx 1+x$ to give

$$\left[\gamma_1\sigma_x - \left(\epsilon + \xi\frac{u}{2}\sigma_z\right)\right]^{-1} \approx \left[1 + \frac{\left(\epsilon + \xi\frac{u}{2}\sigma_z\right)}{\gamma_1\sigma_x}\right]\frac{1}{\gamma_1\sigma_x}.$$

Expanding out all these terms using this approximation and gathering all terms in ϵ on the right hand side, we find

$$\xi\frac{u}{2}\begin{pmatrix}1 & 0\\ 0 & -1\end{pmatrix}\psi_1 - \frac{v^2}{\gamma_1}\begin{pmatrix}0 & \left(\pi^\dagger\right)^2\\ \pi^2 & 0\end{pmatrix}\psi_1 - \frac{\xi v^2 u}{2\gamma_1^2}\begin{pmatrix}\pi^\dagger\pi & 0\\ 0 & -\pi\pi^\dagger\end{pmatrix}\psi_1 = \epsilon\left[1 + \frac{v^2}{\gamma_1^2}\begin{pmatrix}\pi^\dagger\pi & 0\\ 0 & \pi\pi^\dagger\end{pmatrix}\right]\psi_1.$$

Finally, taking the square brackets on the right hand side as $[a+b]$, we simplify by multiplying both sides by $[a-b]$. The square brackets on the right hand side now reduces to $[a^2-b^2]$, where $a^2=1$ and the b^2 term is lead by a $1/\gamma_1^4$ and therefore considered feasibly negligible - this leaves purely $\epsilon\psi_1$ as the right hand side. Multiplying the left hand side by the $[a-b]$ term and neglecting anything above a quadratic in terms of γ_1, we find

$$\left[1 - \frac{v^2}{\gamma_1^2}\begin{pmatrix}\pi^\dagger\pi & 0\\ 0 & \pi\pi^\dagger\end{pmatrix}\right]\left[\xi\frac{u}{2}\begin{pmatrix}1 & 0\\ 0 & -1\end{pmatrix} - \frac{v^2}{\gamma_1}\begin{pmatrix}0 & \left(\pi^\dagger\right)^2\\ \pi^2 & 0\end{pmatrix} - \frac{\xi v^2 u}{2\gamma_1^2}\begin{pmatrix}\pi^\dagger\pi & 0\\ 0 & -\pi\pi^\dagger\end{pmatrix}\right]\psi_1$$
$$\approx \left[\xi\frac{u}{2}\begin{pmatrix}1 & 0\\ 0 & -1\end{pmatrix} - \frac{v^2}{\gamma_1}\begin{pmatrix}0 & \left(\pi^\dagger\right)^2\\ \pi^2 & 0\end{pmatrix} - \frac{\xi v^2 u}{2\gamma_1^2}\begin{pmatrix}\pi^\dagger\pi & 0\\ 0 & -\pi\pi^\dagger\end{pmatrix} - \frac{\xi v^2 u}{2\gamma_1^2}\begin{pmatrix}\pi^\dagger\pi & 0\\ 0 & -\pi\pi^\dagger\end{pmatrix}\right]\psi_1.$$

This left hand side now displays the effective Hamiltonian for the two-band system, found from projecting the high-energy dimer states onto the lower energy contributions.

Therefore, in a basis of $\{\Phi_{A1}, \Phi_{B2}\}$ in the $\boldsymbol{K}_+$ valley and $\{\Phi_{B2}, \Phi_{A1}\}$ in the other, we reduce to [17]

$$\hat{\boldsymbol{H}}_{\mathrm{BLG}} = -\frac{1}{2m}\begin{pmatrix}0 & \pi^{\dagger 2}\\ \pi^2 & 0\end{pmatrix} + \frac{\xi u}{2}\begin{pmatrix}1 & 0\\ 0 & -1\end{pmatrix} - \frac{\xi u v^2}{\gamma_1^2}\begin{pmatrix}\pi^\dagger\pi & 0\\ 0 & -\pi\pi^\dagger\end{pmatrix}. \tag{1.24}$$

In this, the v and γ_1 parameters are collapsed into the term $m = \gamma_1/(2v^2)$.

From this form, we can note the similarities to the monolayer Hamiltonian,

with linear terms replaced by quadratic and perturbations included due to the possibility of symmetry breaking on-site energy differences. The eigenenergies and wave functions of such a Hamiltonian descriptor are

$$\begin{aligned} E_{\mathrm{BLG}} &= s\frac{\sqrt{4\gamma_1^2 v^4 p^4 + u^2\left(\gamma_1^4 - 4\gamma_1^2 v^2 p^2 + 4v^4 p^4\right)}}{2\gamma_1^2}, \\ \psi_{\mathrm{BLG}} &= \frac{1}{\sqrt{C}}\begin{pmatrix} 1 \\ \dfrac{\gamma_1^2\left(E_{\mathrm{BLG}} - \xi u\left(\frac{1}{2} - \frac{1}{\gamma_1^2}v^2p^2\right)\right)}{v^2p^2} \end{pmatrix} e^{i\boldsymbol{k}\cdot\boldsymbol{r}}. \end{aligned} \tag{1.25}$$

It is worth noting that as $u \to 0$, the E_{BLG} form reduces to

$$E_{\mathrm{BLG}} = s\frac{v^2p^2}{\gamma_1}, \tag{1.26}$$

this more obviously quadratic form further cements the suggestion that this two-band approach models purely the low-energy regime.

We typically rely on the full four-band model description of bilayer graphene in order to provide a more complete description of the band structure, however under certain circumstances where we are particularly interested in the two lowest-energy bands, such as the device described in Chap. 3, we utilise the simpler two-band model.

1.3 Moiré Patterns & Superlattices

The layered graphene structures described thus far can all be considered as rotationally aligned, as all layers involved share the same crystalline directions and crystal structures. This gives them periodicities that can be described on the scale of Angstroms, with unit cells containing only a handful of atoms. However, another large subsection of these simple component materials consists of superlattices. These arise not only due to a mismatch in the crystalline directions of adjacent layers, but also due to mismatches in the constituent lattice constants that typically stems from the use of differing species of 2DACs, each with their own intrinsic period. This results in a periodicity that is mismatched when considering the individual unit cells of the layers, however this mismatch adds up across many unit cells to produce a new periodicity that can instead be described on the scale of nano-metres.

Electrons moving through a weak periodic potential such as this typically exhibit band reconstruction and flattening, alongside mini-gaps around the edges of

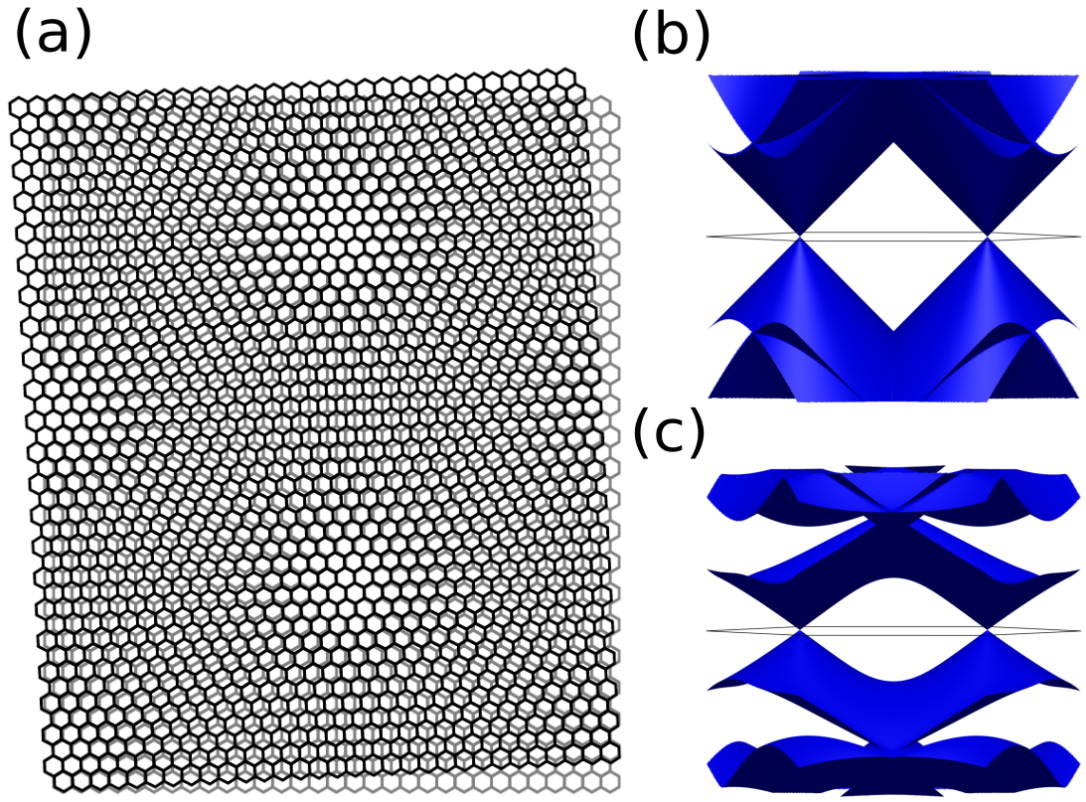

Figure 1.5: (a) Superlattice constructed at the interface between two graphene sheets rotationally misaligned by 3°. The new real space periodicity $\boldsymbol{A}_i$ is defined by the two regions where the beating of the individual layers are in sync, here they are roughly vertical to one another, however varying θ will change the direction of this vector. (b) The uncoupled spectra of the twisted bilayer system, comprised of two offset linear Dirac cones from the two individual layers. (c) Coupled spectra with $w = 110$meV. Note the flattening of the band structure between the two cones - this has a profound effect on the density of states around this energy and is exploited in the basis of the work of Chap. 4.

the Brillouin zone they inhabit [37]. In a more general approach to the problem, a generic stacked superlattice without an exactly defined perturbation or substrate tends to have mini-bands that exhibit flattening and the opening of gaps (and the formation of more exotic features, such as secondary Dirac points in certain circumstances [30]) under this superlattice perturbation. These general properties are exploited throughout this work, in order to construct stacks with novel properties. Some of the more simplistic superlattice structures are discussed in the following section in order to give a general overview of graphene-based superlattices and moiré patterns and their general electronic properties.

1.3.1 Twisted Bilayer Graphene

Another relatively simple variation of the graphene structure we use is Twisted Bilayer Graphene (tBLG), comprised again of two monolayer sheets but now with their crystallographic axes rotationally misaligned by an angle θ. This means that the primitive lattice vectors of the two individual sheets are related by $\boldsymbol{a}' = \hat{\boldsymbol{R}}_\theta \boldsymbol{a}$, in which $\hat{\boldsymbol{R}}_\theta$ represents the anti-clockwise rotation matrix of form

$$\hat{\boldsymbol{R}}_\theta = \begin{pmatrix} \cos\theta & -\sin\theta \\ \sin\theta & \cos\theta \end{pmatrix}. \tag{1.27}$$

With the periodicities rotationally misaligned, a longer range periodicity or moiré pattern is formed by the beating of the two individual layers, with a length that depends on the rotation angle, as seen in Fig. 1.5a. We define a new real space lattice vector $\boldsymbol{A}_i$ to describe this new large scale periodicity, that corresponds to the joining of two regions with similar atomic surroundings. This effect is most easily seen by joining the regions where the two layers are beating roughly in-phase and thus the hexagonal structures are, again roughly, vertically stacked and the colour behind the stack can be seen. Note that the hexagonal periodicity is also retained in this process. The corresponding Superlattice Brillouin Zone (sBZ), also hexagonal but now much smaller in reciprocal space due to the long-range real space periodicity, that describes this system depends only on the misalignment angle θ of the two sheets. The six shortest reciprocal lattice vectors are given by [30]

$$\begin{aligned} \boldsymbol{b}_m &= \hat{\boldsymbol{R}}_{\frac{2\pi m}{6}}[1 - \hat{\boldsymbol{R}}_\theta]\left(0, \frac{4\pi}{\sqrt{3}a}\right), \\ |b_m| &\approx \theta\frac{4\pi}{\sqrt{3}a}, \quad m = 0, 1, ..., 5. \end{aligned} \tag{1.28}$$

These correspond to the separation between the two Dirac cones of the individual layers, introduced by the rotation of the sheets. We define six reciprocal lattice vectors via m for completeness in methods that are detailed later within this thesis, however, as with all periodic 2D systems, the periodicity can be more simply described by two vectors. The four others are simply reflections or additions of these two primitive vectors, for instance $\boldsymbol{b}_0 = -\boldsymbol{b}_3$ and $\boldsymbol{b}_2 = -\boldsymbol{b}_0 + \boldsymbol{b}_1$.

The real space lattice vectors of the moiré pattern can be found using $\boldsymbol{b}_i \cdot \boldsymbol{A}_i = 2\pi\delta_{ij}$. As $|\boldsymbol{A}_i| > |\boldsymbol{a}_i|$, the overall electronic structure can be described in terms of the moiré periodicity rather than the individual layer periodicities.

However, the electronic structure can still be described in a similar manner as

before - as two monolayer graphene sheets with a vertical coupling between them. The variation in the continuum model Hamiltonian lies in the coupling term $\hat{\boldsymbol{H}}_{\mathrm{T}}$ in Eq. (1.17) and how it varies across the new larger periodicity,

$$\hat{\boldsymbol{H}}_{\mathrm{tBLG}} = \begin{pmatrix} \hat{\boldsymbol{H}}_{\mathrm{MLG}} & \hat{\boldsymbol{H}}_{\mathrm{T}}(\theta) \\ \hat{\boldsymbol{H}}^{*}_{\mathrm{T}}(\theta) & \hat{\boldsymbol{H}}_{\mathrm{MLG}} \end{pmatrix}. \tag{1.29}$$

Instead, $\hat{\boldsymbol{H}}_{\mathrm{T}}(\theta)$ has a form that couples to the three equivalent same-valley Dirac points within the BZ via [38]

$$\hat{\boldsymbol{H}}_{\mathrm{T}}(\theta) = w \sum_{m=1}^{3} \exp(-i\boldsymbol{b}_m(\theta)\cdot\boldsymbol{r})T_m,$$
$$T_1 = \begin{pmatrix} 1 & 1 \\ 1 & 1 \end{pmatrix}, \quad T_2 = \begin{pmatrix} e^{-i\frac{2\pi}{3}} & 1 \\ e^{i\frac{2\pi}{3}} & e^{-i\frac{2\pi}{3}} \end{pmatrix}, \quad T_3 = \begin{pmatrix} e^{i\frac{2\pi}{3}} & 1 \\ e^{-i\frac{2\pi}{3}} & e^{i\frac{2\pi}{3}} \end{pmatrix}, \tag{1.30}$$

where w, in comparison to the zero angle case, is given a value of 110 meV.

The electronic structure of tBLG is surprisingly distinct from that of BLG and can instead be described as the hybridisation of two conical monolayer graphene dispersions, that are slightly rotational misaligned from one another, as seen in Fig. 1.5b and c. The size of the superlattice BZ and therefore the energy at which the two cones meet and the bands hybridise is dependent entirely on the rotation angle between the two sheets and results in a new mini-band structure. Most notably, it contains a saddle point, a feature that has a large impact on the density of states (this is discussed in more detail in Chap. 5) - this flattening of minibands, as previously discussed, is a common feature of superlattice energy band reconstructions and one that we exploit in the construction of superlattice-based devices, such as those in Chap. 2 and 4.

1.3.2 Monolayer Graphene on hBN

A more common superlattice construct consists of graphene placed onto an insulating substrate, with a structural periodicity that is similar, but different, to that of graphene. In these setups, as opposed to the twisted bilayer case, both the rotational misalignment θ and the lattice constant mismatch δ of the two materials affect the beating length and thus the superlattice length and direction. The strength of perturbation and coupling felt by the graphene electrons due to the substrate depends on a multitude of factors such as the structural layout and constituent atoms of the substrate layer and the rotational alignment between

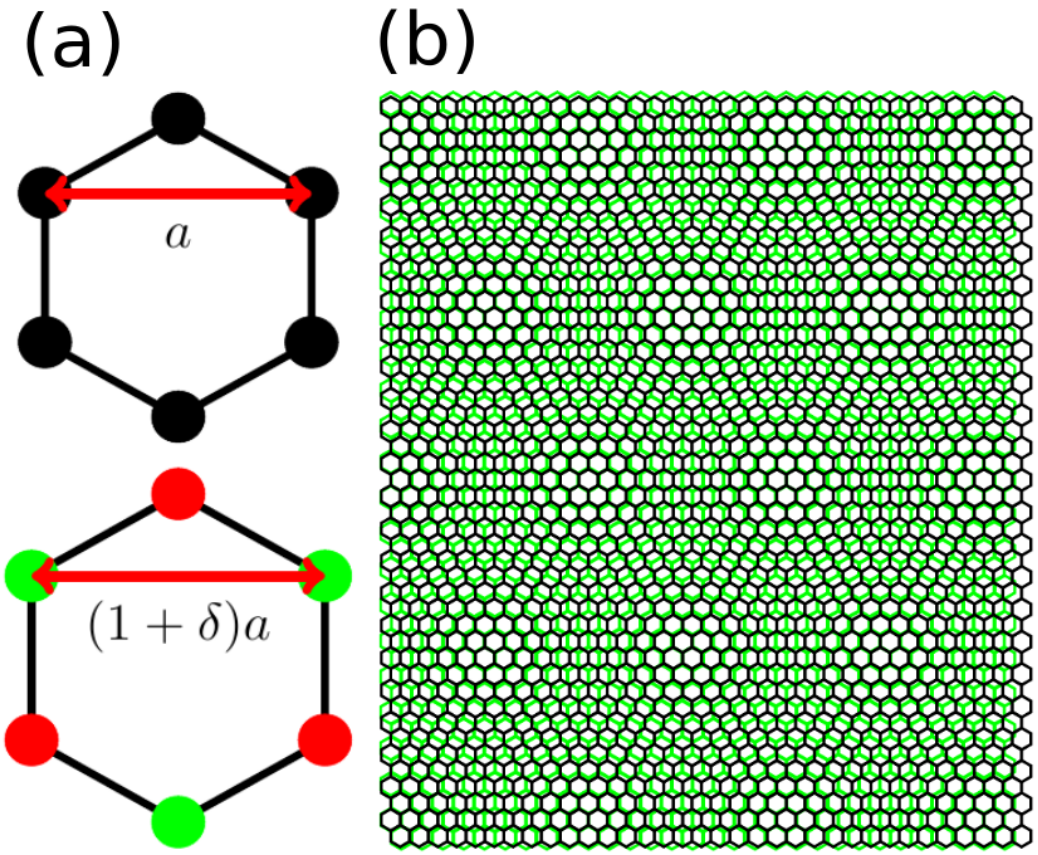

Figure 1.6: (a) Comparison of the lattice constants of graphene and hexagonal boron nitride, mismatch scale exaggerated. (b) Superlattice of graphene and hexagonal boron nitride substrate. Mismatch scale again exaggerated in order to display periodicity over a shorter lengthscale and therefore all six of the nearest periodic points, defined by the differing m in Eq. (1.31).

them.

A generic form of moiré harmonics constructed by two stacked hexagonal materials with similar lattice constants, related via $\boldsymbol{a}'_m = (1+\delta)\hat{\boldsymbol{R}}_\theta \boldsymbol{a}_m$, can be described by [30]

$$\begin{aligned} \boldsymbol{b}_m &= \hat{\boldsymbol{R}}_{\frac{2\pi m}{6}} \left[1 - (1+\delta)^{-1}\hat{\boldsymbol{R}}_\theta\right] \left(0, \frac{4\pi}{\sqrt{3}a}\right), \\ |b_m| &\approx \frac{4\pi}{\sqrt{3}a}\sqrt{\delta^2+\theta^2}, \quad m = 0, 1, ...5. \end{aligned} \tag{1.31}$$

It is assumed that both the lattice mismatch and the misalignment angle are small, $|\delta, \theta| \ll 1$. As such, the real space lattice constant describing the new moiré pattern, again described by A and now dependent on the lattice mismatch δ as $A = a/\sqrt{\delta^2+\theta^2}$, can be seen to quickly increase in magnitude in comparison to the original graphene lattice vector a.

As before, the structure can be described as an interaction between the two layers and thus the general form of the Hamiltonian is

$$\hat{\boldsymbol{H}}_{\text{G+Substrate}} = \begin{pmatrix} \hat{\boldsymbol{H}}_{\text{MLG}} & \hat{\boldsymbol{H}}_{\text{T}}(\theta,\delta) \\ \hat{\boldsymbol{H}}^*_{\text{T}}(\theta,\delta) & \hat{\boldsymbol{H}}_{\text{Substrate}} \end{pmatrix} \tag{1.32}$$

In contrast to the twisted bilayer case, the lack of hybridisation due to the large insulating gap of the substrate means that we focus entirely on the effect of the substrate on the electronic structure of the graphene. Therefore, the Hamiltonian can be folded down, in a similar approach to that of the two-band bilayer graphene model, to a perturbation problem of form $\hat{\boldsymbol{H}}_{\text{G+Substrate}} = \hat{\boldsymbol{H}}_{\text{MLG}} + \delta\hat{\boldsymbol{H}}$, where [30]

$$\begin{aligned} \delta\hat{\boldsymbol{H}} =& u_0 v\hbar b f_1(\boldsymbol{r}) + u_3 v\hbar b f_2(\boldsymbol{r}) + u_1 v\hbar[\boldsymbol{l}_z \times \nabla f_2(\boldsymbol{r})]\cdot\boldsymbol{\sigma}\tau_3, \\ f_1(\boldsymbol{r}) = \sum_{m=0}^{5} e^{i\boldsymbol{b}_m\cdot\boldsymbol{r}}, &\quad f_2(\boldsymbol{r}) = \sum_{m=0}^{5}(-1)^m e^{i\boldsymbol{b}_m\cdot\boldsymbol{r}}, \end{aligned} \tag{1.33}$$

in a basis of $\{\Phi_{A,K_+}, \Phi_{B,K_+}, \Phi_{B,K_-}, -\Phi_{A,K_-}\}$, that describes the perturbation in both sublattices, A and B, and both valleys, K_+ and K_-. $\boldsymbol{l}_z$ represents a unit vector in the z-direction, the two sets of Pauli matrices, σ_i and τ_i, act in the sublattice and valley indices respectively and the Kronecker product is utilised such that $\sigma_i\tau_j \equiv \sigma_i \otimes \tau_j$. Note that the identity matrix versions of these Pauli matrices, σ_0 and τ_0, are omitted from the above equation for brevity.

The strength of the perturbation is given by the constant set $\{u_0, u_1, u_3\}$, where

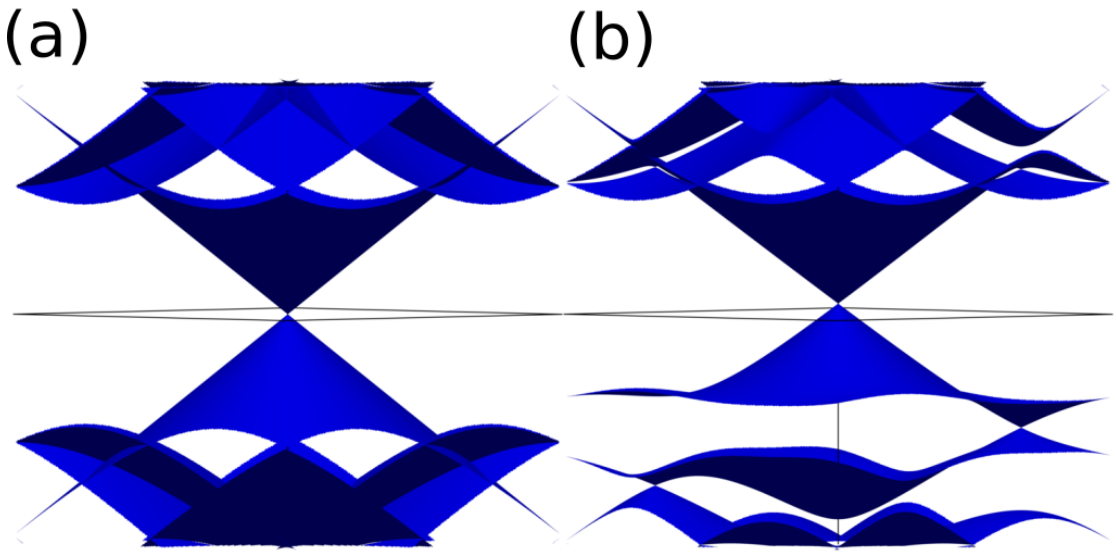

Figure 1.7: (a) Unperturbed miniband spectrum of graphene, folded into induced superlattice Brillouin zone under an unrotated hBN substrate. (b) Miniband spectra of unrotated MLG/hBN structure, produced utilising perturbation constant set suggested in Ref. [39], $u_0 = 0.032, u_1 = -0.063, u_3 = -0.055$. The low energy linear spectra is preserved, whilst a secondary Dirac point is produced within the valence band.

u_0 can be thought of as a potential modulation, u_3 as the asymmetry of the A and B sublattice and u_1 affecting the hopping between the A and B sublattice sites. We assume this perturbation is small such that $|u_i| \ll 1$ and that it will vary depending on factors such as the substrate material, periodicity and rotational misalignment.

The presence of an inversion asymmetric substrate, whereby one atom within the hexagonal unit cell has a differing perturbation than the other, can also be modelling using three extra perturbation terms that mirror the positions of the $\{u_0, u_1, u_3\}$ set [30]. However, current estimates for known substrates that are inversion asymmetric, such as hexagonal boron nitride [39], suggest that their contributions are small in comparison to the inversion symmetric case. Also, in general these contributions tend to open gaps in the spectrum [40] - this should either not affect or only enhance the qualitative deductions in the following chapters and for those reasons we neglect it.

The most common example of such a structure is that of graphene on a hexagonal boron nitride substrate. Hexagonal boron nitride is another two-dimensional atomic crystal with a honeycomb structure that is similar to graphene in the lattice constant length, but mismatched and differing by 1.8% [30]. As opposed to the purely carbon-based unit cell of graphene, the A and B sites contain a boron and nitrogen atom respectively, such that each species is surrounded by three nearest

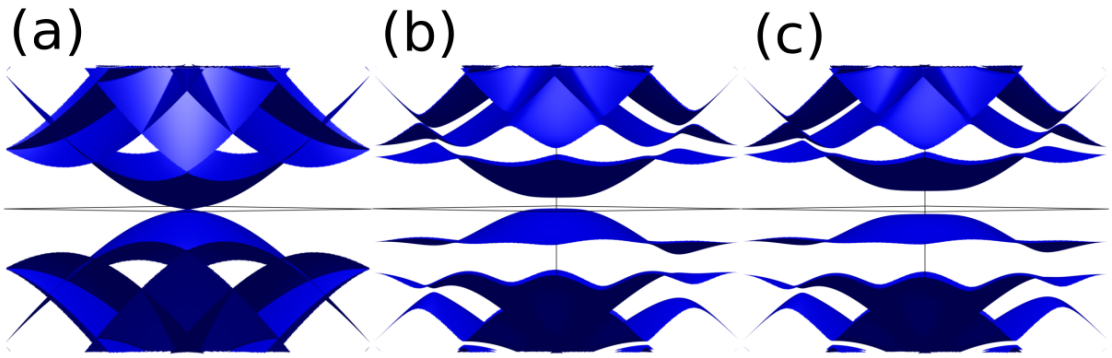

Figure 1.8: (a) Unperturbed miniband spectrum of bilayer graphene on an unrotated hBN substrate, note the similarity to the unperturbed monolayer case in Fig. 1.7a, but with a parabolic dispersion. (b) Miniband spectrum under same perturbation set in Fig. 1.7b, unlike the monolayer spectrum the bilayer dispersion typically opens mini-gaps due to the breaking of layer symmetry introduced by the substrate. (c) The same perturbed spectrum, with the central gap enhanced by the presence of an external potential across the system, $u = 70$meV.

neighbours of the opposite species. In order to avoid hybridisation from the perturbing layer, as in twisted bilayer graphene, hBN is chosen as it is an insulator with a large band gap of 5.8eV [41].

Again, the form of perturbation felt by the graphene sheet is dependent entirely on the substrate structure and component atoms. Even in the case of a monolayer graphene-hexagonal boron nitride composite, the exact perturbation is unknown, however various models have arisen in order to describe the miniband system [39] and certain features of the spectrum predicted. Currently, one such model that agrees with optical absorption data [42] retains the linear spectrum around the neutrality point, alongside a more severe reconstruction of the valence band, exhibiting somewhat flattened minibands and a secondary Dirac point at ~ 100meV. This miniband reconstruction can be seen in Fig. 1.7.

1.3.3 Bilayer Graphene on hBN

As a simple extension of this, we can choose to stack bilayer graphene, as previously detailed in structure, onto a hexagonal boron nitride substrate. The perturbation felt should be identical in beating length, due to MLG and BLG sharing the same lattice vectors and the mismatch in periodicities being the same as before. As such, features such as the superlattice vectors in Eq. (1.31) and the superlattice length are maintained.

However, now with the presence of the secondary layer, we use another primary tenant of van der Waals heterostructures construction - that adjacent layers have

the most direct effect on one another [43]. In other words, we model the system as a bilayer sheet in which only the adjacent layer is perturbed by the presence of the substrate. Again, we model this system as a perturbed graphene system such that $\hat{\boldsymbol{H}} = \hat{\boldsymbol{H}}_{BLG} + \delta\hat{\boldsymbol{H}}$, where the perturbation is folded onto the states of the bilayer graphene. This is described by a Hamiltonian, in a layer-separated basis, of form

$$\hat{\boldsymbol{H}}_{\text{BLG + Substrate}} = \begin{pmatrix} \hat{\boldsymbol{H}}_{\text{MLG}} + \frac{u}{2} + \delta\hat{\boldsymbol{H}} & \hat{\boldsymbol{H}}_{\text{T}} \\ \hat{\boldsymbol{H}}_{\text{T}}^{\dagger} & \hat{\boldsymbol{H}}_{\text{MLG}} - \frac{u}{2} \end{pmatrix}. \tag{1.34}$$

Where $\delta\hat{\boldsymbol{H}}$ is the same perturbation defined in Eq. (1.33) and $\hat{\boldsymbol{H}}_T$ contains the interlayer coupling γ_1. We also introduce an additional degree of perturbation, in the inclusion of an external field term u, the effects of which were discussed previously.

The fact that the substrate perturbation affects only one of the two layers breaks the layer symmetry (similar to the case of an electric field across the layers) and, in general, opens a gap at the neutrality point. Depending on the values of the perturbation constants, the superlattice potential may open additional gaps between minibands higher in energy, as in the monolayer case. However, it may be combined with the presence of an external field across the layers, in order to perturb the band structure further. An example of this can be seen in Fig. 1.8, in which the structure is perturbed by the presence of the substrate and the central gap is modified further by the external potential across the system, whereas the higher order gaps remain roughly constant.

1.3.4 Monolayer Graphene on an Almost Commensurate $\sqrt{3} \times \sqrt{3}$ Substrate

In the case of the graphene/hexagonal boron nitride system, we utilise a substrate with a unit cell that is similar in size to that of graphene but with a slight adjustment to the lattice constant that induces the large-scale quasi-periodic interaction between the two. Other forms of periodicity exist however, such as the Kekulé lattice that is represented by a hexagonal periodicity that is three times larger than that of graphene, with sides that span the distance between two neighbouring atoms of the same sublattice [44]. This results in a relationship between the graphene lattice constant and the substrate as $a_{Sub} = \sqrt{3}a$, however we again introduce a mismatch in order to induce a much longer periodicity and thus a relationship between lattice constants of $a_{Sub} = \sqrt{3}(1+\delta)a$, where δ again represents the mismatch.

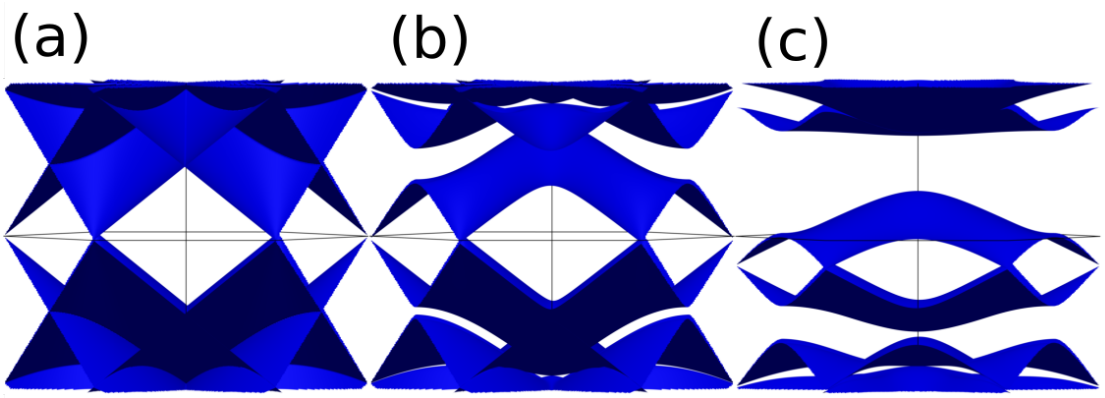

Figure 1.9: (a) Unperturbed miniband spectrum folded into superlattice Brillouin zone from an almost commensurate $\sqrt{3} \times \sqrt{3}$ substrate, recast such that the two valleys are folded to opposite corners of the sBZ. (b) Perturbed energy spectrum ($U_{E'} = 0.02, U_G = -0.04, U_{G'} = 0$) displaying general properties of perturbation, in the preservation of the linear spectrum and flattening of higher order minibands. (c) Larger perturbation ($U_{E'} = 0.07, U_G = -0.14, U_{G'} = 0$), opening mini-gaps within the spectra, between the first and second mini-bands.

This results in a superlattice Brillouin zone of form [45]

$$\begin{aligned} \boldsymbol{b}_m &= \hat{\boldsymbol{R}}_{\frac{2\pi m}{6}} \left[1 - (1+\delta)^{-1} \hat{\boldsymbol{R}}_\theta\right] \left(0, \frac{4\pi}{\sqrt{3}a}\right), \\ |b_m| &\approx \frac{4\pi}{\sqrt{3}a} \sqrt{\delta^2 + \theta^2}, \quad m = 0, 1, ...5. \end{aligned} \tag{1.35}$$

We can note the similarities to the previous case in Eq. (1.31). However, it can be shown that there is a coexisting periodicity [45], corresponding to periodicity with the commensurate Kekulé lattice and defined by $\boldsymbol{\beta}_m = (1/\sqrt{3})\hat{\boldsymbol{R}}_{-\frac{\pi}{2}} \boldsymbol{b}_m$ - this is discussed in more detail in the main body and appendix of Chap. 2.

The Hamiltonian can again be represented as a perturbation of the graphene sheet via $\hat{\boldsymbol{H}} = \hat{\boldsymbol{H}}_{\text{MLG}} + \delta\hat{\boldsymbol{H}}$, with a perturbation of form [45]

$$\begin{aligned} \delta\hat{\boldsymbol{H}} &= U_{E'} v\hbar\beta F(\check{\boldsymbol{\beta}})\sigma_z + U_G v\hbar[\nabla F(\check{\boldsymbol{\beta}})] \cdot [\boldsymbol{\sigma} \times \boldsymbol{l}_z] + U_{G'} v\hbar[\nabla F(\check{\boldsymbol{\beta}})] \cdot \boldsymbol{\sigma}, \\ F(\check{\boldsymbol{\beta}}) &= f_1(\check{\boldsymbol{\beta}})\tau_x + f_2(\check{\boldsymbol{\beta}})\tau_y, \\ f_1(\check{\boldsymbol{\beta}}) = \sum_{m=0,...,5} e^{i\boldsymbol{\beta}_m \cdot \boldsymbol{r}}, &\quad f_2(\check{\boldsymbol{\beta}}) = i \sum_{m=0,...,5} (-1)^m e^{i\boldsymbol{\beta}_m \cdot \boldsymbol{r}}. \end{aligned} \tag{1.36}$$

We choose to realign our superlattice BZ by offsetting the central cone seen in the MLG-hBN structure (Fig. 1.7) to the corner. As this substrate couples the two valleys of the graphene, we obtain degenerate solutions and the new sBZ can

thought of analogously to the original graphene BZ, in which the corners of the hexagon have a linear dispersion that alternates in valley number.

The form and magnitude of the perturbation constants $\{U_{E'}, U_G, U_{G'}\}$ again depend entirely on the structural properties of the layered bilayer and the constituent atoms of the substrate chosen. However a general probe into the properties of such a perturbation reveal the preservation of the linear Dirac cones around the neutrality point and the opening of band gaps between the first and second minibands, asymmetrically in the conduction and valence bands, as seen in Fig. 1.9 [45].

We can expand upon this model in the same manner as the almost commensurate substrate case detailed in Sections 1.3.2 and 1.3.3, by instead converting the monolayer to a bilayer, where the symmetry of system is inherently broken by the substrate perturbation. We can combine this with an external potential perpendicularly across the device, to break the symmetry further and perturb the band structure more profoundly - this provides the basis of the work in Chap. 2.

Chapter 2

Bilayer graphene on an almost commensurate $\sqrt{3} \times \sqrt{3}$ substrate

2.1 Introduction

Since the seminal paper by Esaki and Tsu [47], the idea of tailoring the electronic properties of materials by forming superlattices has had a huge impact on semiconductor physics [48]. More recently, this work has bled into the field of 2D atomic crystals with work such as the electronic properties of graphene being modified by the application of a lateral periodic potential [49, 50, 51, 52, 53] or a one-dimensional artificial graphene superlattice that has been fabricated experimentally using electrostatic gates [54]. A two-dimensional superlattice can also be produced more simply by placing graphene on a hexagonal substrate/surface facet such as hexagonal boron nitride (hBN) [55], Ir(111) [56] or Ru(0001) [57]. In these cases, the superlattice moiré pattern arises due to the mismatch between the graphene and the substrate lattice constants and misalignment of the crystalline directions of the two materials. The most common example is that of graphene on hBN, a heterostructure that attracted considerable attention because, for example, it provided the first observation of the fractal spectrum of magnetic minibands known as Hofstadters butterfly [58, 59, 60] and detection of topological valley currents [61]. Within the structure, weak coupling between the two crystals and close match of the reciprocal lattice vectors in the two materials allow a continuum model description of the perturbation using only harmonic functions of the six smallest reciprocal lattice vectors of the superlattice [40]. The Bragg scattering of graphene electrons by reciprocal lattice vectors of hBN leads to the formation of minibands due to an effective coupling of states in the vicinity of the same graphene Brillouin zone (BZ) corner [40, 62].

A contrasting case of coupling electronic states in the vicinity of the inequivalent graphene BZ corners can be achieved by engineering a $\sqrt{3} \times \sqrt{3}$ superlattice [44, 63, 64, 65, 66], also called the Kekulé lattice of graphene, for example by utilising a choice of substrate with a hexagonal unit cell three times larger than that of graphene, as shown in Fig. 2.1. For such a superlattice, a band gap is opened at the Dirac point [44, 63]. It has also been suggested that for specific superlattice parameters a single-valley quadratic band crossing appears in the spectra [64, 65, 66]. If the substrate is not ideally commensurate, a long wavelength moiré pattern similar to that for graphene on hBN appears, shown schematically in Fig. 2.2a, and the intervalley coupling oscillates in space with the moiré period. As

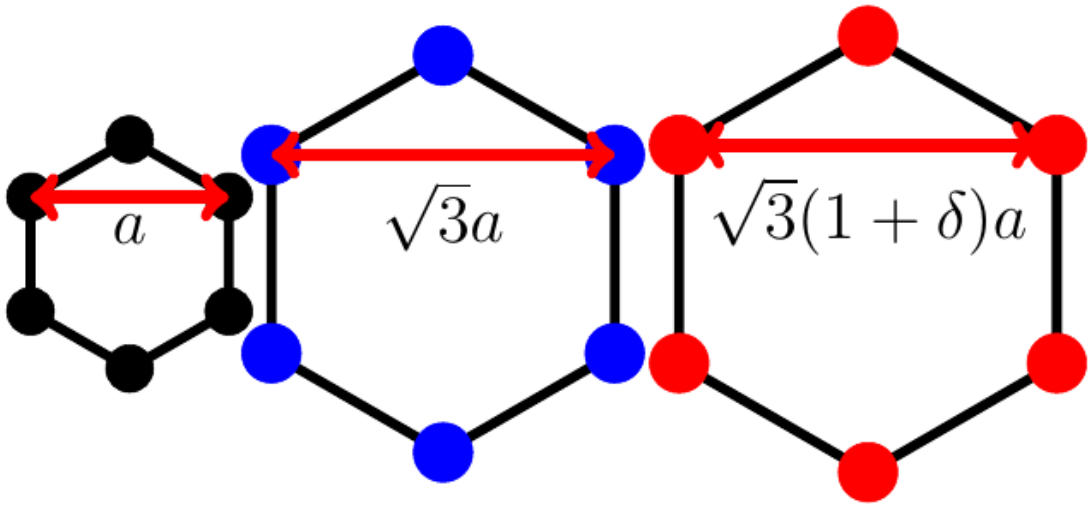

Figure 2.1: The three unit cell periodicities involved; graphene (left), Kekule lattice (middle) and an incommensurate $\sqrt{3} \times \sqrt{3}$ substrate (right). Each with their relative length scales, related to the graphene lattice constant, a.

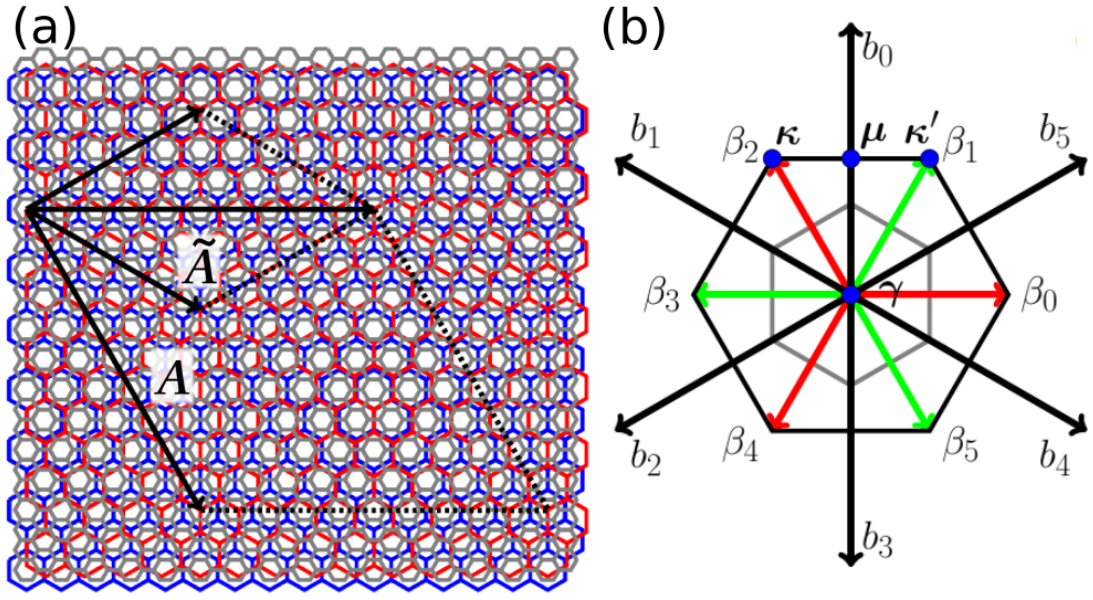

Figure 2.2: (a) Visualisation of the moiré superlattice, with graphene (grey) and an incommensurate $\sqrt{3} \times \sqrt{3}$ substrate (red). Also shown is the Kekulé lattice of graphene (blue). For clarity, we choose a large δ, set $\theta = 0$ and do not show the top graphene layer of BLG. While the mismatch δ between the substrate (red) and the graphene Kekulé lattice (blue) results in a superlattice periodicity set by $\boldsymbol{A}$, a shorter periodicity $\tilde{\boldsymbol{A}}$ of the local atomic arrangement surrounding a carbon atom (grey) always exists (see Appendix for details). (b) The two periodicities set by $\boldsymbol{A}$ and $\tilde{\boldsymbol{A}}$ result in two sets of basic reciprocal vectors, $\check{\boldsymbol{\beta}}_m$ and $\check{\boldsymbol{b}}_m$, $m = 0, 1, ..., 5$, respectively, and two superlattice Brillouin zones that can be used to describe the miniband spectrum. For the larger BZ set by the reciprocal vectors $\check{\boldsymbol{b}}_m$, we introduce the high-symmetry points γ, μ and κ. Figure reprinted from Ref. [46], copyright (2016), with permission from the American Physical Society.

shown in the prior chapter, in such a case the electron states at the Dirac point remain unaffected but typically gaps are open between the first and second miniband on the conduction/valence side [45].

In this chapter, we investigate the electronic properties of a heterostructure comprising of bilayer graphene (BLG) and a semiconducting almost commensurate $\sqrt{3} \times \sqrt{3}$ substrate. We use the form of the moiré perturbation derived previously for monolayer graphene [45] to study the miniband spectrum produced and combine this effect with that of the band structure in the presence of an external electric field. This electric field, perpendicular to the graphene layers, modifies the BLG electronic spectrum [20, 35, 67] that is folded into minibands by the moiré perturbation and redistributes the electronic wave function between the two layers, influencing the impact of the superlattice on the electronic spectrum. We show that, for a large range of moiré perturbation parameters, the miniband spectrum can be tuned via the external potential from a structure with a single band gap to one with a narrow miniband separated by a band gap on each side from the rest of the spectrum. Such an effect was not predicted for BLG on hBN, for which the behaviours of the first and second miniband edges were essentially unaffected by the external electric field [43].

2.2 Electronic Hamiltonian

We consider bilayer graphene [17], two coupled honeycomb layers of carbon atoms in an AB (Bernal) stacking. This is placed on a substrate with a lattice constant $a_s = \sqrt{3}(1+\delta)a$, $|\delta| \ll 1$, where $a = 2.46\mathring{A}$ is the lattice constant of graphene, with an angle θ between the crystalline directions of the two materials. The BLG unit cell contains four atoms $A1$, $B1$, $A2$ and $B2$ where A and B denote the two sublattices within a single layer and the numbers 1 and 2 indicate the bottom and top layer, respectively.

To describe the electronic properties of BLG, we use the four-band model for the π-electrons, applicable in the vicinity of the BZ corner or valley $\boldsymbol{K}_\xi = (\xi\frac{4\pi}{3a}, 0)$, where $\xi = \pm 1$ distinguishes between the two inequivalent BZ corners. Because of the exponential decay of the $2p_z$ orbital wave function with increasing distance [43, 68], we assume that the influence of the substrate on BLG is effectively limited to the bottom graphene layer which is closer to the substrate. We follow the symmetry-based analysis performed for monolayer on an incommensurate $\sqrt{3}\times\sqrt{3}$ substrate [45] and use the six shortest reciprocal lattice vectors of the moiré given by the difference between the reciprocal lattice vectors of the substrate and the

Kekulé lattice of graphene, as in Eq. (1.35) and as shown in Fig. 2.2a,

$$\{\boldsymbol{\beta}_m\} = \hat{\boldsymbol{R}}_{\frac{2\pi m}{6}} \left[1 - \frac{1}{(1+\delta)}\hat{\boldsymbol{R}}_\theta\right] \left(0, \frac{4\pi}{3a}\right), \tag{2.1}$$

to write the Hamiltonian

$$\hat{\boldsymbol{H}} = \begin{pmatrix} \hat{\boldsymbol{H}}_{\text{MLG}} + \frac{u}{2} + \delta\hat{\boldsymbol{H}} & \hat{\boldsymbol{T}} \\ \hat{\boldsymbol{T}}^\dagger & \hat{\boldsymbol{H}}_{\text{MLG}} - \frac{u}{2} \end{pmatrix},$$

within which we utilise the perturbation from Eq. (1.36) to construct our full description as

$$\begin{gathered} \hat{\boldsymbol{H}}_{\text{MLG}} = v\boldsymbol{\sigma}\cdot\boldsymbol{p}, \quad \hat{\boldsymbol{T}} = \frac{1}{2}\gamma_1(\tau_z\sigma_x - i\sigma_y), \\ \delta\hat{\boldsymbol{H}} = U_{E'}v\beta F(\check{\boldsymbol{\beta}})\sigma_z + U_G v[\nabla F(\check{\boldsymbol{\beta}})]\cdot[\boldsymbol{\sigma}\times\boldsymbol{l}_z] + U_{G'}v[\nabla F(\check{\boldsymbol{\beta}})]\cdot\boldsymbol{\sigma}, \\ F(\check{\boldsymbol{\beta}}) = f_1(\check{\boldsymbol{\beta}})\tau_x + f_2(\check{\boldsymbol{\beta}})\tau_y, \\ f_1(\check{\boldsymbol{\beta}}) = \sum_{m=0,\ldots,5} e^{i\boldsymbol{\beta}_m\cdot\boldsymbol{r}}, \quad f_2(\check{\boldsymbol{\beta}}) = i\sum_{m=0,\ldots,5}(-1)^m e^{i\boldsymbol{\beta}_m\cdot\boldsymbol{r}}. \end{gathered} \tag{2.2}$$

Above, we have written the Hamiltonian $\hat{\boldsymbol{H}}$ of our perturbed system in the basis of Bloch states $\{\psi_{A1}^{K_+}, \psi_{B1}^{K_+}, \psi_{B1}^{K_-}, -\psi_{A1}^{K_-}, \psi_{A2}^{K_+}, \psi_{B2}^{K_+}, \psi_{B2}^{K_-}, -\psi_{A2}^{K_-}\}^T$. We have also set $\hbar = 1$ and introduced a unit vector along the z-axis, $\boldsymbol{l}_z$, and two sets of Pauli matrices, σ_i, $\boldsymbol{\sigma} = (\sigma_x, \sigma_y)$ and τ_i, acting in the sublattice and valley space, respectively, as well as their direct products $\tau_i\sigma_j \equiv \tau_i \otimes \sigma_j$. Note that we again omit the presence of identity matrix version of both these Pauli matrices, τ_0 and σ_0.

The diagonal intralayer blocks $\hat{\boldsymbol{H}}_{\text{MLG}}$ have Fermi velocity $v \simeq 10^6 \text{ms}^{-1}$ [69] and an electron momentum $\boldsymbol{p}$ measured from the centre of the valley, corresponding to the Dirac-like Hamiltonian for electrons in monolayer graphene. The off-diagonal block $\hat{\boldsymbol{T}}$ using $\gamma_1 \simeq 0.38\text{eV}$, taken from experiment [70], describes the coupling between the layers and u denotes the interlayer asymmetry due to an external perpendicular electric field. The moiré perturbation is captured by the term $\delta\hat{\boldsymbol{H}}$ which appears in the top left block of the Hamiltonian $\hat{\boldsymbol{H}}$, defining an influence purely on the bottom graphene layer.

In the absence of the perturbation, $\delta\hat{\boldsymbol{H}} = 0$, and for $u = 0$, the Hamiltonian above results in four bands, two of which are degenerate at the points $\boldsymbol{K}_+$ and $\boldsymbol{K}_-$ at the neutrality point, which we use as the zero of our energy scale. The other two bands are split by $\pm\gamma_1$ away from the neutrality point [17]. The external per-

pendicular electric field breaks the layer symmetry and induces an on-site energy difference between the two graphene layers described by u. This leads to opening of a band gap $E_g \approx u$ (if $u < \gamma_1$) in the electronic spectrum [35].

To arrive at the form of the moiré perturbation in Eq. (2.2), we have assumed that the hexagonal monoatomic layer directly under graphene has inversion symmetry (again, interaction with atoms deeper in the bulk of the substrate are neglected because of the rapid decay of the $2p_z$ wave functions). We also do not consider any intravalley terms as these were studied before [43] and it has been shown that in the case of BLG such intravalley terms tend to open gaps rather than create secondary Dirac points and for that reason taking them into account does not influence the qualitative conclusions of the chapter. The relative strength of the perturbation, measured here in the units of $\sqrt{3}v\beta$, $\beta = |\boldsymbol{\beta}_i|$, is set by three dimensionless parameters $U_{E'}$, U_G, $U_{G'}$. Their exact values depend on the substrate as well as the misalignment angle θ and are difficult to determine due to the van der Waals nature of the interaction between the two constituent materials. However, we assume that the perturbation parameters are small, such that $|U_i| \ll 1$. Finally, we note that for $\theta = 0°$ the reflection axes of the graphene and substrate unit cells coincide and hence these directions remain reflection axes for the superlattice. Two models utilised in order to describe the relative magnitudes of the three perturbation parameters $U_{E'}$, U_G, $U_{G'}$ suggest similar estimates [45]

$$v\beta \{U_{E'}, U_G, U_{G'}\} = \tilde{V} \left\{ \frac{1}{2}, \frac{-\delta}{\sqrt{\delta^2 + \theta^2}}, \frac{\theta}{\sqrt{\delta^2 + \theta^2}} \right\}.$$

However, as a result, a rotationally aligned substrate such that $\theta = 0°$ suggests that $U_{G'} = 0$.

The reciprocal lattice vectors $\{\boldsymbol{\beta}_m\}$ correspond to the real space periodicity set by the lattice vectors of the substrate and the Kekulé lattice of graphene, depicted by vector $\boldsymbol{A}$ in Fig. 2.2a. We demonstrate in the Appendix of this chapter however, that a shorter periodicity of the local atomic arrangement surrounding a carbon atom, indicated in Fig. 2.2 by vector $\tilde{\boldsymbol{A}}$, always exists. This shorter periodicity corresponds to primitive reciprocal lattice vectors $\{\boldsymbol{b}_m\} = \sqrt{3}\hat{R}_{\frac{\pi}{2}}\boldsymbol{\beta}_m$, which define a larger superlattice Brillouin zone, shown in Fig. 2.2b, than the vectors $\{\boldsymbol{\beta}_m\}$ [45]. Alternatively, these $\boldsymbol{b}$ vectors can be seen as the addition of two $\boldsymbol{\beta}$ vectors, for instance $\boldsymbol{b}_5 = \boldsymbol{\beta}_0 + \boldsymbol{\beta}_1$, where we swap valley twice and therefore end in a state with the same valley index we started in. The existence of two periodicities gives rise to the particular combination of functions $f_1(\check{\boldsymbol{\beta}})$ and $f_2(\check{\boldsymbol{\beta}})$ in Eq. (2.2) which always leads to an exact cancellation of half of the terms in the sums over vectors $\{\boldsymbol{\beta}_m\}$. As a result, a state $|+, n, \boldsymbol{p}\rangle$ with momentum $\boldsymbol{p}$ in the vicinity of the valley

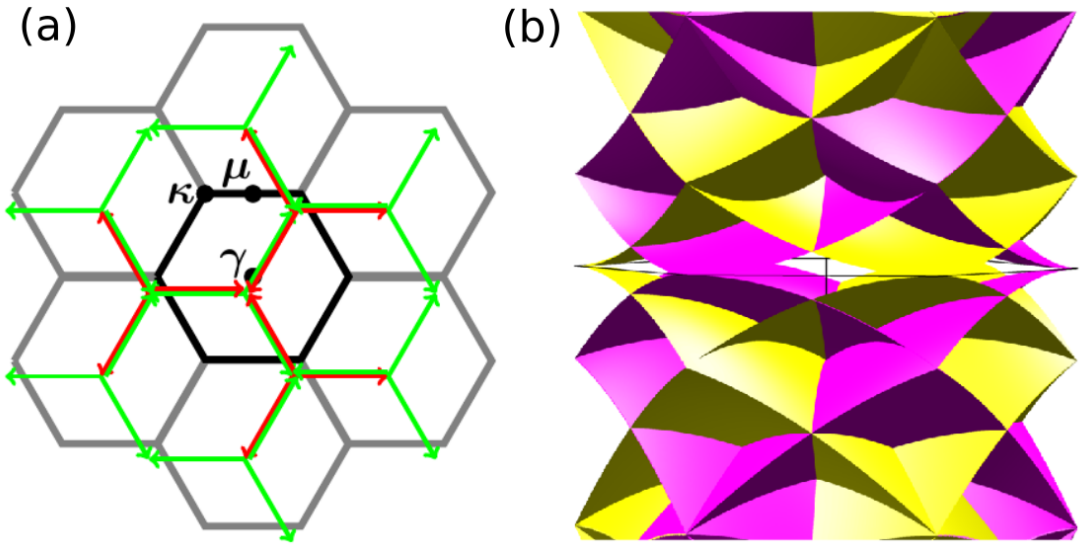

Figure 2.3: (a) Schematic of coupling vectors in momentum space for a generic point within the sBZ (black), truncated to three rings of scattering vectors, just short of the four we utilise in our procedure. Note that the adjacent sBZ are greyed out to demonstrate the fact that we are coupling to energies in the unfolded energy dispersion and thus they are only present to demonstrate the periodicity. (b) Spectrum of bilayer graphene folded onto the sBZ set by vectors $\check{\boldsymbol{b}}_m$. States from the $\boldsymbol{K}_+$ ($\boldsymbol{K}_-$) valley are shown in magenta (yellow).

$\boldsymbol{K}_+$ and with n indexing one of the four BLG bands, is directly coupled by the moiré perturbation to three states $|-, n', \boldsymbol{p} + \boldsymbol{\beta}_m\rangle$, $m = 1, 3, 5$, [shown in green in Fig. 2.2b] in the vicinity of the valley $\boldsymbol{K}_-$. Equivalently, a state $|-, n, \boldsymbol{p}\rangle$ is coupled to the states $|+, n', \boldsymbol{p} + \boldsymbol{\beta}_m\rangle$, $m = 0, 2, 4$ [shown in red in Fig. 2.2b]. Hence, in a reduced zone scheme, the centre of the $\boldsymbol{K}_-$ valley is folded onto momentum $\boldsymbol{\beta}_0$ in the vicinity of the valley $\boldsymbol{K}_+$.

We focus first on the sBZ set by the vectors $\{\boldsymbol{b}_m\}$ and denote its high-symmetry points, as shown in Fig. 2.2b. In order to treat both valleys on an equal footing, we choose the position of the sBZ which reflects best the symmetry of the lattice: the centre of the valley $\boldsymbol{K}_+$ is at the point $\boldsymbol{\kappa}$ and $\boldsymbol{K}_-$ is mapped onto $\boldsymbol{\kappa}'$ [45]. The result of such folding of the unperturbed BLG spectrum is shown in Fig. 2.3b, where we have depicted bands from the $\boldsymbol{K}_+$ ($\boldsymbol{K}_-$) valley in magenta (yellow). To present the dispersion in the smaller sBZ, set by $\{\boldsymbol{\beta}_m\}$, requires additional folding of the bands. This results in the two valleys $\boldsymbol{K}_+$ and $\boldsymbol{K}_-$ being mapped onto the $\boldsymbol{\gamma}$ point, and leads to valley degenerate dispersion surfaces [45]. In general, nesting of minibands makes it more difficult to visualise the dispersion in the smaller sBZ and so, for clarity, in this work we show the minibands within the larger sBZ.

2.3 Effective Hamiltonian at High-Symmetry Points

We assume that $\frac{vb}{\gamma_1} < 1$, requiring a small lattice mismatch δ, and, because we are interested in the reconstruction of the electronic spectrum at the boundary of the first and second miniband, we initially ignore the high-energy split bands. We also assume that $\theta = 0°$ and hence $U_{G'} = 0$. Note that, in the case of the graphene/hBN heterostructure, the effect of the moiré on graphene electrons is most pronounced for small misalignment angles θ [62] and the same should be the case for the heterostructure considered here.

We write the unperturbed plane wave state $|\xi, s, \boldsymbol{p}\rangle$ in the conduction ($s = 1$) or valence ($s = -1$) band, with momentum $\boldsymbol{p} = (p_x, p_y) \neq 0$ in the vicinity of the valley $\boldsymbol{K}_\xi$,

$$|+, s, \boldsymbol{p}\rangle = \frac{1}{\sqrt{C_{p,s}}} \begin{pmatrix} 1 \\ \frac{1}{vp}(\epsilon^0_{p,s} - \frac{u}{2})e^{i\varphi} \\ \frac{1}{\gamma_1}\left[\frac{(\epsilon^0_{p,s} - \frac{u}{2})^2 - v^2p^2}{vp}\right]e^{i\varphi} \\ \frac{1}{\gamma_1}\left[\frac{(\epsilon^0_{p,s} - \frac{u}{2})^2 - v^2p^2}{(\epsilon^0_{p,s} + \frac{u}{2})}\right]e^{i2\varphi} \\ 0 \\ 0 \\ 0 \\ 0 \end{pmatrix} e^{i\boldsymbol{p}\cdot\boldsymbol{r}},$$

$$|-, s, \boldsymbol{p}\rangle = \frac{1}{\sqrt{C_{p,s}}} \begin{pmatrix} 0 \\ 0 \\ 0 \\ 0 \\ \frac{1}{vp}(\epsilon^0_{p,s} - \frac{u}{2})e^{-i\varphi} \\ 1 \\ \frac{1}{\gamma_1}\left[\frac{v^2p^2 - (\epsilon^0_{p,s} - \frac{u}{2})^2}{(\epsilon^0_{p,s} + \frac{u}{2})}\right]e^{-i2\varphi} \\ \frac{1}{\gamma_1}\left[\frac{v^2k^2 - (\epsilon^0_{p,s} - \frac{u}{2})^2}{vp}\right]e^{-i\varphi} \end{pmatrix} e^{i\boldsymbol{p}\cdot\boldsymbol{r}},$$

in a basis $\{\psi^{K_+}_{A1}, \psi^{K_+}_{B1}, \psi^{K_+}_{A2}, \psi^{K_+}_{B2}, \psi^{K_-}_{B1}, -\psi^{K_-}_{A1}, \psi^{K_-}_{B2}, -\psi^{K_-}_{A2}\}^T$,where $\tan\varphi = \frac{p_y}{p_x}$. $C_{p,s}$, the normalisation constant in a specific momentum and band, and $\epsilon^0_{p,s}$, the unperturbed bilayer graphene energy, are given by

$$C_{p,s} = \frac{1}{\gamma_1^2}\left[\frac{(\epsilon^0_{p,s}-\frac{u}{2})^4}{v^2p^2} - (\epsilon^0_{p,s}-\frac{u}{2})^2 - v^2p^2 + \frac{v^4p^4}{(\epsilon^0_{p,s}+\frac{u}{2})^2}\right] + 1 + \frac{(\epsilon^0_{p,s}-\frac{u}{2})^2}{v^2p^2},$$
$$\epsilon^0_{p,s} = s\frac{1}{2}\sqrt{2\gamma_1^2+u^2+4v^2p^2 - \sqrt{\gamma_1^4+4v^2p^2(\gamma_1^2+u^2)}}.$$

The energy equation is re-used from Eq. (1.23), focused on the two bands closest to the neutrality point.

This gives a general coupling $\langle -, s, \boldsymbol{p}|\, \delta\hat{\boldsymbol{H}}\, |+, s', \boldsymbol{p'}\rangle$ of a state with momentum $\boldsymbol{p'}$ intially in the $\boldsymbol{K}_+$ valley and coupled to a state with momentum $\boldsymbol{p}$ (where $\boldsymbol{p} = \boldsymbol{p'} + \boldsymbol{\beta}_i$) in the $\boldsymbol{K}_-$ valley as

$$\begin{aligned}\Delta_{p,s} = \frac{2}{\sqrt{3}}\frac{vb}{\sqrt{C_pC_{p'}}}\Bigg\{ & U_{E'}\left[\frac{(\epsilon^0_{p,s}-\frac{u}{2})}{vp}e^{i\varphi} - \frac{(\epsilon^{0'}_{p,s}-\frac{u}{2})}{vp'}e^{i\varphi'}\right] \\ & + \beta_n^x U_G\left[\frac{(\epsilon^0_{p,s}-\frac{u}{2})(\epsilon^{0'}_{p,s}-\frac{u}{2})}{v^2pp'}e^{i(\varphi+\varphi')} - 1\right] \\ & - i\beta_n^y U_G\left[\frac{(\epsilon^0_{p,s}-\frac{u}{2})(\epsilon^{0'}_{p,s}-\frac{u}{2})}{v^2pp'}e^{i(\varphi+\varphi')} + 1\right]\Bigg\},\end{aligned} \tag{2.3}$$

in which, the apostrophe notation, for instance p', represents the initial state and the lack of apostrophe represent the final state and $\beta_n^{x,y}$ the components of the coupling vector.

2.3.1 μ Point

At the $\boldsymbol{\mu}$ point, shown in Fig. 2.2b as the midway point between the band minima of the corners. Here zone folding brings together two degenerate states, $|+, s, \frac{\boldsymbol{\beta}_1}{2}\rangle$ and $|-, s, -\frac{\boldsymbol{\beta}_1}{2}\rangle$. The two other states linked by $\boldsymbol{\beta}_3$ and $\boldsymbol{\beta}_5$ exist outside the bounds of the first sBZ and therefore are of a much larger energy and can be neglected in this approximation. These couplings are displayed in Fig. 2.4a. Applying degenerate perturbation theory to these two states leads to a 2×2 matrix,

$$\hat{\boldsymbol{H}}_\mu = \begin{pmatrix}\epsilon^0_{\beta/2,s} & \Delta_{\mu,s}\\ \Delta_{\mu,s} & \epsilon^0_{\beta/2,s}\end{pmatrix},$$
$$\Delta_{\mu,s} = -\frac{2vb}{\sqrt{3}C_\mu}\left\{4\sqrt{3}U_{E'}\frac{\left(\epsilon^0_{\beta/2,s}-\frac{u}{2}\right)}{vb} - U_G\left[12\frac{\left(\epsilon^0_{\beta/2,s}-\frac{u}{2}\right)^2}{v^2b^2}+1\right]\right\},$$

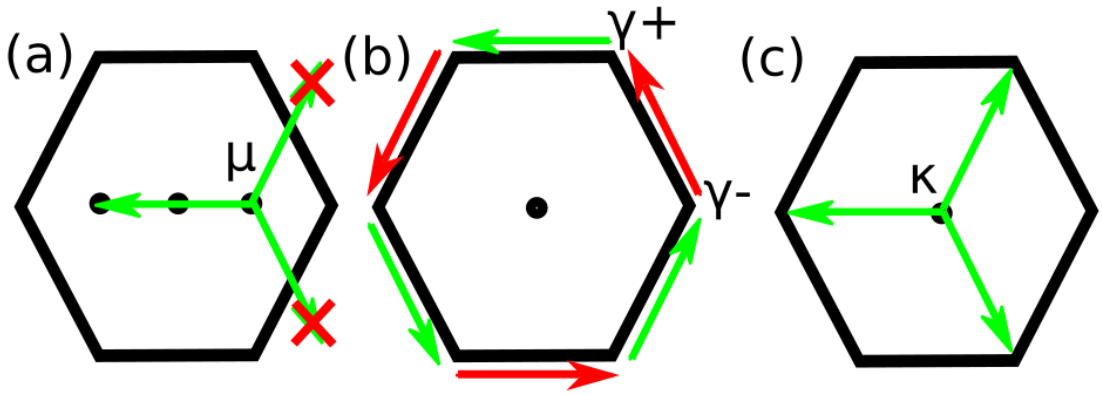

Figure 2.4: Effective coupling at high-symmetry points. Note that the sBZ is shifted such that the parabolic minima of the unperturbed band structure now sits at the middle of the sBZ and therefore the energy of the points coupled to simply increases with increasing distance from the centre. (a) The effective coupling at the μ point, including the two coupling vectors disregarded for coupling to points much larger in energy. (b) Effective coupling at the γ point, showing circular route of equal energy points, constructed by alternating valley coupling vectors. The reverse route is also true, provided we also switch the coupling set we use (in other words, green to red and vice versa), but is omitted for visual clarity. (c) Effective coupling at the κ point. These three coupling vectors are mirrored in both band indices $s \pm 1$, producing a total of six couplings.

and yields the perturbed energies

$$\epsilon^{\pm}_{\mu,s} = \epsilon^{0}_{\beta/2,s} \pm |\Delta_{\mu,s}|. \tag{2.4}$$

2.3.2 γ Point

At the $\boldsymbol{\gamma}$ point, the six following degenerate states are mixed together by the perturbation: $|+,s,\boldsymbol{\beta}_5\rangle$, $|-,s,\boldsymbol{\beta}_0\rangle$, $|+,s,\boldsymbol{\beta}_1\rangle$, $|-,s,\boldsymbol{\beta}_2\rangle$, $|+,s,\boldsymbol{\beta}_3\rangle$ and $|-,s,\boldsymbol{\beta}_4\rangle$. Only the neighbours in the effective ring of six points are directly coupled and the couplings are related by a phase, yielding a 6×6 matrix, as shown in Fig. 2.4b.

$$\hat{\boldsymbol{H}}_{\gamma} = \begin{pmatrix} \epsilon^0_{\beta,s} & \Delta_{\gamma,s}w^* & 0 & 0 & 0 & -\Delta_{\gamma,s} \\ \Delta_{\gamma,s}w & \epsilon^0_{\beta,s} & \Delta_{\gamma,s}w^* & 0 & 0 & 0 \\ 0 & \Delta_{\gamma,s}w & \epsilon^0_{\beta,s} & -\Delta_{\gamma,s} & 0 & 0 \\ 0 & 0 & -\Delta_{\gamma,s} & \epsilon^0_{\beta,s} & \Delta_{\gamma,s}w & 0 \\ 0 & 0 & 0 & \Delta_{\gamma,s}w^* & \epsilon^0_{\beta,s} & \Delta_{\gamma,s}w \\ -\Delta_{\gamma,s} & 0 & 0 & 0 & \Delta_{\gamma,s}w^* & \epsilon^0_{\beta,s} \end{pmatrix},$$

$$\Delta_{\gamma,s} = \frac{2vb}{\sqrt{3}C_{\gamma}} \left\{ \sqrt{3}U_{E'} \frac{\left(\epsilon^0_{\beta,s} - \frac{u}{2}\right)}{vb} - U_G \left[3\frac{\left(\epsilon^0_{\beta,s} - \frac{u}{2}\right)^2}{v^2b^2} + 1 \right] \right\}, w = \exp\left(i\frac{\pi}{3}\right).$$

As a result of the perturbation, the six levels split into two degenerate pairs of levels and two nondegenerate states,

$$\epsilon_{\gamma,s}^{\pm,\mathrm{deg}} = \epsilon_{\beta,s}^{0} \pm |\Delta_{\gamma,s}|, \qquad \epsilon_{\gamma,s}^{\pm} = \epsilon_{\beta,s}^{0} \pm 2|\Delta_{\gamma,s}|. \tag{2.5}$$

2.3.3 κ Point

Finally, at the $\boldsymbol{\kappa}/\boldsymbol{\kappa}'$ point, two (degenerate for $u = 0$) states at the centre of the valley ξ,

$$|+, s, \mathbf{0}\rangle = \begin{pmatrix} \frac{1}{2}|s+1| \\ 0 \\ 0 \\ \frac{1}{2}|s-1| \\ 0 \\ 0 \\ 0 \\ 0 \end{pmatrix}, \quad |-, s, \mathbf{0}\rangle = \begin{pmatrix} 0 \\ 0 \\ 0 \\ 0 \\ 0 \\ \frac{1}{2}|s+1| \\ \frac{1}{2}|s-1| \\ 0 \end{pmatrix},$$

are each coupled to six points $|-\xi, \pm 1, \boldsymbol{\beta}_j\rangle$, where j is odd if $\xi = 1$ and even for $\xi = -1$. This is shown in Fig. 2.4c. However, the moiré perturbation acts only on the bottom graphene layer, see Eq. (2.2), while the state $|\xi, -1, \mathbf{0}\rangle$ is located exclusively on the top layer and, hence, is effectively uncoupled from the other states, its energy, $\epsilon = -\frac{u}{2}$, not affected by the moiré perturbation.

The positions of the entries of the wave function and perturbation and how, starting from the valence band regime, the coupling reduces to zero can be seen below in a layer-valley separated basis of $\left\{\psi_1^{K_+}, \psi_2^{K_+}, \psi_1^{K_-}, \psi_2^{K_-}\right\}$

$$\langle -\xi, -1, \boldsymbol{\beta}_j | \, \delta\hat{\boldsymbol{H}} \, |\xi, -1, \mathbf{0}\rangle = \left(\dots\right) \begin{pmatrix} 0 & 0 & \delta\hat{\boldsymbol{H}} & 0 \\ 0 & 0 & 0 & 0 \\ \delta\hat{\boldsymbol{H}}^\dagger & 0 & 0 & 0 \\ 0 & 0 & 0 & 0 \end{pmatrix} \begin{pmatrix} 0 \\ \Delta \\ 0 \\ 0 \end{pmatrix} = 0.$$

The remaining seven coupled points in momentum space lead to the matrix,

$$\hat{\boldsymbol{H}}_\kappa = \begin{pmatrix} \frac{u}{2} & \hat{\boldsymbol{T}}_1 & \hat{\boldsymbol{T}}_2 \\ \hat{\boldsymbol{T}}_1^\dagger & \hat{\boldsymbol{H}}^0_{\kappa,1} & 0 \\ \hat{\boldsymbol{T}}_2^\dagger & 0 & \hat{\boldsymbol{H}}^0_{\kappa,-1} \end{pmatrix}, \quad \hat{\boldsymbol{H}}^0_{\kappa,s} = \begin{pmatrix} \epsilon^0_{\beta,s} & 0 & 0 \\ 0 & \epsilon^0_{\beta,s} & 0 \\ 0 & 0 & \epsilon^0_{\beta,s} \end{pmatrix},$$
$$\hat{\boldsymbol{T}}_1 = \begin{pmatrix} \Delta_{\kappa,1} w & -\Delta_{\kappa,1} & \Delta_{\kappa,1} w^* \end{pmatrix}, \quad \hat{\boldsymbol{T}}_2 = \begin{pmatrix} \Delta_{\kappa,-1} w & -\Delta_{\kappa,-1} & \Delta_{\kappa,-1} w^* \end{pmatrix},$$
$$\Delta_{\kappa,s} = \frac{2vb}{\sqrt{3C_\beta}} \left\{ \sqrt{3} U_{E'} \frac{\left(\epsilon^0_{\beta,s} - \frac{u}{2}\right)}{vb} - U_G \right\}.$$

For both $u \ll \epsilon^0_{\beta,s}$ and $|\Delta_{\kappa,s}| \ll \epsilon^0_{\beta,s}$, we can use a variation on the Schrieffer-Wolff transformation [71] in an attempt to project the Hamiltonian above onto the low-energy state $|\xi, \mathbf{0}\rangle_1$. This requires rescaling of the zero-energy to the value found at the $\boldsymbol{\kappa}$ point and the solution of a Schrödinger equation of form

$$\begin{pmatrix} 0 & \hat{\boldsymbol{T}}_1 & \hat{\boldsymbol{T}}_2 \\ \hat{\boldsymbol{T}}_1^\dagger & \hat{\boldsymbol{H}}^0_{\kappa,1} & 0 \\ \hat{\boldsymbol{T}}_2^\dagger & 0 & \hat{\boldsymbol{H}}^0_{\kappa,-1} \end{pmatrix} \begin{pmatrix} \psi_1 \\ \psi_2 \\ \psi_3 \end{pmatrix} = \epsilon_\kappa \begin{pmatrix} \psi_1 \\ \psi_2 \\ \psi_3 \end{pmatrix}.$$

The three equations formed by this relation can be rearranged to form

$$\frac{\hat{\boldsymbol{T}}_1 \hat{\boldsymbol{T}}_1^\dagger}{-\epsilon^0_{\beta,1} + \epsilon_{\kappa,\Delta}} \psi_1 + \frac{\hat{\boldsymbol{T}}_2 \hat{\boldsymbol{T}}_2^\dagger}{\epsilon^0_{\beta,1} + \epsilon_{\kappa,\Delta}} \psi_1 = \epsilon_{\kappa,\Delta} \psi_1,$$

within which we have also recognised that $\epsilon^0_{\beta,-1} = -\epsilon^0_{\beta,1}$. We use a Taylor expansion, that we truncate to the linear term, of form

$$\frac{1}{(1-x)} \approx 1 + x + ...,$$

to expand around our energy point, resulting in

$$\left\{ -\frac{1}{\epsilon^0_{\beta,1}\left(1 - \frac{\epsilon_{\kappa,\Delta}}{\epsilon^0_{\beta,1}}\right)} \hat{\boldsymbol{T}}_1 \hat{\boldsymbol{T}}_1^\dagger + \frac{1}{\epsilon^0_{\beta,1}\left(1 + \frac{\epsilon_{\kappa,\Delta}}{\epsilon^0_{\beta,1}}\right)} \hat{\boldsymbol{T}}_2 \hat{\boldsymbol{T}}_2^\dagger \right\} \psi_1 = \epsilon_{\kappa,\Delta} \psi_1,$$
$$\left\{ -\frac{1}{\epsilon^0_{\beta,1}} \left[1 + \frac{\epsilon_{\kappa,\Delta}}{\epsilon_{\beta,1}}\right] \hat{\boldsymbol{T}}_1 \hat{\boldsymbol{T}}_1^\dagger + \frac{1}{\epsilon^0_{\beta,1}} \left[1 - \frac{\epsilon_{\kappa,\Delta}}{\epsilon_{\beta,1}}\right] \hat{\boldsymbol{T}}_2 \hat{\boldsymbol{T}}_2^\dagger \right\} \psi_1 = \epsilon_{\kappa,\Delta} \psi_1,$$

which with rearrangement becomes

$$\epsilon^0_{\beta,1}\left\{\epsilon^{02}_{\beta,1} + \hat{\boldsymbol{T}}_1\hat{\boldsymbol{T}}_1^\dagger + \hat{\boldsymbol{T}}_2\hat{\boldsymbol{T}}_2^\dagger\right\}^{-1}\left\{-\hat{\boldsymbol{T}}_1\hat{\boldsymbol{T}}_1^\dagger + \hat{\boldsymbol{T}}_2\hat{\boldsymbol{T}}_2^\dagger\right\}\psi_1 = \epsilon_{\kappa,\Delta}\psi_1,$$

and recognition that $\epsilon_\kappa \gg \hat{\boldsymbol{T}}_1\hat{\boldsymbol{T}}_1^\dagger, \hat{\boldsymbol{T}}_2\hat{\boldsymbol{T}}_2^\dagger$ gives

$$\frac{1}{\epsilon^0_{\beta,1}}\left\{\hat{\boldsymbol{T}}_2\hat{\boldsymbol{T}}_2^\dagger - \hat{\boldsymbol{T}}_1\hat{\boldsymbol{T}}_1^\dagger\right\}\psi_1 = \epsilon_{\kappa,\Delta}\psi_1,$$

As a final result, we obtain the shift of its energy $\epsilon_{\kappa,\Delta}$ from $\epsilon = \frac{u}{2}$ due to the perturbation,

$$\epsilon_\kappa \approx \frac{u}{2} + 8\sqrt{3}vbU_{E'}U_G. \tag{2.6}$$

We require these results in order to make statements about how the perturbation affects certain high-symmetry points of the sBZ and how they can be utilised to predict the formation of mini-gaps in the spectrum - this is discussed later in the chapter, but provided here in order to describe an analytical version of the calculation provided in the next section, that is used to calculated the full mini-band spectrum.

2.4 Description of Matlab Procedure for Calculation of Dispersion

2.4.1 Energy Bands

In order to construct the superlattice miniband structures induced by the substrate perturbation, we use an effective Hamiltonian approach that expands upon the approximations discussed above, and solves the perturbation theory problem we recast from Eq. (2.2) as

$$\hat{\boldsymbol{H}} = \hat{\boldsymbol{H}}_{\text{BLG}} + \Delta\hat{\boldsymbol{H}}, \quad \hat{\boldsymbol{H}}_{\text{BLG}} = \begin{pmatrix} \hat{\boldsymbol{H}}_{\text{MLG}} + \frac{u}{2} & \hat{\boldsymbol{T}} \\ \hat{\boldsymbol{T}}^\dagger & \hat{\boldsymbol{H}}_{\text{MLG}} - \frac{u}{2} \end{pmatrix}, \Delta\hat{\boldsymbol{H}} = \begin{pmatrix} \delta\hat{\boldsymbol{H}} & 0 \\ 0 & 0 \end{pmatrix},$$

in a layer separated basis. Upon defining the confines of the superlattice BZ and thus the coupling vectors needed using Eq. (2.1) and $\boldsymbol{\beta}_m = \frac{1}{\sqrt{3}}\hat{\boldsymbol{R}}_{-\frac{\pi}{2}}\boldsymbol{b}_m$, we construct a large coupling network that spans 31 of the closest points in momentum space, corresponding to four 'rings' of scattering vectors and noting again that each hopping in $\boldsymbol{\beta}_i$ changes the valley sign ξ and thus the coupling vectors that can be

applied. An example can be seen in Fig. 2.3a. As shown in the expansions around the high-symmetry points, a point in the $\boldsymbol{K}_+$ valley is coupled to three states in the $\boldsymbol{K}_-$ valley via $\boldsymbol{\beta}_{1,3,5}$, seen in green in Fig. 2.2b. The effective Hamiltonian used can therefore be thought of as a generalised expansion of the exact point approach above. From a starting point in the $\boldsymbol{K}_+$ valley (there is an equivalent form for the opposite valley, with vector set changed from odd to even numbered $\boldsymbol{\beta}$), we construct

$$\hat{\boldsymbol{H}} \approx \begin{pmatrix} \boldsymbol{\epsilon}_{\boldsymbol{p}}^{s,\alpha} & \boldsymbol{\Delta}_{\boldsymbol{p},\boldsymbol{p}+\boldsymbol{\beta}_1} & \boldsymbol{\Delta}_{\boldsymbol{p},\boldsymbol{p}+\boldsymbol{\beta}_3} & \boldsymbol{\Delta}_{\boldsymbol{p},\boldsymbol{p}+\boldsymbol{\beta}_5} & \dots \\ \boldsymbol{\Delta}^*_{\boldsymbol{p},\boldsymbol{p}+\boldsymbol{\beta}_1} & \boldsymbol{\epsilon}_{\boldsymbol{p}+\boldsymbol{\beta}_1}^{s,\alpha} & 0 & 0 & \dots \\ \boldsymbol{\Delta}^*_{\boldsymbol{p},\boldsymbol{p}+\boldsymbol{\beta}_3} & 0 & \boldsymbol{\epsilon}_{\boldsymbol{p}+\boldsymbol{\beta}_3}^{s,\alpha} & 0 & \dots \\ \boldsymbol{\Delta}^*_{\boldsymbol{p},\boldsymbol{p}+\boldsymbol{\beta}_5} & 0 & 0 & \boldsymbol{\epsilon}_{\boldsymbol{p}+\boldsymbol{\beta}_5}^{s,\alpha} & \dots \\ \vdots & \vdots & \vdots & \vdots & \ddots \end{pmatrix}.$$

This expands onward to a 31×31 form, to ensure numerical convergence of the mini-band spectrum, within which each entry is a 4×4 matrix, corresponding to the four energy bands present at each point in momentum space in the general bilayer graphene Hamiltonian - both the upper and lower energy within the conduction and valence bands. We assume that each hopping couples to all four possible bands, in order to provide a more complete picture of the miniband representation up to high energy values. This gives the diagonal energy entries form

$$\boldsymbol{\epsilon}_{\boldsymbol{p}}^{s,\alpha} = \begin{pmatrix} \epsilon_{\boldsymbol{p}}^{1,-1} & 0 & 0 & 0 \\ 0 & \epsilon_{\boldsymbol{p}}^{-1,-1} & 0 & 0 \\ 0 & 0 & \epsilon_{\boldsymbol{p}}^{1,1} & 0 \\ 0 & 0 & 0 & \epsilon_{\boldsymbol{p}}^{-1,1} \end{pmatrix},$$

where s refers to the conduction and valence bands, as before, and $\alpha = -1$ and $\alpha = 1$ refer to the lower and upper band respectively.

The off-diagonal terms corresponding to coupling between two points in momentum space and have a similar 4×4 layout per entry. Each component, again starting in the $\boldsymbol{K}_+$ valley, is constructed via

$$\Delta^{s,s',\alpha,\alpha'}_{\boldsymbol{p},\boldsymbol{p}+\boldsymbol{\beta}_i} = \langle -, s, \alpha, \boldsymbol{p}+\boldsymbol{\beta}_i | \, \hat{\boldsymbol{H}}_{\mathrm{BLG},\boldsymbol{p}} \, | +, s', \alpha', \boldsymbol{p} \rangle + \langle -, s, \alpha, \boldsymbol{p}+\boldsymbol{\beta}_i | \, \Delta\hat{\boldsymbol{H}}_{\boldsymbol{\beta}_i} \, | +, s', \alpha', \boldsymbol{p} \rangle .$$

With $\Delta\hat{\boldsymbol{H}}$ set to zero and no external potential incident on the system, we re-

turn the dispersion folding shown in Fig. 2.3b by numerical diagonalization of the effective Hamiltonian built of 31 points coupled by the moiré perturbation, including the initial point $|+, s, \alpha, \boldsymbol{p}\rangle$ (mixing of the valleys ensures that the miniband structure calculated for the choice of the initial point $|-, n, \boldsymbol{k}\rangle$ is identical).

2.4.2 Density Of States

The procedure for calculations of the density of states involves randomly sampling the energy bands of many points in a large range of momentum space, folding them back into the superlattice BZ using the intrinsic vector set $\{\boldsymbol{\beta}_m\}$. The density of states is then approximated by counting the change in the number of states in a small energy division. This process is then averaged over many iterations, tending toward the true density of states with increasing number of sample sets.

2.5 Miniband Spectrum

We take into account states in all four of the BLG bands and to set the geometry, we choose In_2Te_2, a semiconductor with a band gap of ~ 2eV [72], as the intended substrate (a short discussion of other potential substrates can be found in Ref. [45] and within the Appendix). This sets the lattice mismatch $\delta = -0.007$ [64, 72] and the characteristic energy of the moiré $\sqrt{3}v\beta = vb = 0.134$eV.

We are interested in determining the conditions for which the first and second miniband on the conduction/valence-band side are separated by a gap, combining both the analytical and numerical approaches detailed in the previous two sections. In what follows, we focus primarily on the valence-band side but the respective conditions for the conduction band side can be obtained by taking advantage of the symmetry of the miniband spectrum,

$$\epsilon_{\boldsymbol{p}}^{U_{E'},U_G,U_{G'},u} = -\epsilon_{\boldsymbol{p}}^{-U_{E'},U_G,U_{G'},-u}. \tag{2.7}$$

In the presence of a weak perturbation, in order to confirm the presence of a band gap between the first and second miniband, it is enough to analyse energy states at the high-symmetry points. Ignoring the Mexican-hat features created at the valence band edge by nonzero interlayer asymmetry u, [35] the highest (closest to the neutrality point) point in the first miniband is the centre of the valley at $\boldsymbol{\kappa}/\boldsymbol{\kappa}'$ at energy $\epsilon = \min(\epsilon_\kappa, -\frac{u}{2})$. Because the unperturbed BLG dispersion has circular symmetry and electron energy in the valence band decreases away from the centre of the valley, the point with the lowest energy in the first miniband is

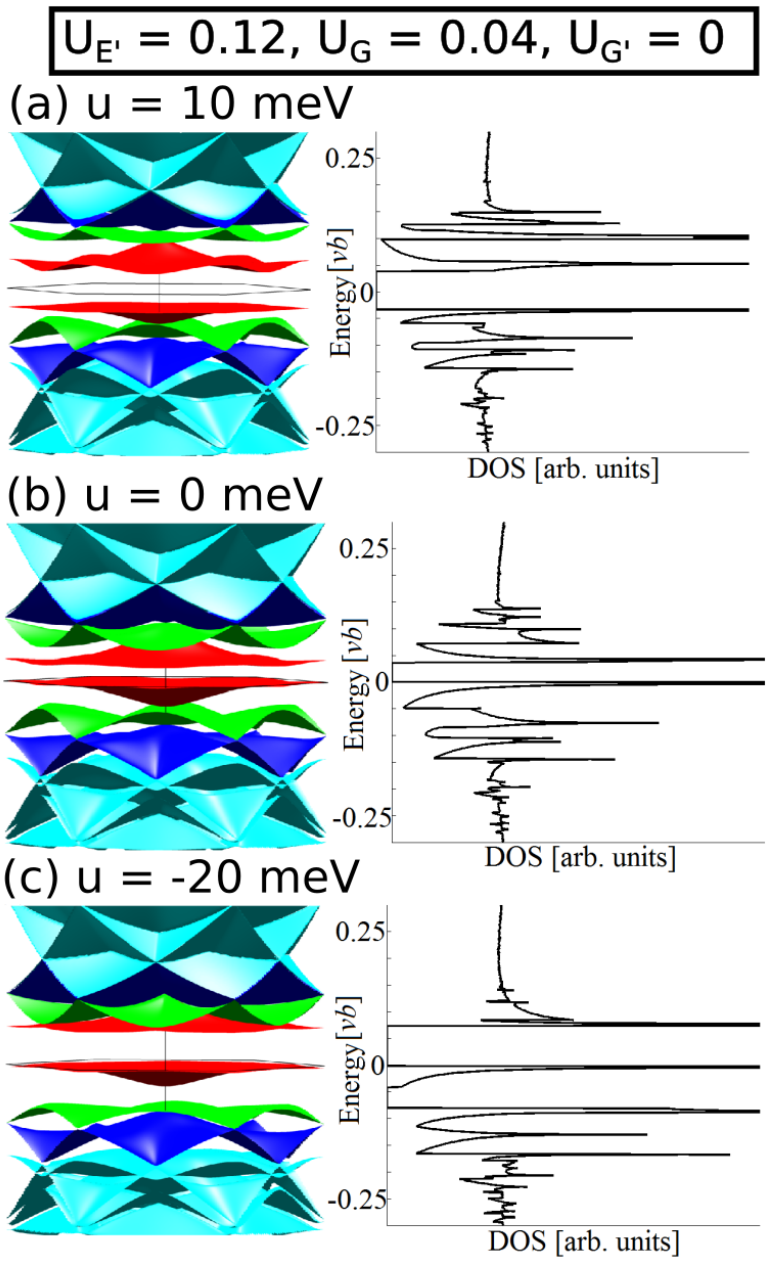

Figure 2.5: (a)-(c) Moiré miniband spectra and density of states (DOS) corresponding to characteristic behaviors of the miniband spectrum that highlight the occurance of an isolated miniband under a varying external potential. Figure reprinted from Ref. [46], copyright (2016), with permission from the American Physical Society.

that furthest away from the centre of the valley, the $\boldsymbol{\gamma}$ point, with energy $\epsilon^{+}_{\gamma,-1}$, Eq. (2.5). In turn, the point with the highest energy in the second miniband is the $\boldsymbol{\mu}$ point which lies in the middle of the shortest line segment connecting two valleys, with energy $\epsilon^{-}_{\mu,-1}$, Eq. (2.4). In other words, we seek to find the conditions under which

$$\begin{aligned} \epsilon_{\gamma,-1,1\mathrm{st}} &> \epsilon_{\mu,-1,2\mathrm{nd}}, \\ \epsilon^{0}_{\beta,-1} + 2|\Delta_{\gamma,-1}| &> \epsilon^{0}_{\beta/2,-1} - |\Delta_{\mu,-1}|. \end{aligned} \tag{2.8}$$

In contrast to monolayer graphene [45], in BLG the energies of the extremal points of a miniband can be modified by tuning the interlayer asymmetry parameter, u, through application of an external electric field perpendicular to the graphene layers. Nonzero u is known to open a gap at the neutrality point. Here, depending on the sign and magnitude of u, one could open and close an additional band gap in the band structure, between the first and second miniband.

An example of such tuning of the miniband spectrum is shown in Fig. 2.5, where we show the miniband spectra for $U_{E'} = 0.12$, $U_G = 0.04$ and $U_{G'} = 0$ and three different values of u, with the additional band gap visible in the spectrum in (c). For $u = 10$ meV, Fig. 2.5a, the miniband spectrum contains a single band gap at the neutrality point, $E_g \approx u$. As the interlayer asymmetry is decreased, the band gap decreases and for $u = 0$meV, Fig. 2.5b, the gap is purely a consequence of the moiré perturbation, $E_g \approx 8\sqrt{3}vbU_{E'}U_G$. Reversal of the sign of u leads to a closure of the band gap when the effect of the electric field cancels that of the moiré perturbation, see the Appendix for further details. Further increase of the magnitude of u, Fig. 2.5c, again opens a band gap at the neutrality point. However, it also opens a band gap, $E'_g \approx |\Delta_{\mu,-1}| + 2|\Delta_{\gamma,-1}|$, between the first and second miniband in the valence band. The isolated valence miniband itself would have a width of

$$\begin{aligned} \epsilon_W &= \epsilon_{\kappa,-1} - \epsilon_{\gamma,-1}, \\ \epsilon_W &= -\frac{|u|}{2} - 8\sqrt{3}vbU_{E'}U_G - \epsilon^{0}_{\beta,-1} - 2|\Delta_{\gamma,-1}|. \end{aligned}$$

The presence of band gaps in the miniband spectrum can be further confirmed through investigation of the density of states (DOS), shown to the right of each of the miniband spectra in Fig. 2.5. Accordingly, in Fig. 2.5c, the DOS vanishes

both in the vicinity of the neutrality point as well as below the first Van Hove singularity in the valence band.

In Fig. 2.6, we display the results of our study of the miniband spectrum for a generic moiré perturbation described by parameters $U_{E'}$ and U_G for various u. The blue-coloured region (I) shows the range of parameters $U_{E'}$ and U_G for which a band gap between the first and second miniband in the valence band exists. The region (II) in white corresponds to the case of overlapping minibands. While the diagram has been produced by inspecting numerically calculated miniband structures, the red dashed line indicates the boundary between the regions (I) and (II) as predicted by the analytical considerations presented in the previous section and inspection of the energy states at the high-symmetry points, as seen in Eq. (2.8). The discrepancy between the numerical and analytical solutions results from the fact that the analytical solution is an approximated solution, first-order in the perturbation constants, and describes the general trend of the inequality. The miniband spectra shown in Fig. 2.5 correspond to the moiré parameter set indicated by the green dot in the diagrams in Fig. 2.6(a)-(c).

In general, greater magnitudes of the perturbation parameters promote appearance of the band gap between the first and second miniband for smaller u. However, the effect of the parameter U_G, describing the sublattice-conserving part of the moiré perturbation, is more significant than that of the parameter $U_{E'}$, characterising the sublattice-exchange part of the perturbation. Also, the threshold value of the interlayer asymmetry u necessary to open the band gap between the first and second miniband for a set moiré perturbation is different for different signs of u.

2.6 Summary

We have discussed the generic miniband structure of the van der Waals heterostructure of bilayer graphene and a semiconducting substrate almost commensurate with the tripled unit cell of graphene. We showed that the combination of an external electric field normal to the graphene layers, which modifies the band structure in the vicinity of the neutrality point, and the miniband formation due to the substrate allow a new degree of tunability in the graphene band structure - the miniband structure can be tuned from the gapless form to that displaying two band gaps, one at the neutrality point and one between the first and second miniband on the conduction/valence-band side, hence isolating a single miniband from the rest of the spectrum.

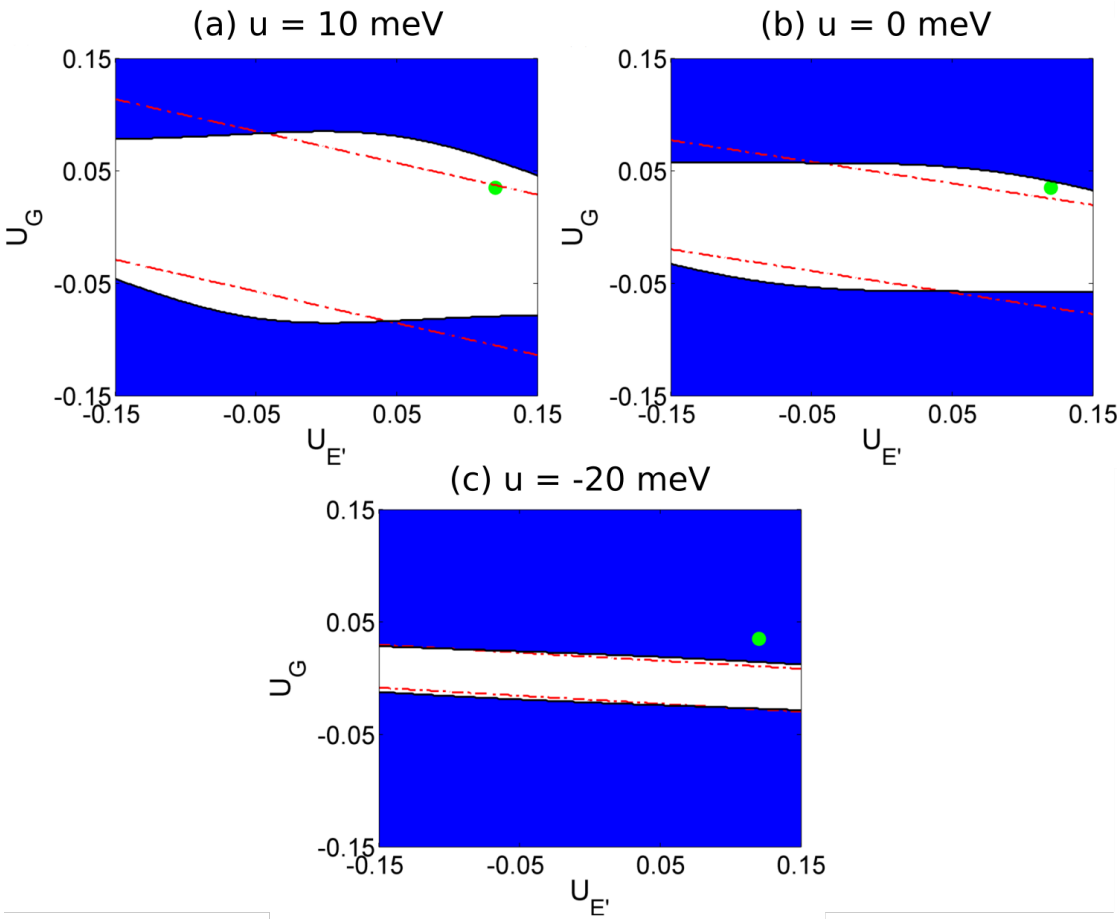

Figure 2.6: Regimes of miniband spectra in the $(U_{E'}, U_G)$ parameter space for the heterostructure of BLG and In_2Te_2 ($\delta = -0.007$) and (a) $u = 10$ meV, (b) $u = 0$ meV and (c) $u = -20$ meV. For the region in blue, a global gap separates the first and second miniband on the valence side. The white region corresponds to the overlapping first and second minibands. The dashed red line represents the boundary between the blue and white regions as obtained using the analysis of the high-symmetry points in the sBZ in Section 2.3. The green dot represents the point in $(U_{E'}, U_G)$ space for which miniband spectra are shown in Fig. 2.5. Figure reprinted from Ref. [46], copyright (2016), with permission from the American Physical Society.

For the case of the lattice mismatch $\delta = -0.007$, corresponding to the choice of In_2Te_2 as the substrate, and mismatch angle $\theta = 0°$, such an isolated miniband could be realised by using relatively weak, experimentally accessible electric fields.

2.A Superlattice Periodicities for Graphene on Incommensurate $\sqrt{3} \times \sqrt{3}$ Substrate

Here, we demonstrate that presence of the moiré superlattice set by the graphene Kekulé lattice and the substrate implies that a superlattice with a shorter period, generated by the substrate and the graphene lattice, also exists.

The substrate is almost commensurate with the Kekulé lattice of graphene and as a result, a new long wavelength periodicity forms at the interface between the two crystals. A continuum model can be constructed if the structure is close to a commensurate geometry [40, 73] and here we assume that the unit vector $\boldsymbol{A}$ of the superlattice can be expressed in terms of the lattice vectors of the substrate and graphene Kekulé lattice so that

$$\boldsymbol{A} = m\left(2\boldsymbol{a}_1 + \boldsymbol{a}_2\right) + n\left(\boldsymbol{a}_1 + 2\boldsymbol{a}_2\right) = \sqrt{1+\delta}\hat{\boldsymbol{R}}_\theta(p\tilde{\boldsymbol{a}}_1 + q\tilde{\boldsymbol{a}}_2)\,, \tag{2.9}$$

where $\boldsymbol{a}_1 = a(\frac{1}{2}, \frac{\sqrt{3}}{2})$ and $\boldsymbol{a}_2 = a(\frac{1}{2}, -\frac{\sqrt{3}}{2})$ are the unit vectors of graphene, $\tilde{\boldsymbol{a}}_1 = a(\frac{3}{2}, \frac{\sqrt{3}}{2})$ and $\tilde{\boldsymbol{a}}_2 = a(\frac{3}{2}, \frac{-\sqrt{3}}{2})$ are the unit vectors of the Kekulé lattice of graphene and m, n, p and q are integers. This periodicity gives rise to the primitive reciprocal vectors $\{\boldsymbol{\beta}_m\}$.

The above condition can be cast in the matrix form [74]

$$\begin{pmatrix} m \\ n \end{pmatrix} = \sqrt{1+\delta}\begin{pmatrix} \cos\theta + \frac{1}{\sqrt{3}}\sin\theta & \frac{2}{\sqrt{3}}\sin\theta \\ -\frac{2}{\sqrt{3}}\sin\theta & \cos\theta - \frac{1}{\sqrt{3}}\sin\theta \end{pmatrix}\begin{pmatrix} p \\ q \end{pmatrix},$$

mapping one pair of integers to another. The necessary and sufficient condition for both to be integers [74] is that the elements of the matrix above assume rational values,

$$\sqrt{1+\delta}\frac{1}{\sqrt{3}}\sin\theta = \frac{i_1}{i_3}, \sqrt{1+\delta}\cos\theta = \frac{i_2}{i_3}. \tag{2.10}$$

Let us now investigate a vector $\tilde{\boldsymbol{A}}$, equivalent to the vector $\boldsymbol{A}$ from Eq. (2.9) rotated by $\frac{\pi}{6}$ and shorter by $\frac{1}{\sqrt{3}}$. We have for the left-hand side

$$\tilde{\boldsymbol{A}} = \frac{1}{\sqrt{3}}\hat{\boldsymbol{R}}_{\pi/6}\left\{m\left(2\boldsymbol{a}_1 + \boldsymbol{a}_2\right) + n\left(\boldsymbol{a}_1 + 2\boldsymbol{a}_2\right)\right\} = (m+n)\,\boldsymbol{a}_1 + n\boldsymbol{a}_2.$$

For the vector above to describe a periodic structure formed by the lattice of the substrate and the lattice of graphene, we require similarly to Eq. (2.9) that

$$(m+n)\,\boldsymbol{a}_1 + n\boldsymbol{a}_2 = \sqrt{1+\delta}\hat{\boldsymbol{R}}_\theta\left(P\tilde{\boldsymbol{a}}_1 + Q\tilde{\boldsymbol{a}}_2\right),$$

where P and Q are also integers. This can be written as

$$\begin{pmatrix} m \\ n \end{pmatrix} = \sqrt{1+\delta} \begin{pmatrix} \cos\theta + \sqrt{3}\sin\theta & -\cos\theta + \sqrt{3}\sin\theta \\ \cos\theta - \sqrt{3}\sin\theta & 2\cos\theta \end{pmatrix} \begin{pmatrix} P \\ Q \end{pmatrix}.$$

Notice that the entries in the matrix above have to be rational because, from Eq. (2.10),

$$\sqrt{1+\delta}\sqrt{3}\sin\theta = 3\frac{i_1}{i_3}, \quad \sqrt{1+\delta}\cos\theta = \frac{i_2}{i_3}. \tag{2.11}$$

Hence, if the substrate and Kekulé lattices form a superlattice with a unit vector $\boldsymbol{A}$, then the substrate and graphene lattices form a superlattice with a unit vector $\tilde{\boldsymbol{A}} = \frac{1}{\sqrt{3}}\hat{\boldsymbol{R}}_{\pi/6}\boldsymbol{A}$, as shown in Fig. 2.2a. The primitive reciprocal lattice vectors corresponding to the latter, shorter periodicity are rotated by $\frac{\pi}{6}$ with respect to $\{\boldsymbol{\beta}_m\}$ and are $\sqrt{3}$ times longer, this is equivalent to the definition of the vectors $\{\boldsymbol{b}_m\}$ in the main text.

2.B Alternative Substrates

Throughout this chapter, we have focused primarily on one substrate of choice, In_2Te_2, in order to show the full numerical analysis for what we believe to be the most immediately promising substrate candidate. However, we are not limited purely to this material and there are other possibilities that adhere to the structural periodicity we require for this effect, as discussed in Ref. [45]. Each material has a distinct lattice constant and therefore a unique superlattice period and sBZ vector set. This additionally means that each one requires varying combinations of perturbation constants and external field in order to introduce a secondary gap to the electronic spectra.

We typically seek to reduce δ as much as possible — this folds the minibands more tightly and means that a set increase in u will have generally have a more profound effect. However, we are effectively limited to the δ values given by the materials currently isolated or hypothesised, thus we focus on and compare the three materials closest to the commensurate case that have a substantial band gap (> 1eV). This corresponds to In_2Te_2 ($\delta = -0.007$) [72], InP(111)B ($\delta = -0.026$) [75] and h-GaTe ($\delta = -0.052$) [76].

All three setups are shown in Fig. 2.7 with a perturbation of $U_{E'} = U_G = 0.05$ and varying external potential values in order to highlight the changing effect of the variable with increasing δ. With the sBZ increasing in size, the secondary

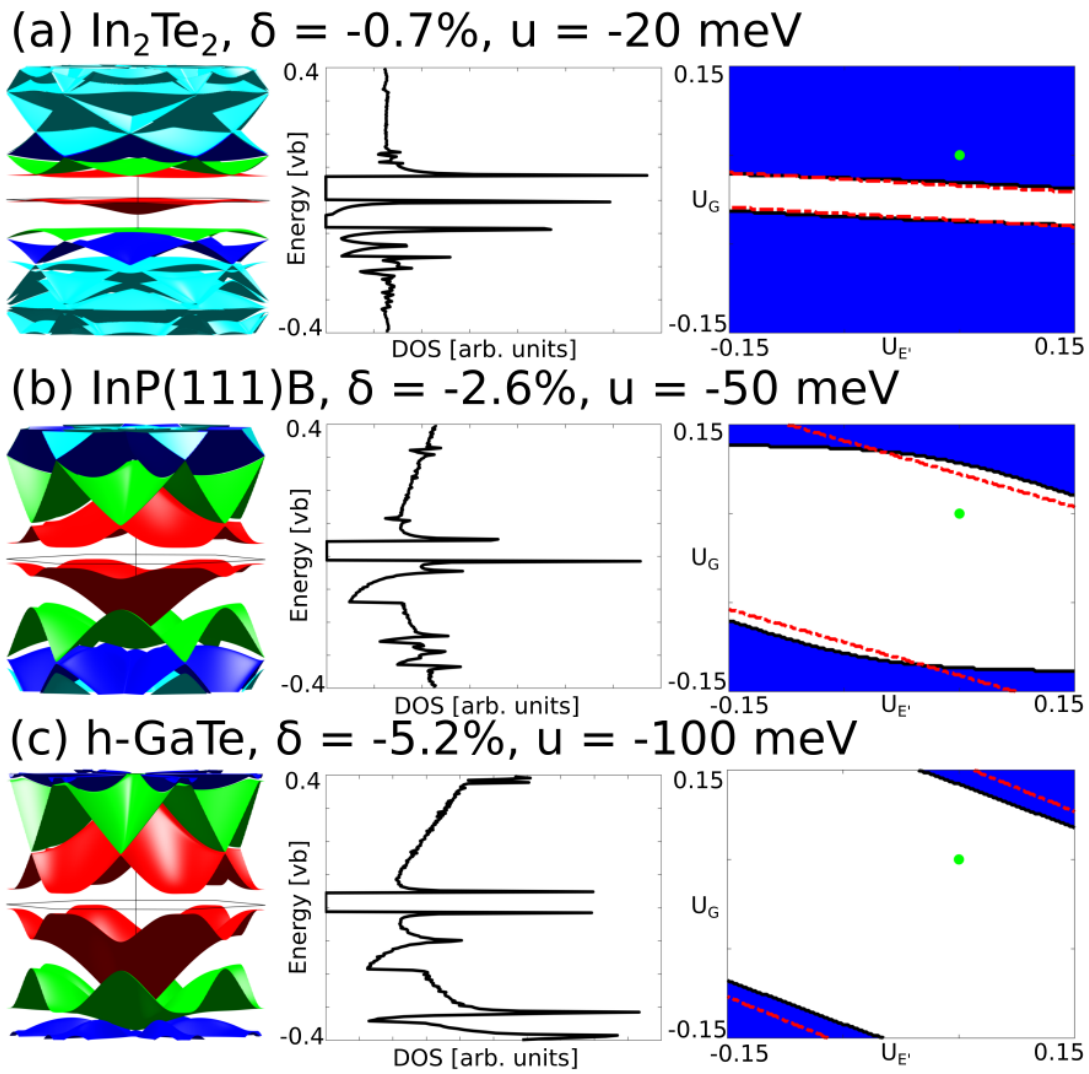

Figure 2.7: Band structure, density of states and parameter space diagrams for comparison of three differing materials that adhere to the structural symmetry we require; (a) In_2Te_2 at $u = -20$meV, (b) InP(111)B at $u = -50$meV and (c) h-GaTe at $u = -100$meV.

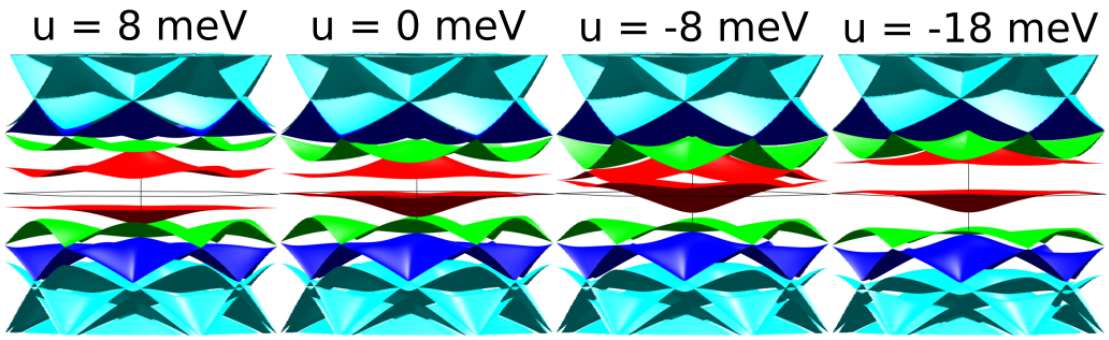

Figure 2.8: Miniband structure displaying the four possible gaps states seen in a general system, induced simply by varying u. We set δ such that it adheres to In_2Te_2, as in the main text. From left to right they display; a central gap (induced by substrate perturbation and external potential) at $u = 8$meV, a central gap (induced purely by substrate perturbation) at $u = 0$meV, a secondary gap (the central gap closed by matching the substrate perturbation) at $u = -8$meV and two gaps (the secondary gap isolated by gaps above and below) at $u = -18$meV.

gap can be seen to be increasingly harder to induce with the parameter space investigated, however the general band structure remains quite similar — a gap separating the conduction and valence bands and the flattening of the secondary miniband in the presence of u. Addtionally, the energy scale of each is scaled via a vb dependence, suggesting the gaps (visually of similar widths) increase in size as the lattice constants misalign further in value.

This allows us to make a more generic statement about the hypothetical 'perfect' substrate for this device. It would have a δ value in the range between In_2Te_2 ($\delta = -0.007$) and InP(111)B ($\delta = -0.026$), in order to balance the need for small δ values that more easily induce the secondary gap and large δ values that maximise the size of the gaps. The perturbation would ideally be as large in magnitude as possible, especially favouring higher values in the sublattice-conserving part of the moiré perturbation U_G, and finally it would contain a large band gap centred around the neutrality point in graphene in order to minimise hybridisation between the two component materials.

2.C Closing the Central Gap

One final gap-related state exists for a generic device of this structure — the closing of the central gap between the conduction and valence bands through balancing the effects of the perturbation and the external potential. Thus for any given substrate and perturbation combination that allows for a secondary gap, we instead cycle through four possible gapped energy band structures rather than just

the three displayed in Fig. 2.5. These, ordered in a manner of increasing u as in Fig. 2.8, consist of:

1. A large central gap, perturbation induced and enhanced by the presence of u.

2. A central gap, purely perturbation induced.

3. A secondary gap with the central gap closed by the interaction between the substrate perturbation and the external potential applied.

4. A large central gap, perturbation induced and enhanced by the presence of u, and a secondary gap between the first and second miniband, induced by u. This state can occur in the conduction band or the valence band or, more typically, both - this is dependent on the perturbation constants involved.

We minimise the central gap using the relation for the perturbed energy bands of the point lowest in energy within the first miniband, the κ point, as seen in Eq. (2.6). We rearrange such that

$$\epsilon_\kappa \approx 0, \quad \rightarrow \quad \frac{u}{2} \approx -8\sqrt{3}vbU_{E'}U_G \tag{2.12}$$

Chapter 3

Valley-polarised tunnelling current in a vertically stacked MLG-hBN-BLG heterostructure

The work in this chapter was done in collaboration with J. J. P. Thompson, who provided the electrostatic model of the device and the basis for the tunnelling current model. These are reproduced here, with permission, in order to provide a complete description of the results.

3.1 Introduction

Van der Waals heterostructures of stacked 2D atomic crystals allow us many degrees of freedom to probe in their construction. However, over time certain device templates have risen to the top and garnered large amounts of interest due to their manipulable properties and relatively simple construction - one such device is the vertical tunnelling transistor [77]. These use a precise combination of material layering and incident fields in order to construct an electronic device, with rich I-V characteristics and short transit times, that is only a handful of atoms thick. Primarily constructed using monolayer graphene electrodes separated by a hexagonal boron nitride insulating barrier [77, 78, 79, 80], however many variations on the theme that utilise other materials and stacking orders exist [81, 82, 83, 84, 85].

Within this chapter, we model the tunnelling properties of a heterostructure based on these graphene tunnelling devices, comprised of a bilayer graphene electrode and a monolayer graphene electrode, book-ending a hexagonal boron nitride tunnelling barrier. The defining characteristic of the system here is a magnetic field applied perpendicularly to the surfaces that quantises the energy bands of the electrodes, with differing spectra for the two distinct electrode setups. The low energy Landau levels in the bilayer demonstrate an asymmetric valley-layer charge distribution that, when combined with the difference in distance between the two layers and the opposite electrode and thus differences in the tunnelling probability, produces a tunnelling current that is polarised by valley. Alongside this, the general coupling strength between two Landau levels differs between the two valleys. We show how this current is also tunable in magnitude and polarisation via standard tunnelling potentials, the rotational misalignment of the two electrodes and the strength of the magnetic field.

3.2 Device Setup

The schematic of the device setup can be seen in Fig. 3.1, displaying the monolayer and Bernal stacked bilayer electrodes, separated by the hexagonal boron

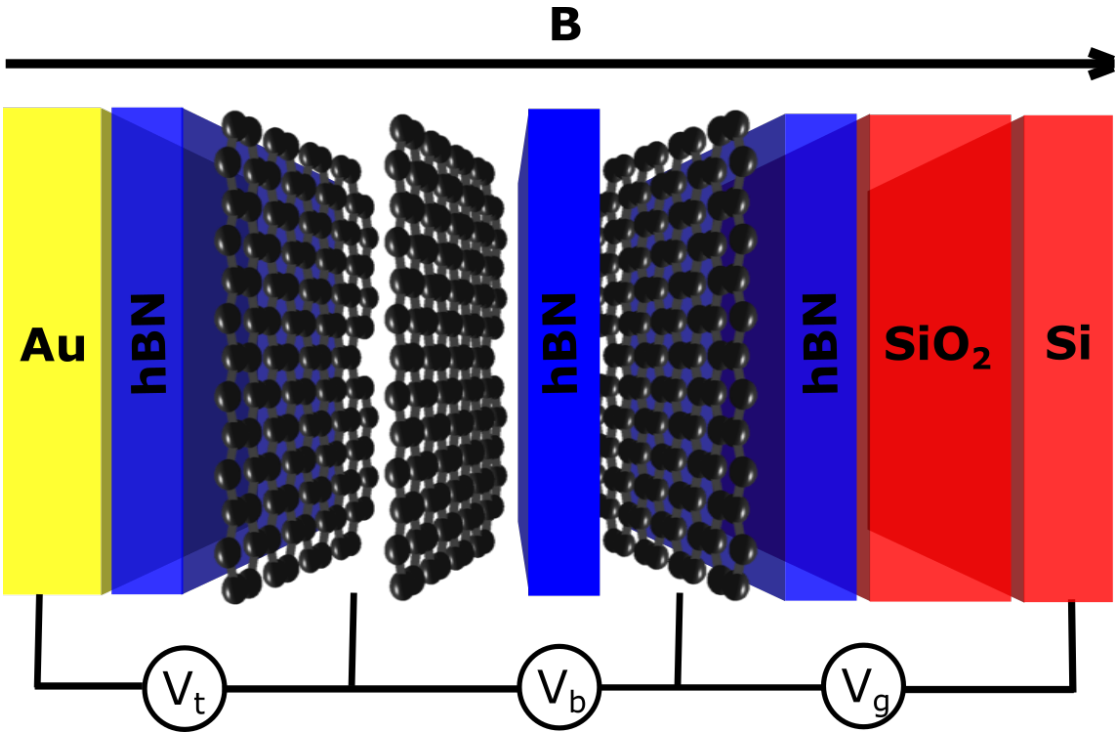

Figure 3.1: Theoretical device setup, showing layering order required to construct the device, presence of tuning potentials $\{V_g, V_b, V_t\}$ and direction of magnetic field incident on the system.

nitride tunnelling barrier. The two graphene electrodes can be rotationally misaligned from one another, with an angle θ separating their crystalline axes. The device is encapsulated by hexagonal boron nitride, to promote and preserve the electronic quality of the graphene systems. The MLG is coupled to a silicon back gate with potential V_g, as is the BLG with a gold top gate and potential V_t. Both of these gates tune the carrier densities of each electrode and thus have a direct impact on the tunnelling current moving through the system. These are utilised in conjunction with a bias voltage V_b placed across the electrodes, that encourages tunnelling through the device. The whole device is placed into a perpendicular magnetic field B, the strength of which we vary between $B = 4\text{T}$ and $B = 1\text{T}$.

A similar device setup has been suggested to induce a valley polarisation within the tunnelling current between graphene electrodes, however it instead utilises an in-plane magnetic field and requires much higher field strengths, up to 30T [86]. Other structures require constrictions and restructuring of the graphene sample, using nanoribbons [87, 88, 89] or defects [90], in order to induce the valley polarisation in graphene devices. We utilise the 2D atomic crystal samples as they are isolated or grown for the layering process and use magnetic fields of much smaller magnitudes.

We can relate the applied potential set $\{V_g, V_b, V_t\}$ to a combination of electrode properties: the carrier densities within each electrode $n_{\mathrm{BLG,\,MLG}}$ (and thus the Fermi levels $\mu_{\mathrm{BLG,\,MLG}}$), the potential felt across the bilayer electrode u and the relative shift of the neutrality points of the two electronic spectra Δ. By utilising Gauss' Law we can obtain the relationship between these two combinations of variables and thus represent our results in more experimentally useful manner, constructing electrostatic equations that are adapted from Ref. [91] as

$$\begin{aligned} V_b &= \frac{1}{e}\left[\mu_{\mathrm{BLG}} - \mu_{\mathrm{MLG}} - \Delta\right], \\ V_t &= e(n_{\mathrm{Si}} + n_{\mathrm{BLG}} + n_{\mathrm{MLG}})\frac{d_{\mathrm{hBN}}}{\epsilon_0 \epsilon_{\mathrm{hBN}}}, \\ V_g &= \frac{e n_{\mathrm{Si}}}{\epsilon_0}\left(\frac{d_{\mathrm{SiO_2}}}{\epsilon_{\mathrm{SiO_2}}} + \frac{d_{\mathrm{hBN}}}{\epsilon_{\mathrm{hBN}}}\right), \\ \Delta &= e^2(n_{\mathrm{MLG}} + n_{\mathrm{Si}})\frac{d + d_0}{\epsilon_0 \epsilon_{\mathrm{hBN}}}, \end{aligned} \tag{3.1}$$

within which d_0 gives the distance between the two layers within the bilayer graphene electrode, $d_{\mathrm{SiO_2}}$ is the width of the SiO_2 buffer, d_{hBN} is the width of the encapsulating hBN and finally d is the width of the tunnelling barrier, which we take to be three layers thick. The dielectric constants of the materials are $\epsilon_{\mathrm{hBN}} = 3$ and $\epsilon_{\mathrm{SiO_2}} = 3.9$, respectively [91]. n_{Si} is the carrier density difference provided by the silicon gate and has value

$$n_{\mathrm{Si}} = \frac{\epsilon_0}{e^2 d_0} u - n_{\mathrm{BLG,1}} - n_{\mathrm{MLG}},$$

where $n_{\mathrm{BLG,1}}$ is the carrier density of the individual layer from the bilayer system closest to the Si electrode such that $n_{\mathrm{BLG}} = n_{\mathrm{BLG,1}} + n_{\mathrm{BLG,2}}$.

The tuning potentials have the additional side-effect that they induce an electric field across the bilayer electrode, adjusting the band structure of the electrode. In standard bilayer graphene systems, without the presence of the magnetic field, this separates the conduction and valence bands away from zero energy and induces a tunable band gap that is proportional to the strength of the field. Here, this manifests in lifting the degenerate Landau levels at the neutrality point and is proportional to the carrier density pushed into the system via the potential set

$$u = \frac{e^2 d_0}{\epsilon_0}\left(n_{\mathrm{Si}} + \frac{1}{2} n_{\mathrm{BLG}} + n_{\mathrm{MLG}}\right). \tag{3.2}$$

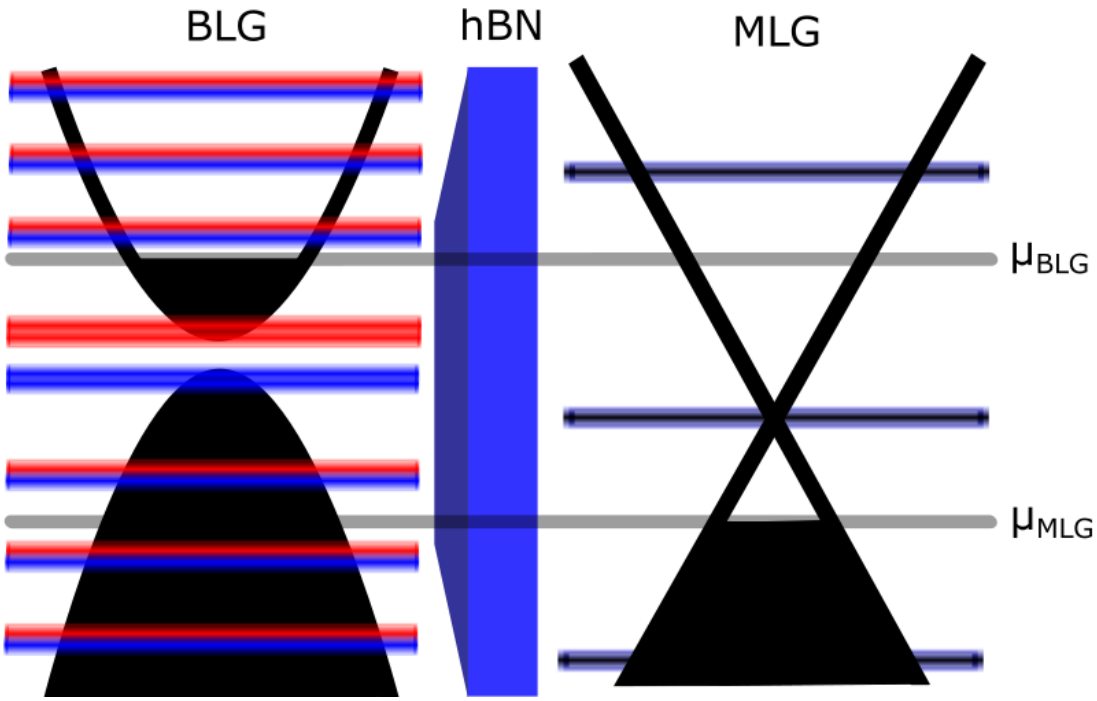

Figure 3.2: Energy band diagram of device. The magnetic field quantises the energy bands present with a separation proportional to the strength of the field, however the energy level distribution between the two electrodes varies due to the difference in electrode composition. Within the bilayer graphene, the degeneracy of the two valleys is lifted via the presence of an external potential u across the layers, and these are indicated by the red and blue levels that shifted away from one another.

The exact effects of this variable on the Landau level spectrum of the bilayer electrode are discussed in more detail within the next section.

3.3 Electronic Structure in a Perpendicular Magnetic Field

3.3.1 Monolayer

We define the structure of the electrodes as constructs of simple graphene sheets, but with the added caveat that they are in the presence of a magnetic field perpendicular to their layers. Electrons in a two-dimensional gas, in the presence of such a field, follow cyclotron orbits and display a band structure that is quantised into Landau levels. This manifests in a transformation of the electron momentum under a Landau gauge such that $\boldsymbol{p} \to \boldsymbol{p} + e\boldsymbol{A}$, where $\boldsymbol{A} = (0, -Bx, 0)$, such that the MLG Hamiltonian in the vicinity of the $\boldsymbol{K}_\xi$ valley corner is

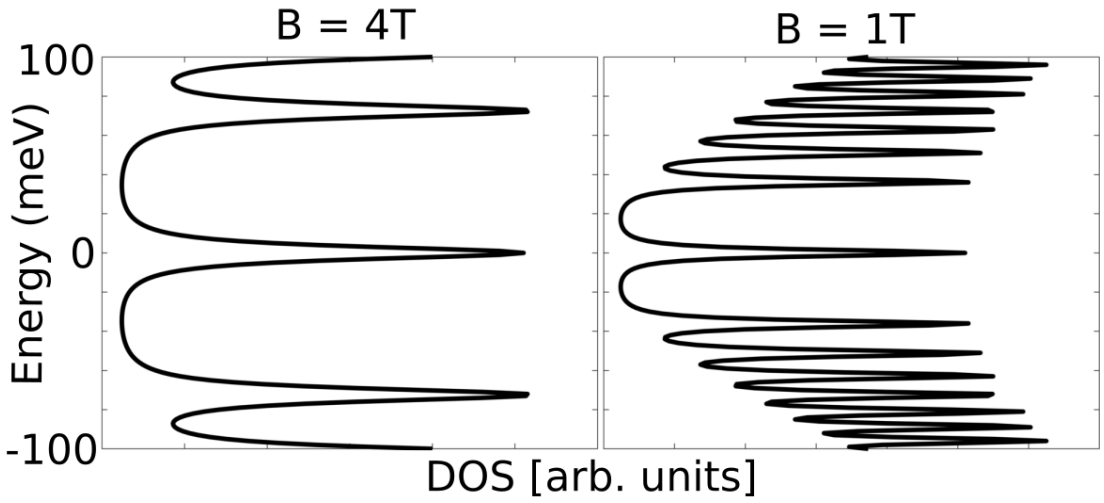

Figure 3.3: Density of states of the MLG electrode for $B = 4$T (left) and $B = 1$T (right), each energy band is defined positionally by Eq. (3.5) and given a Lorentzian broadening, as in Eq. (3.6). The energy spectrum shrinks in spacing as the magnetic field strength decreases and overlaps between neighbouring levels becomes more common.

$$\hat{\boldsymbol{H}}_{\mathrm{MLG}} = \xi v \begin{pmatrix} 0 & \pi^{\dagger} e^{-i\theta} \\ \pi e^{i\theta} & 0 \end{pmatrix} = \xi v \begin{pmatrix} 0 & (p_x - i(p_y - eBx))e^{-i\theta} \\ (p_x + i(p_y - eBx))e^{i\theta} & 0 \end{pmatrix}.$$

Acting in a sublattice $(A, B)^T$ basis in $\boldsymbol{K}_+$ and $(B, -A)^T$ in $\boldsymbol{K}_-$. We account for the possibility of the two electrodes being rotationally misaligned with respect to one another by θ, resulting in a rotation of the momentum space. This produces wave functions [82]

$$\psi_{\boldsymbol{K}_+,n} = \frac{1}{\sqrt{2}} \begin{pmatrix} \phi_{|n|} \\ -sie^{i\theta}\phi_{|n|-1} \end{pmatrix} e^{i\boldsymbol{k}_y \cdot \boldsymbol{y}}, \quad \psi_{\boldsymbol{K}_-,n} = \frac{1}{\sqrt{2}} \begin{pmatrix} sie^{i\theta}\phi_{|n|-1} \\ \phi_{|n|} \end{pmatrix} e^{i\boldsymbol{k}_y \cdot \boldsymbol{y}}, \tag{3.3}$$

$$\phi_n = \frac{1}{\sqrt{2^{|n|}|n|!\sqrt{\pi}\lambda_B L}} \exp\left[-\frac{1}{2\lambda_B^2}(x - X_{\mathrm{MLG}})^2\right] \mathcal{H}_n\left(\frac{1}{\lambda_B}(x - X_{\mathrm{MLG}})\right). \tag{3.4}$$

Within this, integer n defines the Landau level number and holds for $|n| \neq 0$, the magnetic length is given by $\lambda_B = \sqrt{\hbar/eB}$, L the characteristic length in the y direction, the orbit centres as $X_{\mathrm{MLG}} = \lambda_B^2 k_y$, $\mathcal{H}_n$ is an nth order Hermite polynomial and the conduction and valence band are distinguished by band index $s = \pm 1$. These solutions have a form that contain planes waves in the y-direction and simple harmonic oscillator waves in the x-direction, quantised by the Landau level number n. The energy spectrum is then described by

$$E_n = s\frac{\sqrt{2}v\hbar}{\lambda_B}\sqrt{|n|}. \tag{3.5}$$

The distribution of levels can be seen more clearly in the density of states of the electrode in Fig. 3.3, in which the spacing between Landau levels decreases with increasing index, hence the energy being proportional to the $\sqrt{|n|}$ term. We model the density of states of both electrodes using Lorentz functions, in order to give broadening to the confined energy levels, due to electron-electron interactions [82]. This has form

$$D_{\text{MLG, BLG}}(E, E_{n,l}) = \sum_{n,l}\frac{1}{\pi}\frac{\Gamma}{(E - E_{n,l})^2 + \Gamma^2}. \tag{3.6}$$

Γ defines the broadening and has values of 2meV and 4meV for $B = 1$T and $B = 4$T respectively [82], identically for both electrodes, to correspond to experimental data.

At the neutrality point, such that $n = 0$, we find that our electron density is sublattice-valley polarised

$$\psi_{\boldsymbol{K}_+,0} = \begin{pmatrix}\phi_{|0|}\\ 0\end{pmatrix}e^{i\boldsymbol{k}_y\cdot\boldsymbol{y}}, \quad \psi_{\boldsymbol{K}_-,0} = \begin{pmatrix}0\\ \phi_{|0|}\end{pmatrix}e^{i\boldsymbol{k}_y\cdot\boldsymbol{y}}.$$

3.3.2 Bilayer

For the bilayer electrode opposite, we use the two-band Hamiltonian as written in Eq. (1.24), in order to describe purely the low-energy band structure of the electrode [17, 32]

$$\hat{\boldsymbol{H}}_{\text{BLG}} = -\frac{1}{2m}\begin{pmatrix}0 & \pi^{\dagger 2}\\ \pi^2 & 0\end{pmatrix} + \frac{\xi u}{2}\begin{pmatrix}1 & 0\\ 0 & -1\end{pmatrix} - \frac{\xi u v^2}{\gamma_1^2}\begin{pmatrix}\pi^\dagger\pi & 0\\ 0 & -\pi\pi^\dagger\end{pmatrix},$$

in a basis of non-dimer states $\{\phi_{A1}, \phi_{B2}\}^T$ in $\boldsymbol{K}_+$ and $\{\phi_{B2}, \phi_{A1}\}^T$ in $\boldsymbol{K}_-$, with interlayer coupling $\gamma_1 \approx 0.38$eV and an external potential across the sheets, tunable in proportion to the device potentials, u. The justification for this is that the effect we seek manifests most obviously when the energy levels are clearly distinct from one another and therefore at higher energies, where the energy spectrum is more

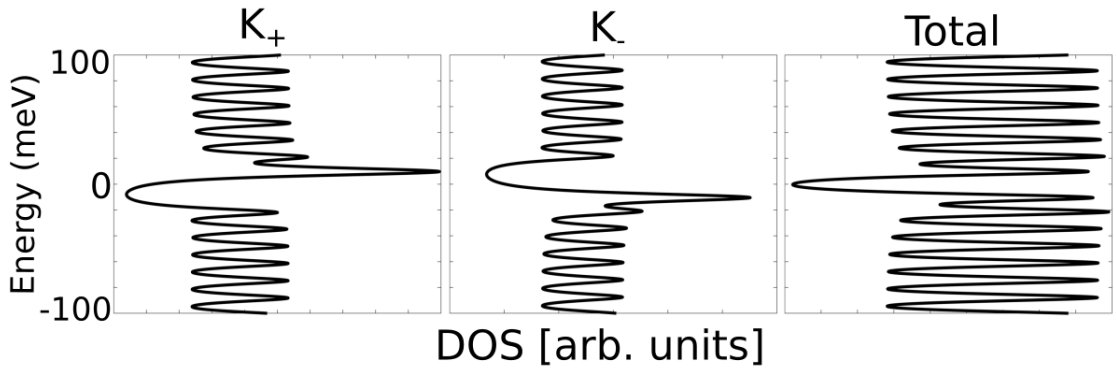

Figure 3.4: Density of states of the BLG electrode for the K_+ valley (left), the K_- valley (middle) and in total (right), each energy band is defined positionally by Eq. (3.9) due to the presence of an external potential of 20 meV.

densely populated due to the overlap with high order bands, we can expect it to be more subdued.

As previously mentioned, we allow for our electrodes to be rotationally misaligned from one another. This rotational misalignment re-positions the BLG valleys by $\Delta \boldsymbol{K}_\pm = (\hat{\boldsymbol{R}}_\theta - 1)\boldsymbol{K}_\pm$, via the anti-clockwise rotation matrix $\hat{\boldsymbol{R}}_\theta$, and thus the wave functions have form [17]

$$\psi_{\boldsymbol{K}_\pm,l} = \frac{1}{\sqrt{2C}} \begin{pmatrix} |E_l|\phi_{|l|} \\ (E_l - \xi\frac{u}{2} + \xi u|l|x^2)\phi_{|l|-2} \end{pmatrix} e^{i\boldsymbol{k}_y \cdot \boldsymbol{y}}, \tag{3.7}$$

$$\phi_l = \frac{1}{\sqrt{2^{|l|}|l|!\sqrt{\pi}\lambda_B L}} \exp\left[-\frac{1}{2\lambda_B^2}(x - X_{\mathrm{BLG}})^2 - i\Delta K_x(x - X_{\mathrm{BLG}})\right] \mathcal{H}_l\left(\frac{1}{\lambda_B}(x - X_{\mathrm{BLG}})\right),$$

where the centre of the orbits is shifted by the rotation to $X_{BLG} = \lambda_B^2(k_y + \Delta K_{\pm,y})$ and with discretised energy levels, that are lifted in valley degeneracy by the presence of the external potential u. This can be seen most obviously in the density of states of the electrode for each valley, as in Fig. 3.4 in which the $l = 0$ and $l = 1$ levels are shifted away from the neutrality point by an external potential of 20meV.

Without an external field present, $u = 0$, the LLs are distributed as such

$$E_l(u = 0) = s' \frac{\hbar^2}{m\lambda_B^2}\sqrt{|l|(|l| - 1)}, \tag{3.8}$$

with $m = \gamma/2v^2$. The spectra is roughly equidistant in separation for level indexes larger than 2, due to the dependence on the $\sqrt{|l|(|l| - 1)}$ term.

Alternatively, under the influence of an external potential, the LLs can be

thought of as a perturbed version of the original spectrum, with energy values that depend on the unperturbed values above. As such, the LL in Fig. 3.4 are centred around energies of value

$$\begin{aligned} E_l &= -\frac{x^2\xi u}{2} + s'\sqrt{E_l^2(u=0) + \frac{1}{4}u^2}, \quad l \geqslant 2, \quad x = \frac{\sqrt{2}v\hbar}{\lambda_B\gamma_1}, \\ E_1 &= \frac{\xi u}{2} - x^2 u, \\ E_0 &= \frac{\xi u}{2}, \end{aligned} \tag{3.9}$$

Unlike the MLG electrode, two-fold degenerate through-out due to the presence of an identical solution for either valley, the BLG valley is four-fold degenerate at the neutrality point (if we take $u = 0$) [22, 92, 93]. Both the $l = 0$ and $l = 1$ solutions reduce to zero energy within the $\sqrt{|l|(|l|-1)}$ dependence. This low-energy case, rearranged to the same $\{\phi_{A1}, \phi_{B2}\}^T$ basis, simply for visual clarity, present wave functions of the form [32]

$$\begin{aligned} \psi_{\boldsymbol{K}_+,1} &= \begin{pmatrix} \phi_1 \\ 0 \end{pmatrix} e^{i\boldsymbol{k}_y\cdot\boldsymbol{y}}, \quad \psi_{\boldsymbol{K}_-,1} = \begin{pmatrix} 0 \\ \phi_1 \end{pmatrix} e^{i\boldsymbol{k}_y\cdot\boldsymbol{y}}, \\ \psi_{\boldsymbol{K}_+,0} &= \begin{pmatrix} \phi_0 \\ 0 \end{pmatrix} e^{i\boldsymbol{k}_y\cdot\boldsymbol{y}}, \quad \psi_{\boldsymbol{K}_-,0} = \begin{pmatrix} 0 \\ \phi_0 \end{pmatrix} e^{i\boldsymbol{k}_y\cdot\boldsymbol{y}}. \end{aligned} \tag{3.10}$$

The electron distributions, in a layer separated basis, suggest that for the low-energy case the electrons are distributed such that the first layer contains only electrons from the $\boldsymbol{K}_+$ valley whilst the second contains electrons from the $\boldsymbol{K}_-$ valley. This disparity of states across the layers is one of the features we exploit within our device in order to induce a tunnelling current that is valley polarised.

3.4 Tunnelling Current

Electrons flow through the device via tunnelling through the hBN barrier located between the graphene electrodes. The direction and magnitude of this current can be tuned externally by the bias and gate voltages, however it is also dependent on the coupling between the initial and final states of the graphene structures. The matrix element that describes this coupling between two states, as previously determined in Eq. (3.3) and Eq. (3.7), can be found via

$$M^{s,s'}_{n,l,K_\pm} = \int_A \psi^\dagger_{K_\pm,n,s} V_{hBN} \psi_{K_\pm,l,s'} dA.$$

V_{hBN} defines the decay potential through the insulating barrier and allows us to distinguish between the individual layers of the BLG, using $d \approx 6.5$Å as the separation between the electrodes and d_0 as the separation between the individual sheets within the BLG.

$$V_{hBN} = V_0 \exp\left[-\frac{d}{r_1}\right] \begin{pmatrix} 1 & \exp\left[-\frac{d_0}{r_2}\right] \\ 1 & \exp\left[-\frac{d_0}{r_2}\right] \end{pmatrix},$$

where d and d_0 again are the tunnelling barrier length and the separation of layers in bilayer graphene respectively and r_1 and r_2 are the scaling constants that describe the loss of tunnelling probability with increasing distance. We scale our tunnelling probability through the hBN barrier $-d/r_1$ to match them to other models and experimental data sets [77, 79, 86, 94], leading to a 1/25 times reduction of the tunnelling probability per layer tunnelled through [77]. We assume that the effective barrier experienced by the tunnelling electrons remains constant in the energy ranges we probe, due to the large inherent band gap of insulating hexagonal boron nitride [82]. The additional distance d_0 hinders the tunnelling probability of electrons in the furthest layer as graphene, despite its conductive properties, acts as an out-of-plane insulator [95, 96]. Assuming the tunnelling decay through a material is dependent on the band gap of the material, an increasing gap leading to an increasing decay [79], the gapless spectrum of graphene should have a decay constant less than that of boron nitride, however we choose to model the additional graphene sheet as another insulating boron nitride sheet in order to account for the worst tunnelling possibility.

This dependence on the distance from the tunnelling barrier can be seen more explicitly upon expanding the full relationship for the coupling strength between two generic Landau levels

$$
\begin{aligned}
M^{s,s'}_{n,l,K_+} &= \frac{V_0 P_{n,l}}{\sqrt{2}} e^{-\frac{d}{r_1}} \left[\Lambda_1 + e^{-\frac{d_0}{r_2}} \Lambda_2 \right], \\
M^{s,s'}_{n,l,K_-} &= \frac{V_0 P_{n,l}}{\sqrt{2}} e^{-\frac{d}{r_1}} \left[\Lambda_2 + e^{-\frac{d_0}{r_2}} \Lambda_1 \right],
\end{aligned}
\tag{3.11}
$$

where the normalisation constant $P_{n,l} = \sqrt{(1+\delta_{n,0})}$. Within this the overlap integrals are grouped as such

$$
\begin{aligned}
\Lambda_1 &= C_1 \Lambda(|n|,|l|) - \xi s i C_1 \Lambda(|n|-1,|l|) e^{i\xi\theta}, \\
\Lambda_2 &= C_2 \Lambda(|n|,|l|-2) - \xi s i C_2 \Lambda(|n|-1,|l|-2) e^{i\xi\theta}, \\
C_1 &= \frac{|E_l|}{\sqrt{C}}, \quad C_2 = \frac{(E_l - \xi\frac{u}{2} + \xi u |l| x^2)}{\sqrt{C}},
\end{aligned}
\tag{3.12}
$$

For a set index combination, the difference in coupling strength between the two valleys manifest in how the two coupling components, Λ_1 and Λ_2, swap places in the equation and interact with the extra decay provided by the exponential term $\exp[-d_0/r_2]$. Within these, the generic overlap integral itself is given by

$$
\begin{aligned}
\Lambda(|n|,|l|) = \int_A \phi^\dagger_{|n|} \phi_{|l|} dA = \frac{2\pi 2^{\max\{n,l\}} (\min\{n,l\})!}{\sqrt{2^{|n|}|n|!}\sqrt{2^{|l|}|l|!}} e^{i\frac{1}{2}\Delta K_x \Delta K_y \lambda_B^2} \\
\cdot \left(\mathrm{sign}(n-l)\frac{1}{2}\lambda_B \Delta K_y - i\frac{1}{2}\lambda_B \Delta K_x \right)^{|n-l|} e^{-\frac{\boldsymbol{\Delta K}^2 \lambda_B^2}{4}} \mathcal{L}^{|n-l|}_{\min\{n,l\}} \left(\frac{\boldsymbol{\Delta K}^2 \lambda_B^2}{2} \right).
\end{aligned}
\tag{3.13}
$$

For which we make use of the known integral solution of the form [97]

$$
\int e^{-x^2} \mathcal{H}_n(x+y) \mathcal{H}_m(x+z) = \sqrt{\pi} 2^n m! y^{n-m} \mathcal{L}^{n-m}_m(-2yz), \quad n \geqslant m.
$$

In Eq. (3.13), we can note that when $\theta = 0°$ the two valley positions overlap and $\boldsymbol{\Delta K} = 0$, recasting the general coupling to

$$
\Lambda(|n|,|l|) = \int_A \phi^\dagger_{|n|} \phi_{|l|} dA = \frac{2\pi 2^{\max\{n,l\}} (\min\{n,l\})!}{\sqrt{2^{|n|}|n|!}\sqrt{2^{|l|}|l|!}} \delta_{|n|,|l|},
\tag{3.14}
$$

it is via this relation that the strict conservation of angular momentum through

the tunnelling barrier is encoded in non-rotated systems. Only one Λ component across both Λ_1 and Λ_2 can be non-zero at any combination of Landau level indices and, even then, certain combinations are preferred by certain valleys - this is another large source of valley polarisation for our tunnelling current.

Alternatively, with a rotation between our two electrodes, the valleys misalign vertically such that $\boldsymbol{\Delta K} \neq 0$ and all combinations of Landau levels indices are allowed, with a strength that is dependent not only on the rotation, but also on the Landau level index of both electrodes. These couplings can be seen across many index combinations in Fig. 3.5, for a magnetic field of 4T and a rotation of 0.25° and 0.5° - highlighting the preference for particular couplings at low energy and index combinations with a roughly similar separation. This 'rippled' effect is a consequence of the interaction of the level indexes with the generalised Laguerre polynomial term, as it has the form

$$\mathcal{L}^{|n-l|}_{\min(n,l)}\left(\frac{\boldsymbol{\Delta K}^2\lambda_B^2}{2}\right) = \sum_{i=0}^{n}(-1)^i \begin{pmatrix} \min(n,l)+|n-l| \\ \min(n,l)-i \end{pmatrix} \frac{1}{i!}\left(\frac{\boldsymbol{\Delta K}^2\lambda_B^2}{2}\right)^i. \quad (3.15)$$

These index preferences morph under a change in rotation angle or field strength and therefore the point around which we expand our polynomial. To a certain degree, these variables can be thought of as 'highlighting' or 'favouring' particular combinations of Landau level indices.

With these two polarisation effects in mind, we seek to model the current flow via Fermi's Golden rule. It is dependent on the occupation of the initial and final states and the coupling between those two, and is given by the sum over all states in the two electrodes

$$\begin{aligned} I_\pm &= \frac{2g_s\pi e}{\hbar}\sum_{n,l}\sum_{s,s'}\sum_{k_1,k_2}|M^{s,s'}_{n,l,K_\pm}|^2[f_{\mathrm{BLG}}(E_{\mathrm{BLG}}) - f_{\mathrm{MLG}}(E_{\mathrm{MLG}})]\delta(E_{\mathrm{BLG}} - E_{\mathrm{MLG}}), \\ &= \frac{2g_s\pi e}{\hbar}\int\sum_{n,l}|M^{s,s'}_{n,l,K_\pm}|^2 D_{\mathrm{BLG}}(E_{\mathrm{BLG}})D_{\mathrm{MLG}}(E_{\mathrm{MLG}} - \Delta)dE_{BLG}, \end{aligned} \quad (3.16)$$

in which $g_s = 2$ to account for the spin degeneracy. The Fermi functions $f_{BLG,MLG}$ define the distribution of the electrons around the Fermi level, in which we assume a low-temperature limit and thus a distinct cut-off, and $D_{\mathrm{BLG,\,MLG}}$ represents the density of states of the two electrodes, one of which is shifted by Δ to account for the spectral energy shift induced by the external potentials.

Upon obtaining the magnitude of the current per valley, we can then calculate

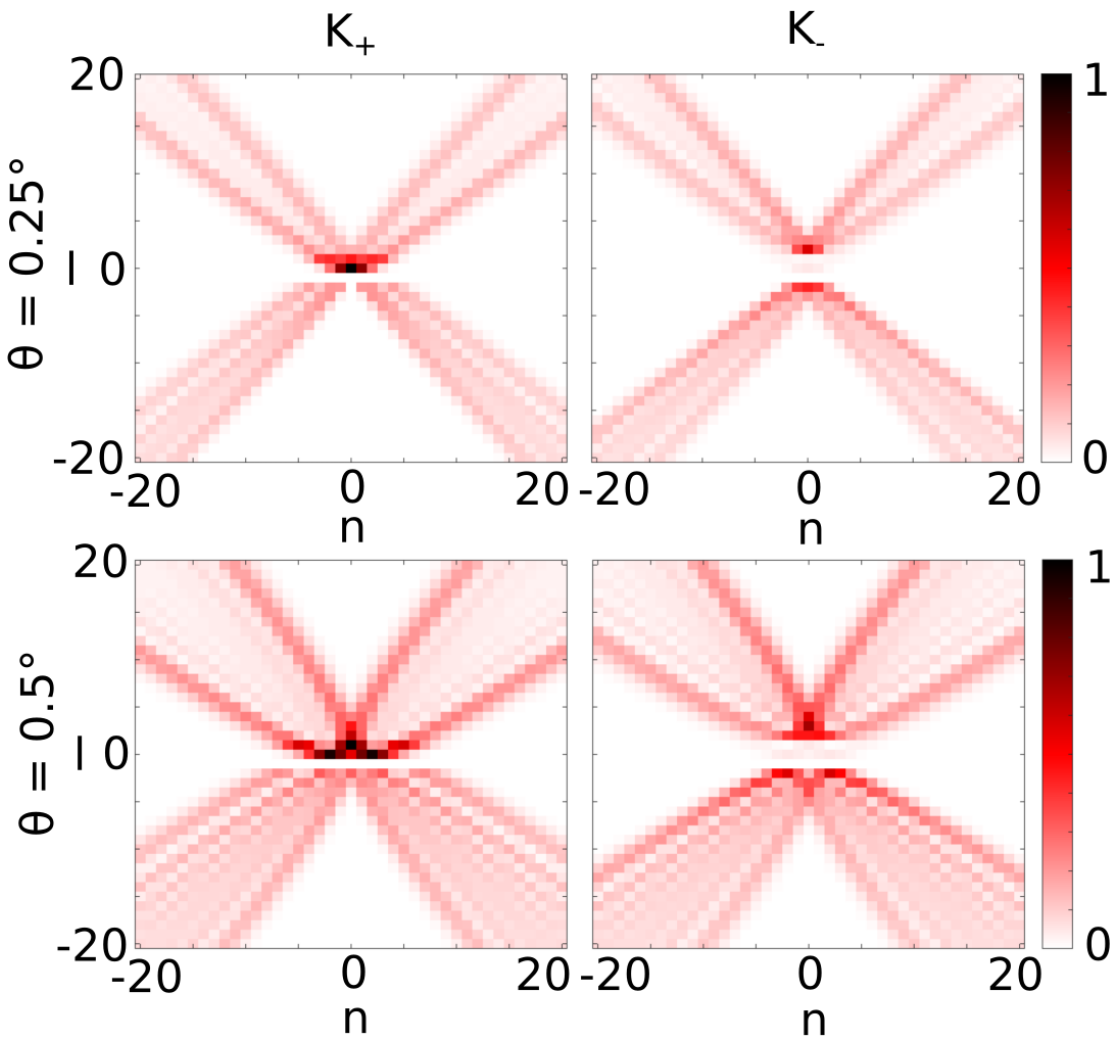

Figure 3.5: Coupling strength $|M^{s,s'}_{n,l,K_\pm}|$ for various combinations of Landau level indices l and n, referring to the bilayer and monolayer electrode setup respectively. Solutions are scaled between 0 and 1 for each angle, for $B = 4$T and $\theta = 0.25°$ (above) and $\theta = 0.5°$ (below) and for the K_+ (left) and K_- (right) valley. This displays both the difference in coupling strengths in a changing rotation, but additionally the strength disparity between the two valleys.

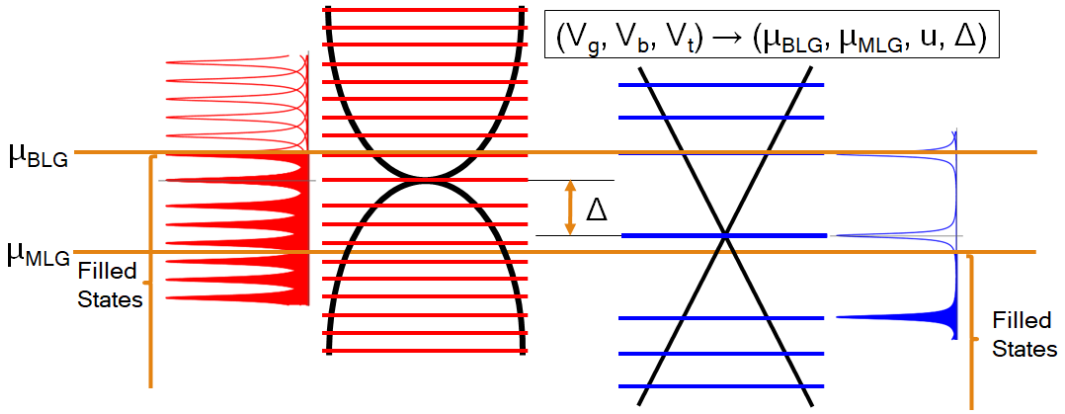

Figure 3.6: The calculation procedure involves finding the variable set $\{\mu_{\mathrm{BLG}}, \mu_{\mathrm{MLG}}, u\}$ that best describes the effects of an applied potential set $\{V_g, V_b, V_t\}$. A generic example, showing the Landau levels and broadened individual density of states for each level in both electrodes and the overlap of tunnelling states, defined by the Fermi levels and spectra shift. The vertical shift of the spectra with respect to one another, Δ, is an important by-product of this calculation that helps to define the overlap of energy bands.

a value for the polarisation of the tunnelling current using

$$P = \frac{I_+ - I_-}{I_+ + I_-}. \tag{3.17}$$

This ranges between 1 and -1, where a positive polarisation favours current flow from the $\boldsymbol{K}_+$ valley and a negative polarisation favours the $\boldsymbol{K}_-$ valley.

3.5 Description of Matlab Procedure for Current Calculation

Our tunnelling system comprises of two electrodes, each with a distinct Landau level spectrum, and an induced current flow between them due to the presence of a set of tuning potentials $\{V_g, V_b, V_t\}$, laid out as defined in Fig. 3.1. Typically, devices such as these are discussed using an I-V plot with the tuning potentials as the plot axes and a current magnitude at each point. However, due to the form of Eq. (3.16), which depends primarily on the variable set $\{\mu_{\mathrm{BLG}}, \mu_{\mathrm{MLG}}, u\}$, it is simpler to calculate the current whilst varying these values. Thus, we begin by constructing a large database of values that map together the two data sets, $\{\mu_{\mathrm{BLG}}, \mu_{\mathrm{MLG}}, u\} \rightarrow \{V_g, V_b, V_t\}$, utilising the relations in Eq. (3.1). We discretise our energy scale, typically on the order of 1meV, and position the Fermi levels of our two electrodes at all combinations of all possible values, calculating the corresponding potential set produced and storing it.

If we expect the value of Δ to be large, as is the case when the potential set is large in magnitude, we double the separation width of points on the MLG energy scale in order to save on computation time. The carrier density increase in a set energy increase for the monolayer electrode is expected to be roughly half that of the bilayer electrode and therefore the setup should be more sensitive to changes in the Fermi level of the bilayer electrode.

We add a third dimension to our dataset by including the external potential u as an additional degree of freedom, requiring a new calculation of the Landau level spectrum and therefore density of states at each incremental change. This in total produces three large matrices of the three potential values required $\{V_g, V_b, V_t\}$, with dimensions defined by the limits and intervals of the three variable scales, all centred around zero.

This large dataset is then translated to the standard I-V plots, typically used to highlight the properties of similar electronic devices, by defining a potential set $\{V_g, V_b, V_t\}$ and combing the matrix for the set of values closest to it. We then match those to the variable set $\{\mu_{\text{BLG}}, \mu_{\text{MLG}}, u\}$, utilising the fact that they hold the same relative position within their respective matrix. The accuracy of this method is entirely dependent on the amount of data computed in the first step and precise choice of the limits and intervals of each variable, however computation time can quickly scale up due to the three-dimensional nature of the storage. In order to minimise search times, we use the fact that the results should be continuous in order to make the assumption that two adjacent points in potential space should be fairly close to one another within the matrix and, therefore, variable set. At each subsequent point, we choose to scan the immediate vicinity of the previously chosen point and if the percentage mismatch of the potentials chosen lies under some threshold we choose, typically 0.5%, then it is chosen. Otherwise, the entire matrix is searched again, in order to provide the optimal solution at each point in potential space.

For a given point in potential space (V_g, V_b, V_t), we construct a Landau level spectrum, utilising the variable set $(\mu_{\text{BLG}}, \mu_{\text{MLG}}, u)$ in order to define the boundaries of interest. An example of this is shown in Fig. 3.6. The vertical shift between the two energy spectra Δ is assumed to be a by-product of the obtained variable set, that results from the potential set required to reach the carrier densities required, nonetheless it is an important factor to take into account when discerning the window of tunnelling energies and therefore the current. Due to the manner in which we model our broadened Landau levels (seen in Eq. (3.6)), we take care to include in the calculation levels that sit outside of the window of energy provided by the Fermi levels. In regions with a small energy window

of interest or low-current flow, the overlap between the tails of levels outside the energy window can make a significant contribution to the current magnitude and helps to keep the transistion between potential sets continuous. From this we calculate the overlap and coupling strength between every combination of Landau levels of the two electrodes, using the relations in Eq. (3.11) and Eq. (3.13). This is done separately for each valley at each point and the current and polarisation are calculated using Eq. (3.16) and Eq. (3.17).

3.6 Tunnelling Current & Polarisation

Using the procedure described above, we can obtain many datasets that describe the evolution of the current, in both magnitude and polarisation, as a function of the change in the applied potentials. However, for the sake of visual clarity, we focus on a two-dimensional cut-through of potential space, setting $V_t = 0\text{V}$. We still maintain a great deal of control over the I-V characteristics but with the added caveat that they may be further manipulated by the application of some value of V_t and that some regions of potential space may be more accessible by using a three-component voltage set $\{V_g, V_b, V_t\}$ that is on-average lower in magnitude than the required two-component voltage set $\{V_g, V_b\}$.

3.6.1 B = 4T

We begin by using a non-rotated system ($\theta = 0°$) in a magnetic field with strength $B = 4\text{T}$, in order to ensure that the individual Landau levels are well resolved, particularly at low energy. Fig. 3.7 shows the results for such a system, across a large range of potential combinations, reporting the current individually for each valley and the polarisation they produce together. The results are symmetric in magnitude under a transform in potential space of $\{V_g, V_b\} \to \{-V_g, -V_b\}$, due to the electron-hole symmetry of the spectra involved. Additionally marked is the contour of zero value for the variables μ_{BLG}/u in black and μ_{MLG} in green, in order to highlight the positions of the neutrality point and the Landau levels situated around them.

Around the zero point, $V_g = V_b = V_t = 0\text{V}$, small changes in the potential set result in an energy window with Fermi levels close to the neutrality point and $u \approx 0\text{meV}$. This focuses on the overlap and coupling between only levels that exist at the neutrality point, $n = 0$ and $l = 0, 1$, and their interactions. Looking at the index combinations allowed in the non-rotated case of Eq. (3.11), we note that only the $n = 0$ and $l = 0$ levels interact in this window in any meaningful way.

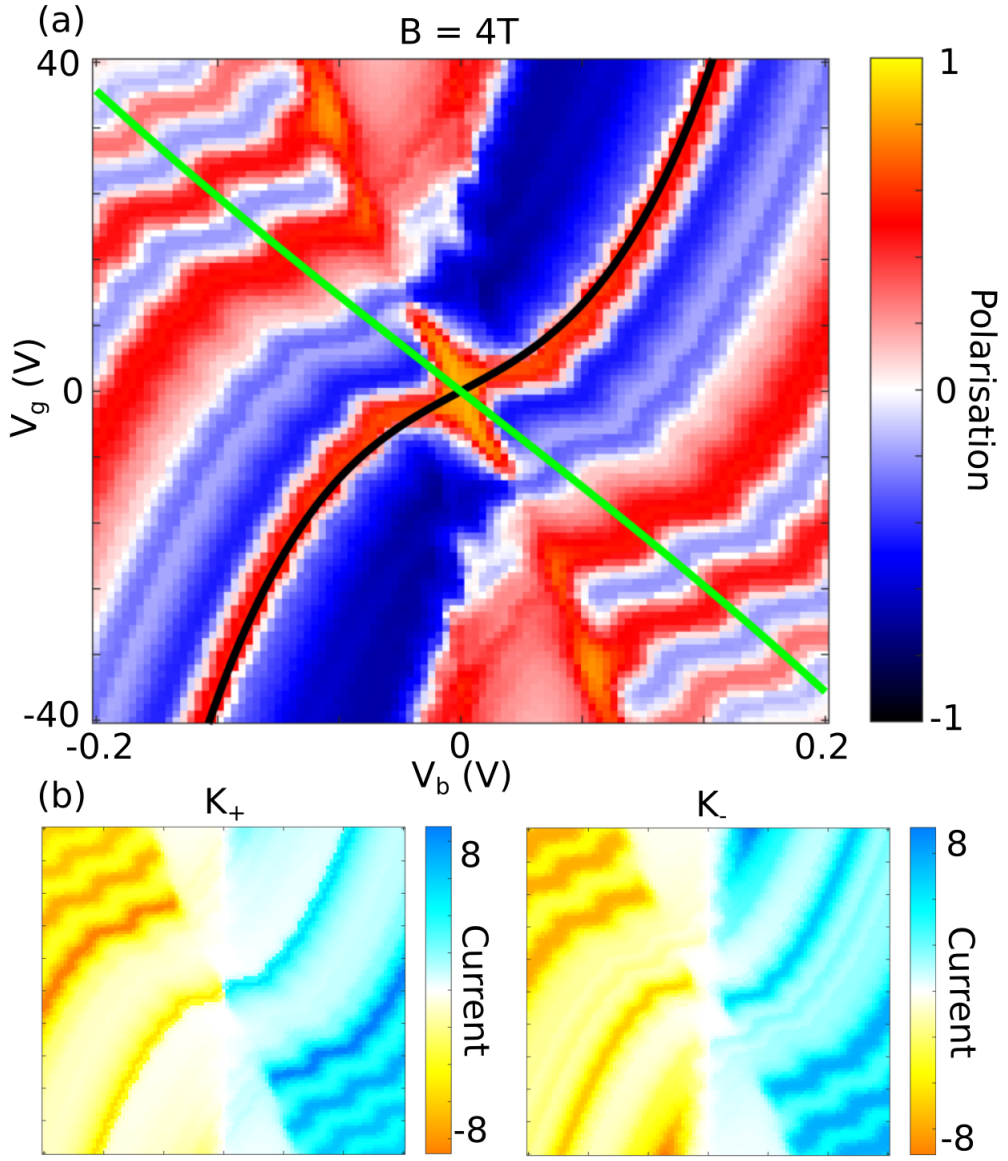

Figure 3.7: (a) Polarisation plot for $B = 4$T and $\theta = 0°$. The polarisation is measured as in Eq. (3.17), so that yellow and red indicates a tunnelling current with a weighting toward the K_+ valley, whilst black and blue are weighted toward the K_- valley. The black and green lines represent the routes of constant value for μ_{BLG}/u and μ_{MLG} respectively. (b) The current plots that construct the polarisation values, with current corresponding the $K_+(K_-)$ valley on the left (right). These use the same axes as the polarisation plot.

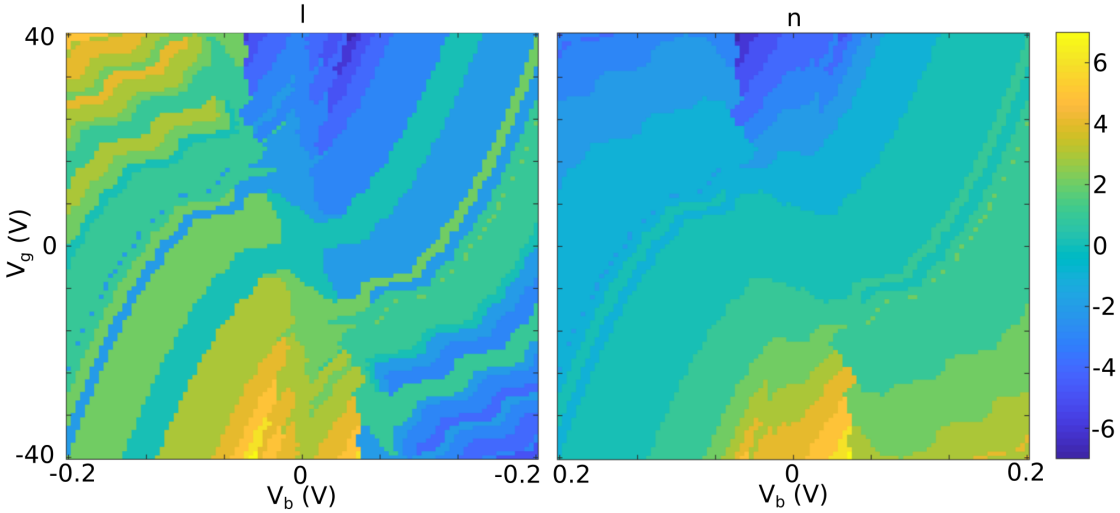

Figure 3.8: The combination of Landau level indexes, bilayer index l (left) and monolayer index n (right), that provide the largest contribution to the current at each point in potential space.

This contributes to both valley currents, however inspection of the matrix element for both displays the reason for the polarisation

$$M^{s,s'}_{0,0,K_+} = \frac{V_0 P_{0,0}}{\sqrt{2}} e^{-\frac{d}{r_1}} \left[C_1 \Lambda(0,0) \right], \quad M^{s,s'}_{0,0,K_-} = \frac{V_0 P_{0,0}}{\sqrt{2}} e^{-\frac{d}{r_1}} \left[e^{-\frac{d_0}{r_2}} C_1 \Lambda(0,0) \right].$$

This interaction can be seen in the current plots within Fig. 3.7, as the low potential region in the K_+ valley contains a substantial current contribution from the layer closest to the tunnelling barrier that fades as the overlap of the two levels misaligns, whilst the K_- valley contribution, existing on the layer furthest from the tunnelling barrier, is negligible - resulting in a maximal polarisation of $\approx 90\%$ in a cross formation that approximately follows the lines of zero Fermi level. There is a shift away from this line as the value of the external potential u (zeroed along the black line) increases due to the displacing of the low-index bilayer Landau levels. This description of the polarisation of the current is equivalent to the layer-valley polarisation argument discussed previously, in relation to the low-energy wave functions of the bilayer electrode in Eq. (3.10).

If we first cut our potential space such that $V_g = 0$V and V_b is free to vary, we note that this K_+ valley preferential current eventually concedes a polarisation of opposite sign. This corresponds to the broadening of the energy window of interest, now including either the $l = 2$ or $l = -2$ level, dependent on the sign of the bias voltage. Increases in the vertical energy shifts misalign the neutrality points of

the electrodes, pushing the $n = 0$ level to interact with the aforementioned bilayer inclusions, eventually overcoming the diminishing response of the $n = l = 0$ overlap and swaying the sign of the polarisation.

Alternatively, cutting such that V_b is small and V_g is variable, the change in sign is also observed. These changes in V_g can somewhat reductively be thought of as increasing or decreasing the overall carrier density of both electrodes, therefore as it increases we elevate the magnitude of both Fermi levels (applying the same sign to both) and thus probe energy states further from the neutrality point in both electrodes. This results in an increasing overlap between the $l = 2$ and $n = 1$ states in the energy window of interest, the begins to supersede the initial coupling.

Further out in potential space, many other features occur that can be directly attributed to the precise combinations of two level indexes. However, due to the decreasing separation between neighbouring levels in the monolayer electrode (as seen from the $\sqrt{|n|}$ term in Eq. (3.5)), these overlaps occur more frequently, with multiple overlaps being important in each window, and they become increasingly more complex to unpack. An overview of this approach to understanding the origin of the polarisation can be seen in Fig. 3.8, which displays the combination of Landau levels that provides the largest contribution to the tunnelling current at each point in potential space. It is worth noting, however, that whilst the largest contributing pair of levels is shown at each point, they alone do not purely dictate the polarisation, as one large contribution can be outweighed by the sum of many more weakly coupled levels, particularly in regions where total current magnitude is low or the levels are tightly packed together.

It is worth noting that while we use these valley-separated results to explain the features of the device, experimentally the total current would instead be measurable - in other words, the sum of the two current plots in Fig. 3.7. Although this would not obscure many of low-energy features due to the well-defined and separated energy bands around the neutrality point, these features become more tightly packed higher in potential space and therefore it would become harder to unpack the various contributions. This could be alleviated through the implementation of a method to measure the valley polarisation directly - however, this is currently beyond the scope of this device and so we focus primarily on attaining valley polarisation magnitudes that are worthwhile investigating.

3.6.2 B = 1T

Although the $B = 4$T situation provides an ideal case for displaying how the polarisation of the tunnelling current can be achieved, due to the well-resolved

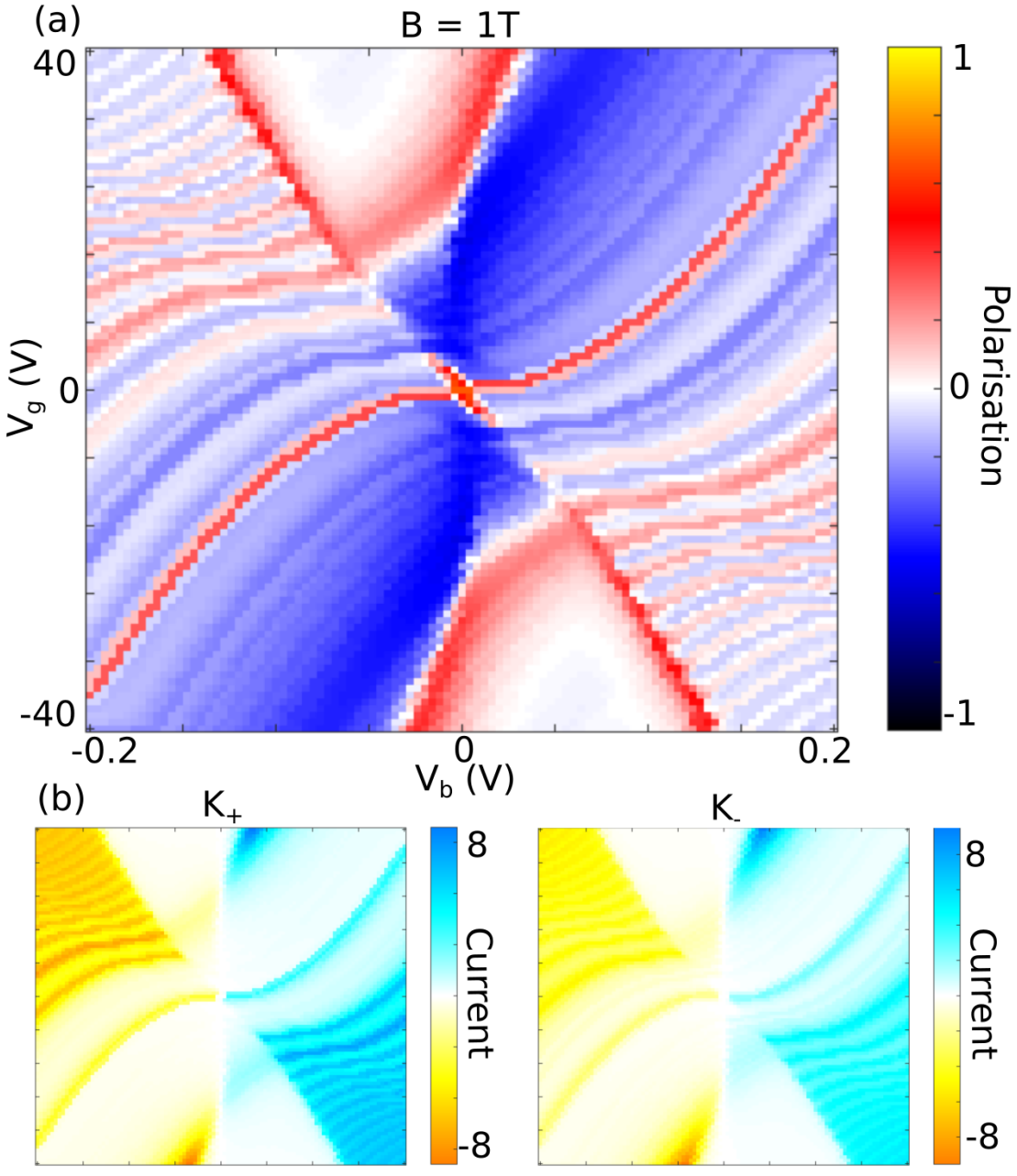

Figure 3.9: (a) Polarisation plot for $B = 1\text{T}$ and $\theta = 0°$. (b) The current plots that construct the polarisation values, with current corresponding the $K_+(K_-)$ valley on the left (right).

separation between neighbouring levels, this field strength is relatively high and may be difficult to achieve experimentally. We then instead consider the case where the magnetic field is reduced to $B = 1\text{T}$. This is of the order of magnitude that could be induced by a neighbouring thin-film magnet [98] built onto the device, rather than relying on the application an external field.

The LL spectrum shrinks and coupling pairs that were previously isolated within an energy window, now compete more strongly with neighbouring overlaps. The scale of reduction can seen in Fig. 3.3 for the monolayer electrode, in which this has a more profound effect due to the decreasing separation between increasing Landau level indices.

Fig. 3.9 shows the polarisation and constituent current plots for the $B = 1\text{T}$ case. Many of the same features appear, such as the central K_+ polarised region, but are reduced in size and magnitude of potentials required, owing to this tighter packing of the Landau level spectra. Ignoring the loss of certain features due to the continuous nature of the polarisation, the $B = 1\text{T}$ landscape can seen as a 'zoomed out' version of the $B = 4\text{T}$ case. Despite these effects, that should overall decrease the chance of a high polarisation value, maximal polarisation still reaches a peak of $\approx 80\%$. Further reducing the magnetic field strength should only continue this pattern - packing the Landau levels tighter together and therefore smoothing out the polarisation landscape.

3.6.3 Rotational Misalignment

As previously discussed, the strict Landau level index matching of the system is lifted when the two electrodes are rotationally misaligned from one another. The coupling strengths, shown in Fig. 3.5, vary with changing index of both electrodes, the rotation angle and the strength of the field applied and, in general, are decreased in comparison to the aligned case.

In order to restrict the number of levels involved in the tunnelling process, we show in Fig. 3.10 the polarisation landscape at $B = 1\text{T}$ for a smaller potential range than the plot shown in Fig. 3.9. Alongside it, we show the same potential range and magnetic field results, but in the presence of rotation angles of $0.25°$ and $0.5°$ between the two electrodes. The current is still polarised, in a similar manner as before, however the individual pairings that dictated the polarisation strength previously are now smeared by the inclusion of many other index coupling pairs. This can be seen in the matrix couplings of Eq. (3.11) - with $\theta = 0°$, only one of the four Λ components can be true in any one index coupling (using the relation seen in Eq. (3.14)), however all four variations of Λ have value in the rotated

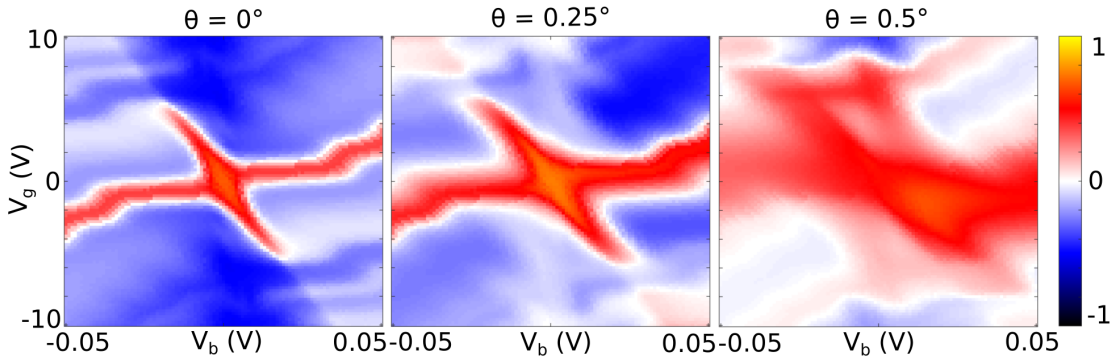

Figure 3.10: Polarisation of the systems in a magnetic field $B = 1$T with increasing angle. The aligned case, $\theta = 0°$, seen on the left, is simply the central region of the plot in Fig. 3.9. When the misalignment is introduced, all LL couplings are allowed with a strength that varies with rotation angle and LL index. The landscape becomes asymmetric and the differing angle favours different combinations of Landau levels, moving the largest asymmetric values in the potential space.

system and as such the current is dependent on all of them.

The polarisation landscape is now also no longer symmetric under a change $\{V_g, V_b\} \rightarrow \{-V_g, -V_b\}$, suggesting our interactions are no longer electron-hole symmetric. Referring back to Fig. 3.5, we note that the couplings themselves vary depending on the signs of both l and n, suggesting the band index can affect the coupling strength in this rotated system. Again, referring back to the coupling between two generic levels, as in Eq. (3.11), we note the explicit dependence on the band index of MLG, s. We can note the additional dependence on the band index of the BLG electrode, but this is hidden with the energy terms of the bilayer Landau levels, as described by Eq. (3.9). Initially, with no rotation and only one allowed component, any dependence on band index is removed by the squaring of the coupling seen in Eq. (3.16).

However, when all components have value, interactions between the various band index dependencies take place, due to the squared term $|M^{s,s'}_{n,l,K_\pm}|^2$ in Eq. (3.16). For the sake of showing this simply, we take the $u = 0$ case and note the explicit dependence of the coupling on both band indices

$$\Lambda_1 = \frac{|E_l|}{\sqrt{C}} \left(\Lambda(|n|, |l|) - \xi s i \Lambda(|n| - 1, |l|) e^{i\xi\theta} \right),$$
$$\Lambda_2 = \frac{|E_l|}{\sqrt{C}} \left(s' \Lambda(|n|, |l| - 2) - \xi s s' i \Lambda(|n| - 1, |l| - 2) e^{i\xi\theta} \right).$$

It is from the interference of these band index terms that the asymmetry arises.

Inspection of Fig. 3.5 also shows how the coupling strength moves with a

change in the rotation angle - this effect manifests in the polarisation asymmetry shifting in potential space with varying angle, in order to match regions where particularly strongly coupled Landau levels overlap. In general, the larger the rotational mismatch, the further out in potential space or the higher in energy the asymmetry is focused.

3.7 Summary

We have modelled the tunnelling current through a vdW heterostructure comprised of a monolayer and bilayer electrode, separated by an insulating hexagonal boron nitride tunnelling barrier, in the presence of a perpendicular magnetic field and explored how the current flow is polarised by valley. This occurs due to a mixture of spatial differences in the occupation of the wave function, as seen in Eq. (3.10) that displays a layer-valley separated electron distribution for low-energy Landau levels. This combines with the corresponding additional decay length added to electrons forced to travel from the furthest layer in the bilayer electrode and the preferencing of individual valleys for particular combinations of Landau levels, both contained within Eq. (3.11), in order to selective tune the polarisation of the tunnelling current, dependent on the potentials imposed upon the device. The polarisation magnitude reaches peaks of $\approx 80 - 90\%$, depending on the system setup, and can be tuned by a variety of factors, including the gate and bias potentials applied to the system, the rotational misalignment between the two electrodes and the strength of the applied magnetic field. In the presence of a rotation of the electrodes, the polarisation landscape becomes asymmetric, a consequence of the distinction between the band indices in the coupling strength.

3.A Inclusion of Top Gate, $V_t \neq 0$V

Initially, we defined our device with two gate voltages, pertaining to either electrode. However, in order to visualise the results clearly we tune the top gate such that $V_t = 0$V. This displays the full range of polarisation and magnitude of current of the device and therefore we include only a brief word on the effects of the inclusion of V_t in order to give a full description of the system. Fig. 3.11 can be compared to Fig. 3.10 in order to see the direct effect that V_t has the landscape.

As the top gate sits adjacent to the bilayer electrode, it has the most direct effect on both the carrier density in the bilayer and the external potential incident across it. The initial adjustment to the carrier density offsets the previously central features and destroys the polarisation symmetry that previously held under a transform of $\{V_b, V_g\} \rightarrow \{-V_b, -V_g\}$. This is due to the non-zero carrier density the system exhibits at the $V_b = V_g = 0$V point, induced by the addition of V_t, and can be seen more obviously in the asymmetry of the current plots.

More prominent however, is the asymmetry provided by the loss and enhancement of certain low-energy features. This is a consequence of the gate voltage introducting an external potential to the bilayer electrode around the $V_b = V_g = 0$V point and therefore splitting the low-energy Landau level spectrum by valley - now the different valley components of the same Landau level are pushed either side of the neutrality point and therefore certain valleys favour certain band index components (or alternatively the sign of V_b). This can be seen more obviously in the current component plots in Fig. 3.11, however it has the knock-on effect of drastically changing the polarisation seen at those points.

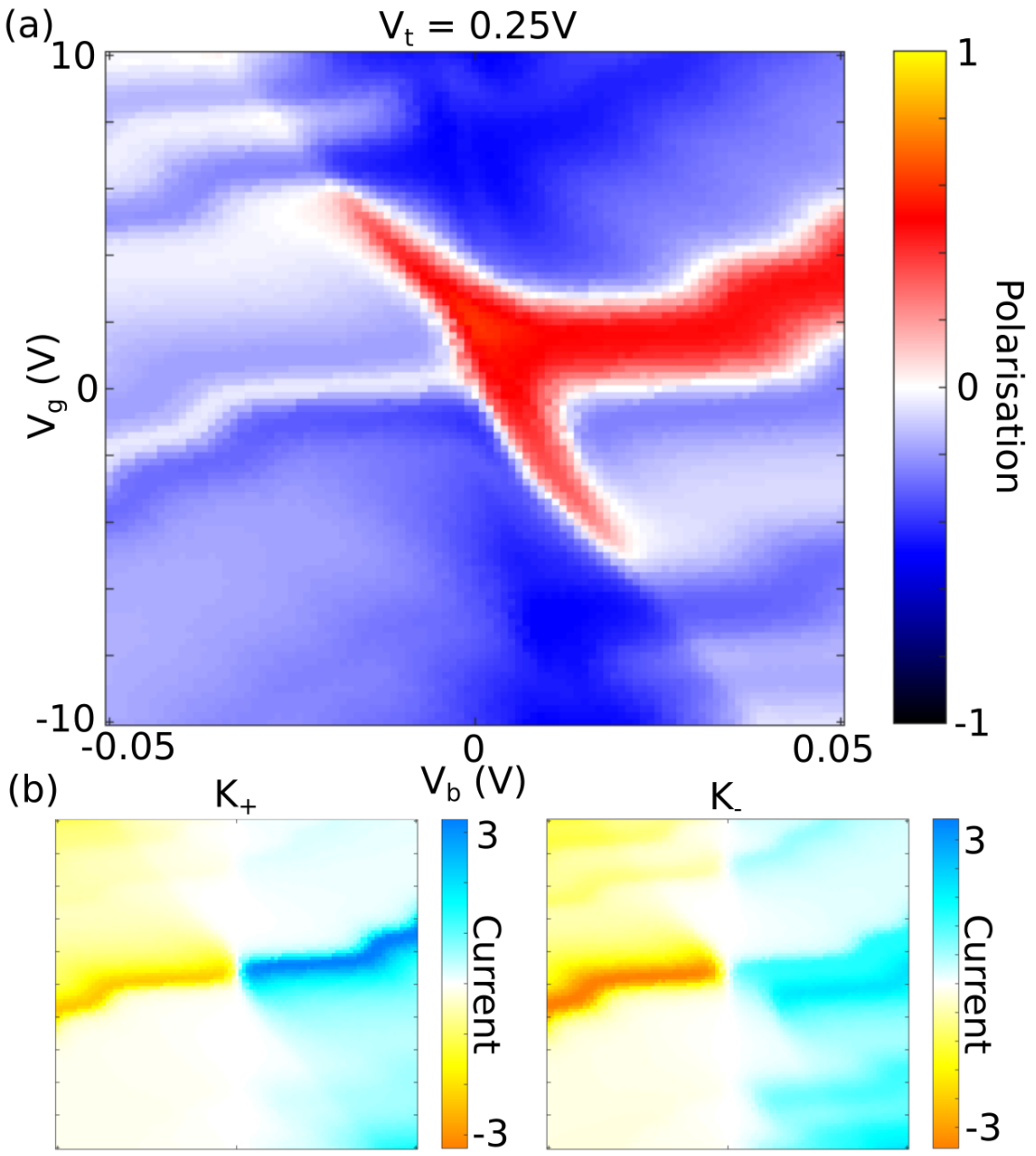

Figure 3.11: (a) Polarisation plot for $B = 1\text{T}$, $\theta = 0°$ and $V_t = 0.25\text{V}$. Note the loss of symmetry of the results in comparison to the unrotated version of Fig. 3.10. (b) The current plots that construct the polarisation values, with current corresponding the $K_+(K_-)$ valley on the left (right).

Chapter 4

Negative differential resistance in van der Waals heterostructures due to moiré-induced van Hove singularities

Portions of this chapter are reproduced from a pre-print article, arXiv:1802.08100.

The work in this chapter was also done in collaboration with J. J. P. Thompson, who again provided the model for the electrostatics and the tunnelling current. These are reproduced here, with permission, in order to provide a complete description of the results.

4.1 Introduction

Chap. 2 highlighted and discussed an example of a simple van der Waals heterostructure that utilises the mismatch in periodicities of two materials. This lead to the creation of a new, larger superlattice periodicity that was used, in conjuction with an external potential, to exploit miniband folding of the perturbed electronic spectra that introduced gaps and flattened mini-bands. Chap. 3 focused on the prospect of a vertical tunnelling device that exploited unique properties of the individual electrodes in order to modify the current flowing through the device. Here, we seek to combine these two approaches to Van der Waals heterostructure construction and create a tunnelling device that uses superlattice reconstruction of the electrodes in order to modify the current flow.

We propose a new variation on the architecture of the vertical tunnelling device, still using the primary components of graphene and hexagonal boron nitride, but instead utilising electrodes that have undergone a reconstruction of their energy bands and density of states due to the presence of a superlattice. We highlight two distinct cases, the first being that of a rotationally aligned combination of monolayer graphene and hexagonal boron nitride [99], the most well known and researched of the bilayer superlattices. The second comprises of a bilayer graphene electrode in which the two graphene sheets are rotationally misaligned, seen, for instance, in bilayer graphene grown on SiC substrates [100]. In both cases, the electronic spectra is recast and a flattening and splitting of energy band features lead to distinct peaks and troughs within the density of states.

Negative differential resistance (NDR), in which an increase in voltage within a device leads to a decrease in the output current, has been identified as a desirable component of these nano-scale components due to its prevalence within semiconductor physics, in which the non-linear response allows for the design of more complex devices with tailored and specific responses. In the Esaki diode [101], for instance, this effect arises due to voltage increases that modify the alignment of occupied and empty electronic states in the source and drain electrodes.

This effect has been observed in a Van der Waals heterostructure as a result of momentum-conserving electron tunnelling through an atomically thin barrier [80, 81, 83, 84, 86, 102]. Due to the high quality of the crystals produced by mechanical exfoliation and the atomically sharp interfaces in the assembled vdW-coupled stack [103], the requirement to match both energy and momentum of the initial and final states leads to a peak in the tunnelling current as applied voltages tune the source and drain to a particular band alignment. However, exfoliation, whilst providing state-of-the-art materials and devices, is currently not a scalable fabrication method.

Materials produced by other methods such as chemical vapour deposition do not achieve the quality necessary to observe momentum-conserving tunnelling and, as such, NDR [94, 104]. Additionally, the many stages deposition and annealing in device construction result in a notable increase of disorder within samples, manifesting in a increase in the disorder (D) peak in the Raman spectra of a graphene electrode [94]. Our device, in which the electrode band structure is altered by the presence of a moiré pattern, does not require strict momentum-conserving tunnelling events, relying purely on the density of states of either electrode, and therefore can be constructed from samples of a lower quality. We examine two of the simplest cases, however the result relies purely on the peaks and troughs provided by the superlattice reconstruction and should therefore be applicable to many other superlattice constructs.

4.2 Generic Device Model

4.2.1 Device Schematic

The theoretical device schematic for both of our vdW tunnelling transistors are shown in Fig. 4.1. As in the prior chapter, it comprises of two graphene-based electrodes separated by an insulating tunnelling barrier of hexagonal boron nitride. A bias voltage V_b is applied between the electrodes whilst a gate voltage V_g is applied beneath the drain electrode. Importantly, the source electrodes is comprised of two layers, arranged in such a manner that Layer 1, furthest from the barrier, generates a long-wavelength periodic potential for electrons in Layer 2, perturbing the electronic states. In structures involving two-dimensional atomic crystals, such periodic potentials arise naturally as a consequence of different lattice constants of the neighbouring materials as well as any misalignment between their respective crystallographic axes, leading to the formation of superlattices that are visually represented by moiré patterns and seen, for example, in scanning

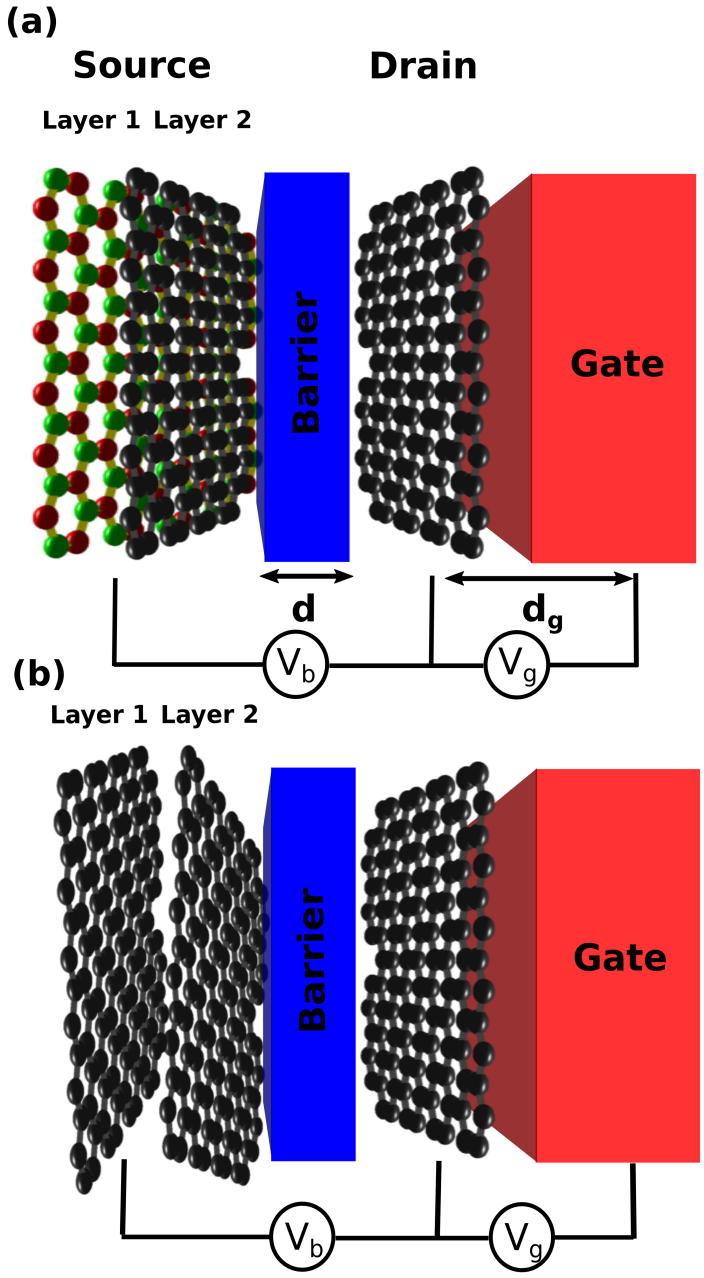

Figure 4.1: (a) Device schematic for a tunnelling device with a source electrode comprised of a highly-aligned graphene/hBN heterostructure. Also shown are the inherent distances d and d_g, as well as contacts for the bias and gate voltages V_b and V_g. (b) Alternative schematic in which the source electrode is replaced with a twisted bilayer graphene construct. Partially reproduced from arXiv:1802.08100.

tunnelling microscopy measurements [99, 105, 106, 107, 108].

The exact impact of the moiré perturbation depends on both the atomic composition of the two layers and details of the two interacting geometries. But in general, the additional potential felt by the graphene leads to Bragg scattering of the electrons and folding of the electronic spectrum into the superlattice Brillouin zone (sBZ), typically accompanied by flattening of bands and the opening of minigaps along the zone boundary [42, 99, 105, 106, 107, 108, 109, 110, 111, 112, 113]. As a result of such a spectral reconstruction, the electronic density of states (DOS) is strongly modified. A fact crucial to the functioning of our device as, for a thin tunnelling barrier, the current I is sensitive to the source and drain DOS, D_s and D_d.

4.2.2 Tunnelling Current & Electrostatics

This current is modelled as before via Fermi's Golden Rule, utilising purely energy conservation and thus managing magnitude purely through matching of these DOS,

$$I = \frac{2g_s\pi e}{\hbar}\int T_\epsilon D_s(\epsilon)D_d(\epsilon-\Delta)\cdot[f(\epsilon-\mu_s)-f(\epsilon-\Delta-\mu_d)]\,d\epsilon, \tag{4.1}$$

where the energy ϵ is measured from the source electrode neutrality point, Δ is the vertical shift between the two neutrality points of the electrodes, T_ϵ is the transmission coefficient, μ_s and μ_d are the Fermi levels in the source and drain respectively and g_s takes into account additional degeneracies of spin and valley of the electronic states.

We relate the applied potential values V_b and V_g to the energy variable set to the energy values μ_s, μ_d and u, via

$$\begin{gathered} V_b = \frac{1}{e}(\mu_s - \mu_d - \Delta), \quad V_g = \frac{ed_g}{\epsilon_0\epsilon}n_g, \\ \Delta = \frac{e^2 d}{\epsilon_0}(n_B(\mu_d)+n_g), \end{gathered} \tag{4.2}$$

where d and d_g are the thickness of the tunnelling barrier and the distance between the drain and the back gate, as seen in Fig. 4.1, $\tilde{\varepsilon}$ and ε are the relative permittivities of the barrier and the substrate between the drain and gate, and $n(\mu_d)$ is the carrier density induced on the drain electrode. Here, we assume that the drain electrode consists of monolayer graphene, so that $n(\mu_d) = \mu_d^2/\pi(v\hbar)^2$,

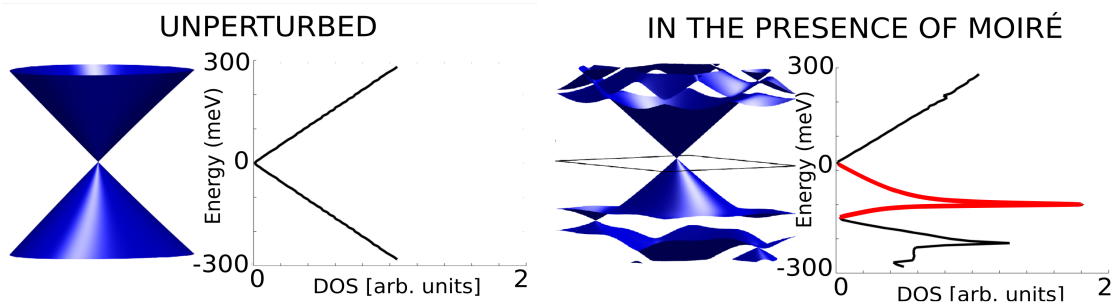

Figure 4.2: The band structure and density of states of unperturbed monolayer graphene (above) and corresponding graphene minibands and density of states of an aligned graphene/hBN heterostructure (below). The Van Hove singularity in the density of states of the heterostructure is highlighted in red. Reproduced from arXiv:1802.08100.

with $v \approx 10^6 \mathrm{ms}^{-1}$, the Fermi velocity of the graphene electrons. n_g is the carrier density introduced to the system by the back gate and is equivalent to the sum of the carrier densities of both electrodes, $-(n_s - n_d)$.

We also assume that the tunnelling barrier is made of thin hexagonal boron nitride (hBN). As a result, the large bandgap can be assumed to fairly constant in the potential window we are interested in and the transmission coefficient T in Eq. (4.1) only weakly depends on the energy of the initial state, ϵ [79, 85], thus we set it to a constant. Moreover, the hBN located in the barrier is rotated by a large angle with respect to the graphene in the source electrode, to avoid additional superlattice effects.

4.3 Highly-Aligned Graphene/hBN

We first investigate the possibility of superlattice-induced NDR for a source electrode composed of hBN (Layer 1) and monolayer graphene (Layer 2). As the perturbing effect of hBN on graphene electrons decreases with increasing misalignment between the two crystals [99, 114], we assume their crystalline axes are highly aligned. In such a case, the conical dispersion of graphene in the vicinity of the Brillouin zone (BZ) corner (valley) is folded into minibands, as indicated in Fig. 4.2, with the valence band undergoing a more significant spectral reconstruction than the conduction band [30], including the appearance of a Van Hove singularity in the DOS [30, 39, 105], shown in red in Fig. 4.2.

For a generic honeycomb substrate with a lattice constant similar to that of graphene, the perturbation of the Hamiltonian can be represented using the per-

turbation in Eq. (1.33) [30, 43]

$$\hat{\boldsymbol{H}}_{\text{Gr+Substrate}} = \hat{\boldsymbol{H}}_{\text{MLG}} + u_0 v b f_1(\boldsymbol{r}) + u_3 v b f_2(\boldsymbol{r})\sigma_3\tau_3 + u_1 v[\boldsymbol{l}_z \times \nabla f_1(\boldsymbol{r})]\cdot\boldsymbol{\sigma}\tau_3$$
$$f_1(\boldsymbol{r}) = \sum_{m=0}^{5} e^{i\boldsymbol{b_m}\cdot\boldsymbol{r}}, \quad f_2(\boldsymbol{r}) = i\sum_{m=0}^{5}(-1)^m e^{i\boldsymbol{b_m}\cdot\boldsymbol{r}},$$

where $\boldsymbol{b}_m$ represents the new reciprocal superlattice vector as before, σ and τ represent pseudospin and valley analogies to the Pauli spin matrices respectively and u_0, u_1 and u_3 are the perturbation constants. The reciprocal moiré pattern vectors b_m themselves are described by

$$\boldsymbol{b}_m = \hat{\boldsymbol{R}}_{\frac{2\pi m}{6}}\left[1 - \frac{\hat{\boldsymbol{R}}_\theta}{(1+\delta)}\right]\left(0, \frac{4\pi}{\sqrt{3}a}\right). \tag{4.3}$$

As such the reciprocal lattice vector set is primarily determined by δ the lattice constant mismatch between the two materials and θ the rotational misalignment between their crystallographic axes.

In our device, we model a rotationally-aligned, $\theta = 0°$, graphene and hexagonal boron nitride electrode in which the lattice constant mismatch is 1.8% [30]. The highly-aligned case leads to the strongest perturbation felt in the graphene sheet [114] and therefore the most profound reconstruction of the electronic states.

The exact values of the three perturbation constants $\{u_0, u_1, u_3\}$ are currently unknown, however, one such model agrees with optical absorption data [42] and sets them as $u_0 = 0.032$, $u_1 = -0.063$ and $u_3 = -0.055$ [39]. This perturbation leads to the formation of flattened bands and a secondary Dirac point, as seen in Fig. 4.2 in comparison to the purely linear bands of unmodified monolayer graphene. The important reconstruction in the density of states, involving a van Hove Singularity (vHS) around the flattened bands, is highlighted in red.

In Fig. 4.3a, we display the I-V dependence of the tunnelling current between the graphene/hBN source and graphene drain electrode as a function of the voltages V_b and V_g in a device with hBN as the barrier ($d = 13$ nm, $\tilde{\epsilon} = 3$) and a Si gate separated by insulating layer ($d_g = 180$ nm, $\epsilon = 3.9$), geometry similar to recent experiments [79, 80, 81, 104]. The appearance of NDR can be seen in the top right quadrant of Fig. 4.3a where the tunnelling current decreases with increasing bias voltage. We show select cuts through the potential space for various constant values of V_g, between 0V (orange) and 60V (black), in Fig. 4.3b.

For the standalone device, $V_b = V_g = 0$V, the chemical potentials in the source and drain are located at the respective neutrality points and are aligned with one another, as in diagram (I) in Fig. 4.3c, leading to an absence of tunnelling current.

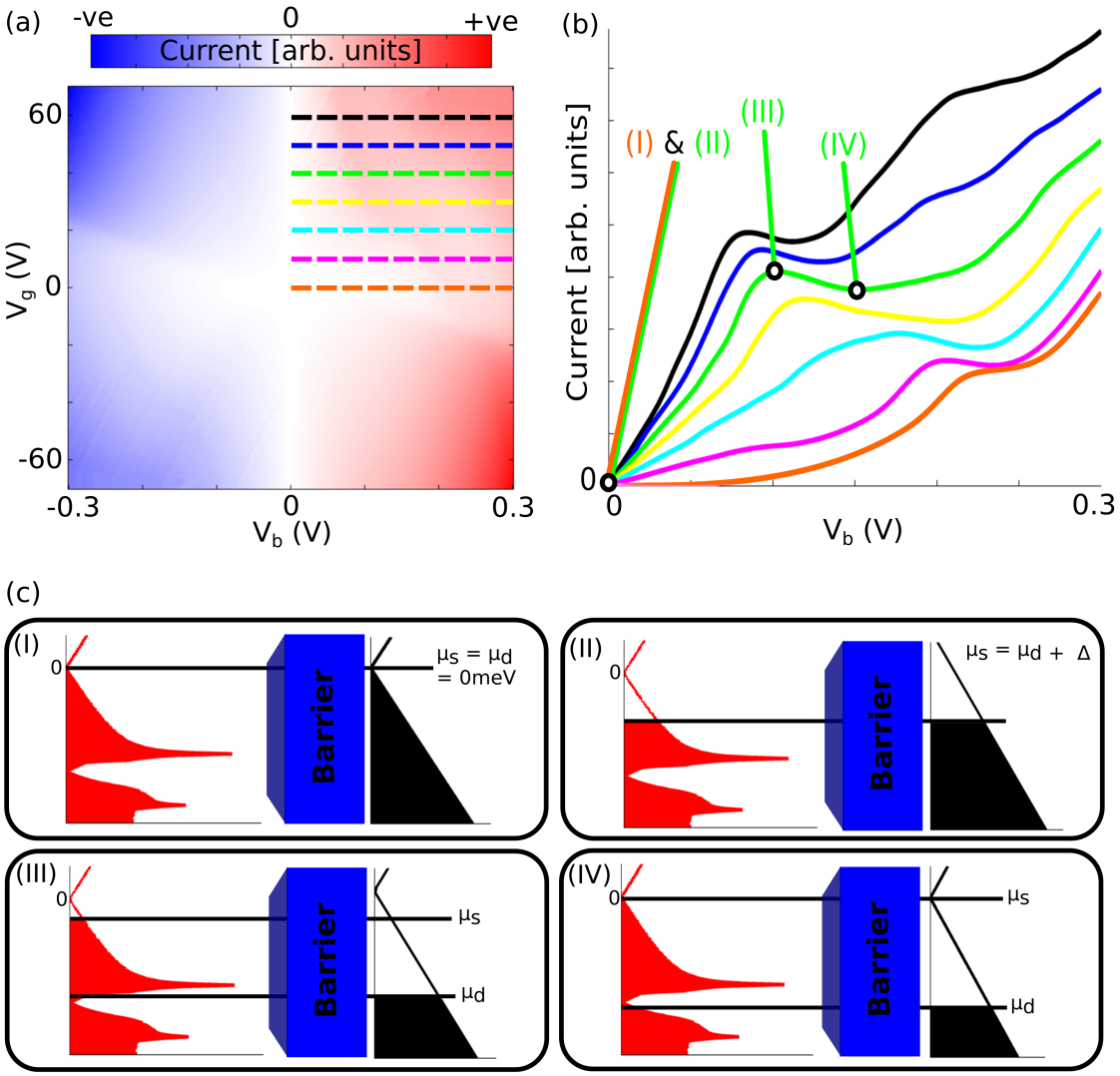

Figure 4.3: (a) Calculated tunnelling current for a tunnelling device as seen in Fig. 4.1a, as a function of voltages V_g and V_b. (b) Tunnelling current as a function of V_b for constant V_g from 0 V (orange) to 60 V (black) in steps of 10 V. The cuts in (V_g, V_b) space corresponding to current curves in (b) are shown with dashed lines in (a). (c) Diagrams showing alignment of source and drain density of states as well as the positions of chemical potentials μ_s and μ_d for points in (V_g, V_b) space corresponding to tunnelling currents marked in (I), (II), (III) and (IV) in (b). Reproduced from arXiv:1802.08100.

Applying the bias voltage introduces a relative shift between the shift and drain chemical potentials μ_s and μ_d, respectively. Meaning that an increase in V_b for $V_g = 0$V (corresponding to following the orange dashed line in Fig. 4.3a and the orange line in 4.3b) results in an increasing current as electrons from the valence band in the source can tunnel into the empty conduction band states of the drain. For V_b slightly above 0.2V, μ_d moves past the moiré-induced VHS in the source valence band that leads to a shoulder-like feature in the orange curve in Fig. 4.3b.

In contrast, applying the gate voltage V_g at constant V_b dopes source and drain without affecting the relative positions of the chemical potentials, μ_s and μ_d. As shown in diagram (II) in Fig. 2, for $V_g = 40$ V and $V_b = 0$ V no current flows through the structure because the chemical potentials are aligned, as in (I). Again, the current increases with increasing bias (as demonstrated by the green curve in Fig. 4.3b) until it reaches a peak when the occupied state in the moiré-induced VHS are aligned with empty states in the drain valence band, as in diagram (III). Because the VHS in the source DOS is followed by a dip, increasing V_b further does not lead to more occupied electronic states contributing to the tunnelling. However, because changing V_b affects the energy shift Δ between the Dirac points of the source and drain through Eq. 4.2, the number of empty states aligned with the VHS actually decreases with increasing V_b, as seen by comparing diagrams (III) and (IV). This results in a decrease of the current and therefore the presence NDR in the device.

4.4 Twisted Bilayer Graphene

We further test the robustness of this hypothesis by exploring another superlattice source electrode, comprised of twisted bilayer graphene (tBLG). tBLG comprises of two stacked and rotationally misaligned graphene sheets — in contrast the graphene/hBN electrode, this system requires a rotational misalignment of angle θ to form the superlattice as the lattice constants in the two sheets are equivalent. The effective Hamiltonian for such a system can written as

$$\hat{\boldsymbol{H}}_{\text{tBLG}} = \begin{pmatrix} \hat{\boldsymbol{H}}_{\text{MLG}}(\boldsymbol{p}, -\frac{\theta}{2}) + \frac{u}{2} & \hat{\boldsymbol{T}} \\ \hat{\boldsymbol{T}}^{\dagger} & \hat{\boldsymbol{H}}_{\text{MLG}}(\boldsymbol{p'} + \boldsymbol{\Delta K}, \frac{\theta}{2}) - \frac{u}{2} \end{pmatrix}, \tag{4.4}$$

in which the two Dirac cones are displaced by a vector $\boldsymbol{\Delta K} \approx 2|\boldsymbol{K}|\sin(\theta/2)(0,-1)$ and the coupling between the two rotated sheets is taken from Eq. (1.30)

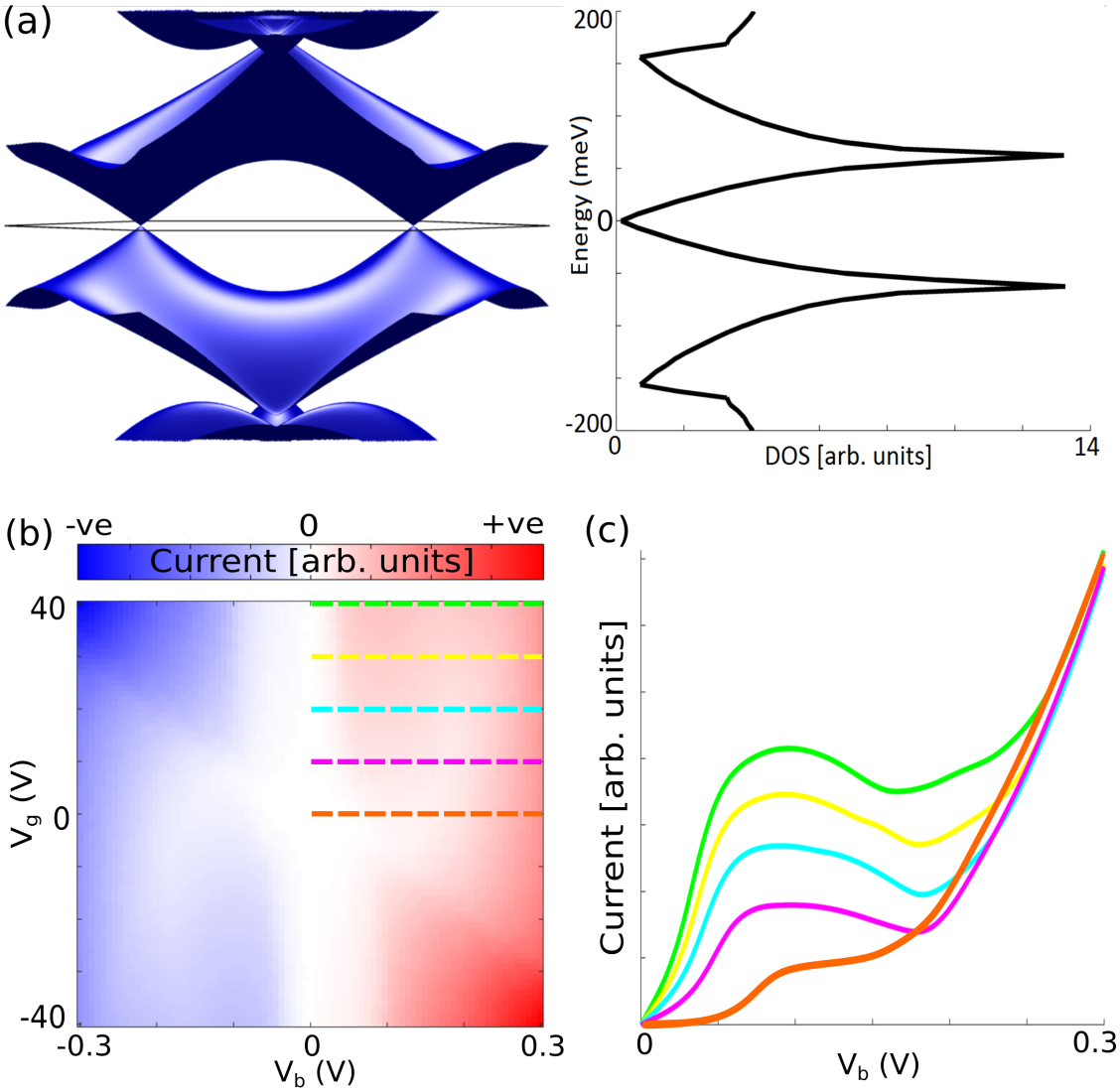

Figure 4.4: (a) Low-energy band structure and density of states for twisted bilayer graphene with a misalignment angle of 2°. Note that both the position and height of the VHS change with misalignment angle. (b) Tunnelling current for the device seen in Fig. 4.1b, as a function of gate and bias voltages V_g and V_b. (c) Tunnelling current as a function of V_b for constant V_g from 0V (orange) to 40V (green) in steps of 10V. The cuts in (V_b, V_g) space corresponding to the current curves in (c) are shown with dashed lines in (b). Reproduced from arXiv:1802.08100.

$$\hat{\boldsymbol{T}} = w \sum_{m=1}^{3} \exp(-i\boldsymbol{b}_m(\theta) \cdot \boldsymbol{r}) T_m,$$
$$T_1 = \begin{pmatrix} 1 & 1 \\ 1 & 1 \end{pmatrix}, \quad T_2 = \begin{pmatrix} e^{-i\frac{2\pi}{3}} & 1 \\ e^{i\frac{2\pi}{3}} & e^{-i\frac{2\pi}{3}} \end{pmatrix}, \quad T_3 = \begin{pmatrix} e^{i\frac{2\pi}{3}} & 1 \\ e^{-i\frac{2\pi}{3}} & e^{i\frac{2\pi}{3}} \end{pmatrix}, \tag{4.5}$$

where $w \approx 110$meV. Midway between the cones hybridisation of the two linear dispersions leads to the flattening of a miniband feature and appearance of a peak in the DOS, as shown in Fig. 4.4a. This peak has been observed by scanning tunnelling microscopy and is known to modify the optical conductivity [115, 116] and Raman spectra [117] of tBLG.

Unlike the prior definition of twisted bilayer graphene in Section 1.3.1, we have also included the presence of an external potential across the bilayer, u. In standard graphene bilayers the results in a band gap opening, proportional to the strength of the field [20]. Here, where the low-energy spectra resembles that of the linear dispersion in monolayer graphene, instead one cone is shifted up by $u/2$ and the other shifted down by $u/2$. This has the effect of flattening the density of states in that region and making it non-zero at the neutrality point. Although this directly affects the density of states of the electrode, we find the effect it has on the current flow is small in comparison to large peaks provided by the vHS.

For our modelling of the tunnelling between tBLG and graphene across a hBN multilayer, we choose the misalignment angle 2°, corresponding to the low-energy band structure in the vicinity of a single valley and density of states as shown in Fig. 4.4a. All the other geometrical parameters of the device are as used in the case of the graphene/hBN source electrode, as seen in Fig. 4.1. The calculated current as a function of the bias and gate voltages V_b and V_g is shown in Fig. 4.4b and selected cuts for constant V_g are presented in Fig. 4.4c. Similarly to the case of the graphene/hBN electrode, superlattice-induced spectral reconstruction, in particular the presence of sharp VHSs followed by a dip, leads to NDR for a range of gate voltages.

Because the VHS is a robust feature in the density of states of tBLG for a large range of misalignment angles [113], the behaviour of tunnelling current should also be similar for different θ (although note that greater misalignment angle requires higher V_g to dope the source past the singularity). Also, because, in contrast to the aligned graphene/hBN heterostructure, density of states of tBLG is electron-hole symmetric, the graph in Fig. 4.4b is inversion-symmetric with respect to the point $V_b = V_g = 0$ V.

The peak-to-valley ratio is the typical measure of the quality of an NDR system - the larger this ratio, the larger the differences seen in current flow. The devices shown in the previous two sections exhibit a low peak-to-valley ratio of roughly 1. However, as previously stated, this device setup is not limited only to variations we show. There are many possible superlattice constructs under the two main superlattice types we have discussed in this Thesis [30, 45], a number that will continue to grow as more and more 2D materials become isolated, each with their own distinct reconstruction of the graphene density of states. As such, we make no defining statement about the ideal device electrodes to use - although any reconstruction that exhibits sharp peaks and troughs in the density of states it produces, particularly when packed close to one another in energy, can be assumed to be of merit in this regard.

4.5 Summary

In conclusion, we have described a model for a vertical tunnelling device comprised of a monolayer electrode alongside an electrode that utilises a superlattice form in order to induce large peaks and troughs in the density of states and thus affect the I-V characteristics felt in the device. This includes a description of the electrostatics of the system and how the current magnitude and conductance can be tuned via the presence of a back gate, top gate and bias voltage, and, in the case of the twisted bilayer, how variation in the angle can affect these. Both exhibit current peaks followed by troughs in the I-V characteristics and negative differential resistance, in a reasonable voltage range and without the need for high-quality, momentum conserving graphene samples.

4.A Density Of States Probe

At specific 'magic' angles, lower than those previously mentioned, the lowest energy mini-band flattens and the two VHS collapse around the neutrality point [118, 119, 120, 121], constructing a single sharp peak of width $\approx$ 8meV, as seen in Fig. 4.5. Due to the large carrier densities found around neutrality point, the Fermi level of the twisted bilayer can be pinned within the VHS, $\mu_s = 0$meV. Therefore the low-energy variable setups probed by small changes in the tuning potentials tend to manifest primarily in energy and Fermi level shifts seen in the opposite electrode instead. Thus this sharp peak can be thought of as a probing state that can be used as a reference to image the DOS of the corresponding secondary electrode.

In order to achieve this, we utilise a top gate as in the device in Chap. 3 and pin the Fermi levels of our electrodes at the neutrality point, exploring the potential space that allows this. This affects only the external potential across the tBLG system u and the vertical shift of the monolayer energy spectra Δ. By setting our Fermi levels at their respective neutrality points, $\mu_s = \mu_d = 0$meV, we can recast our electrostatics to the much simpler form of

$$\begin{aligned} V_t &= \frac{ed_g}{\epsilon_0 d_0}u, \quad V_b = \frac{e}{\epsilon_0}\frac{d_g}{\epsilon}u, \\ V_g &= -\frac{1}{e}\Delta, \quad \Delta = \frac{d}{ed_0}u. \end{aligned} \tag{4.6}$$

These relations correspond to a device setup whereby changes in current occur due the vertical shifting of the monolayer spectrum, Δ, matching differing sections of the MLG DOS with the sharp peak provided by the tBLG. Provided the potential values applied vary smoothly and fit the above electrostatic approach, the change in current should vary smoothly as well. The potential constructs that move smoothly through these energy setups cannot be confined to 2D plane and instead requires matching of all three potentials. Outside of the device dimensions, it is worth noting that each potential term now depends entirely on the external potential across the twisted bilayer u. As before this external potential directly affects the band structure, however in the $\theta = 1^\circ$ case, it attempts to lift the degeneracy of the two collapsed VHS's, for instance increasing the width of the peak to 12meV when $u = 150$meV.

Fig. 4.5 displays the absolute tunnelling current magnitudes for such a setup with fixed Fermi levels and potentials that vary in the range $V_t = \pm 1.3$V, $V_g = \pm 0.1$V and $V_b = \pm 12$V, which additionally bounds $u = \pm 75$meV, keeping the

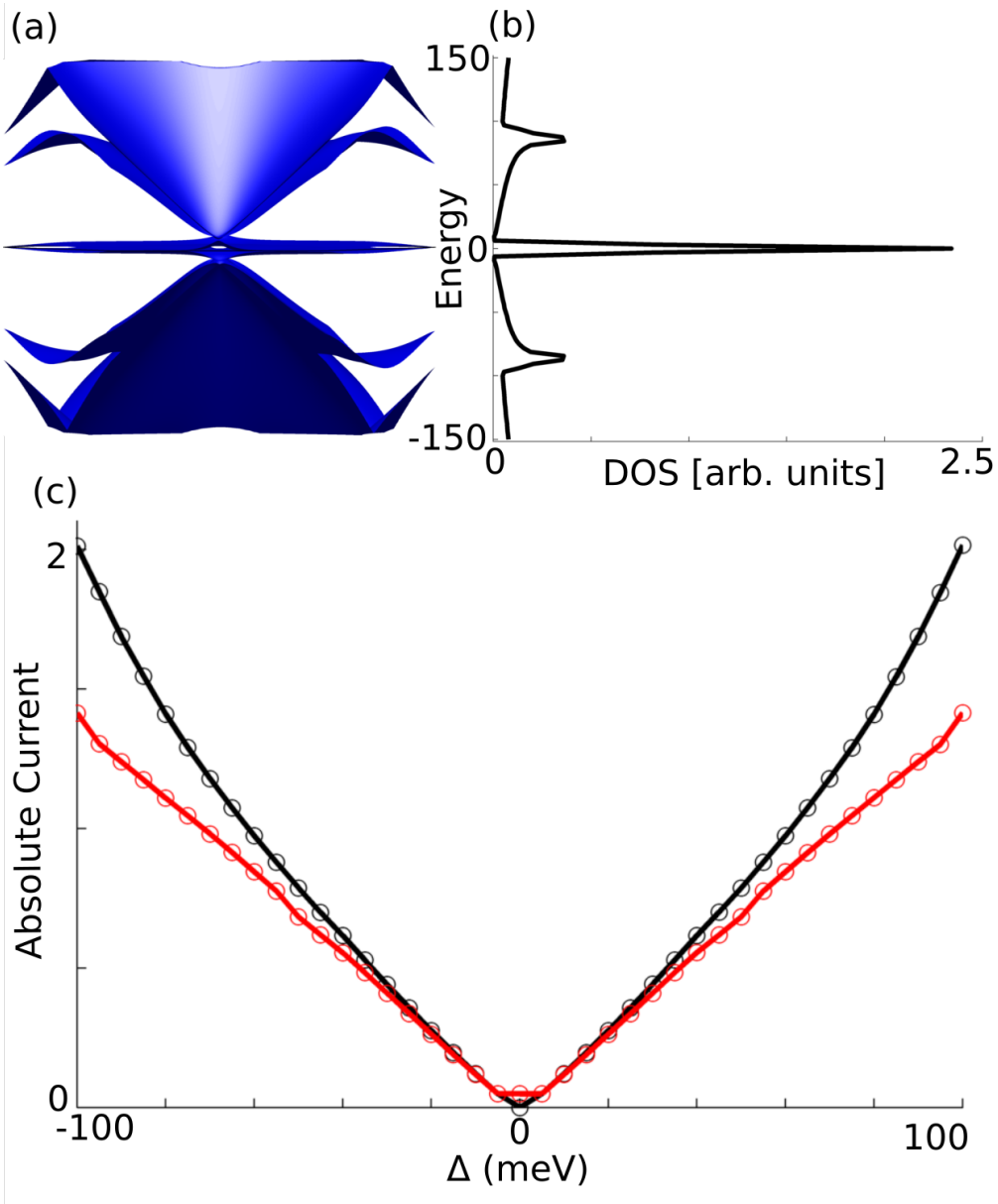

Figure 4.5: (a) Flattened band structure and (b) density of states for a twisted bilayer sheet with a misalignment angle of 1.05°. (c) The current magnitudes for varying potential setups that maps the DOS of the monolayer electrode. Black represents the results obtained with the full DOS spectra found for $\theta = 1.05°$ and red represents the idealised results found when only the initial sharp peak is used.

central peak fairly condensed. As previously mentioned, $\mu_d = 0$meV and therefore Δ represents the energy at which states are being imaged and can be directly transformed into values of the three potentials $V_{t,b,g}$ via Eq. (4.6). The black points are results obtained when the current is calculated using the full DOS spectra found in constructing the $\theta = 1.05°$ energy bands and red constitutes the 'idealised' representation, where all features outside of the initial sharp peak are nullified. Both can be seen to reconstruct the linear dependence found in the monolayer electrode, using current magnitude in place of the state density. As the current is proportional to the DOS of both electrodes, this occurs due to the large current provided in the energy range of the VHS being orders of magnitude larger than those in the immediate adjacency.

As the peak is symmetric around $E = 0$meV, the current results are also symmetric, giving direct imaging of both the conduction and valence band of the monolayer electrode. At values of $\mu_B + \Delta = 0 \rightarrow 40$meV, the two approaches are in alignment, reproducing the linearly increasing DOS we expect. Higher in energy however, they diverge due to the presence of features further out in the tBLG DOS, at around 60meV, within the energy window of interest. This may limit this approach to the 80meV range, centred around the neutrality point, penned by the secondary features seen in the DOS. Recent work however, taking into account the possibility of relaxation of the large scale moiré structures provided by low angle rotations, suggest that an AB or BA stacking is favoured where possible, centralising the sharp peak around the neutrality point, introducing band gaps and pushing higher energy features further out in energy [120]. All of which suggest an imaging DOS for the tBLG that may be effective to even higher energy values and tend toward the values plotted in red.

Additionally, we suggest that this approach should be applicable to other monolayer systems with low-energy spectra that are worthwhile analysing, as the Fermi level is always higher in energy than the magnitude of the external potential across the electrode being imaged and the electrostatics depends entirely on the device architecture and other factors that only manifest within the tBLG electrode.

Chapter 5

Summary

Throughout this thesis, we have proposed and explored the properties of a selection of vertically-stacked van der Waals heterostructures that focus on the exploitation of various graphene-based bilayers and the features that those devices produce. Chapter 2 is based on the construction of a simple graphene and substrate system, in which the graphene is perturbed by the presence of the almost commensurate periodicity of the underlying substrate. A monolayer graphene sheet placed onto one of these almost commensurate $\sqrt{3} \times \sqrt{3}$ substrates exhibits gaps between the first and second minibands, whilst maintaining the gapless linear dispersion around the neutrality point [45]. However, we choose to position bilayer graphene onto the substrate and can therefore take advantage of the band gap opening around the neutrality point, under the presence of an external potential across the system [35]. The combination of these two effects can result in a doubly gapped energy spectra that isolates a single miniband to a slim region of energies. Though we focus primarily on one such substrate, defining the parameters of our superlattice periodicity, we seek to make broad statements concerning the effects of the perturbation, understanding that we can vary the value of the external potential across such a system. As such, the isolation of new monolayers with the rough periodicity we require [122] is still of interest when considering the construction of such a device.

Chapter 3 discussed the construction of a tunnelling transistor device, in which two graphene electrodes are separated by a hexagonal boron nitride insulating barrier, through which electrons can be encouraged to tunnel through via an asymmetry in the Fermi levels of each electrode. We make this distinct from similar devices [77] by utilising a bilayer electrode and placing the system within a perpendicular magnetic field, in order to quantise the energy bands. It is again this inclusion of a bilayer graphene system that gives this our device its most distinct properties - the ability to polarise the tunnelling current by valley. This occurs due to a combination of a valley-layer polarisation at low-energies and momentum/Landau level index conserving interactions at higher energies.

Finally, Chapter 4 sought to combine both the tunnelling device structure with the manipulative properties of superlattice structures by suggesting a device in which one of the electrodes was instead swapped by some superlattice bilayer. We focused primarily on two of the simplest superlattices; monolayer graphene on hexagonal boron nitride and twisted bilayer graphene. The larger-scale periodicity arises in the first case due an inherent mismatch in the lattice constants of the two materials, whereas it arises in the second due to a rotational misalignment between the two graphene layers. However, again the statement made was general - superlattices tend to fold and restructure the energy bands of a material and

introduce regions of flattening and gaps, resulting in a density of states that is much less smooth and prone to regions of intense peaks (within the flattened bands) and troughs (within the gapped regions). We also make allowances for grown samples, that may be made larger than their exfoliated counterparts but are of a lesser quality [94], in order to build the system and construct a tunnelling device that is more dependent on the density of states of either electrode. Therefore negative differential resistance, in which an increased potential across the system leads to a decrease in current due to the large changes in the density of states within a small region of energy, can be expected for many of these superlattice electrodes. For instance, a device such as the one focused on in Chapter 2, would make for an exemplary electrode within this regime. Alternatively, a system comprised of two superlattice-reconstructed electrodes may allow for additive overlap on the density of states peaks and an even more pronounced region of NDR.

Due to the open-ended nature of the research project, the extending family of 2D atomic crystals and the large number of devices already suggested [25], this work, in terms of designable devices, could be extended in many directions. However, a few key areas of expansion could be highlighted in order to build upon some of the key tenants that were promised by early graphene research. Designable heterostructures were a key component of the graphene roadmap [25] and so further inclusion of more exotic 2D atomic crystals should be a priority. As isolation and synthesis techniques improve, we can expect these materials to become as easily produceable as graphene currently is and, as such, the exploitation of features of graphene analogues such as the corrugated structure of silicene [123] or the hydrogen-terminated surface of germanane [124] become increasingly more feasible. This is not to mention the large family of two-dimensional transition metal dichalcogenides that we only use sparingly in this thesis, but many of which have already found use in flexible electronic, spintronic and optoelectronic devices [125].

Additionally, one reoccurring feature throughout this thesis is the dependence of the intrinsic lattice constants of each layer involved. We discuss the many options we have in terms of materials to provide a lattice constant, however we ignore the possibility of simply straining a material in order to dynamically change this value. Graphene itself is able to sustain a reversible tensile strain of up to 25% [126] - for comparison silicon is only able to sustain this up to 1.5%. Under a uniaxial strain, this shifts the position of the Dirac cones in the BZ, however precise biaxial strain would allow us to retain the hexagonal periodicity that we value in graphene, for use in superlattice construction. This biaxial strain also retains much of the conical band structure we know, with a reconstruction of the

Fermi velocity and therefore band gradient [127], and should therefore allow for designable superlattices whereby we open mini-gaps and flatten bands in chosen energy regions depending on the lattice mismatch, now given by a combination of intrinsic lattice constants and the strain applied.

Finally, the flexibility of graphene and other 2D materials is something that is always stressed when discussing their applications. Therefore, further investigation into the effects of folding, extending as far as folding graphene back onto itself and accounting for folding point and direction of folding lines, and how this affects the graphene band structure could provide valuable insight into how these devices would be affected in use [128]. Practically, we can assume that the devices we are interested in should not be folded such that their layers now lie on top of one another under reasonable use, however folding of stacked heterostructures may allow for tighter packing in a regime where we are only a handful of atoms thick vertically and effectively infinitely large in the x-y plane. Understanding of how tightly a device may be packed via folding, whilst maintaining separations that mean that multiple layers of the device do not interfere with one another is a valid line of questioning. Outside of this, the exploitation of folded structures such as carbon nanoscrolls [129] within van der Waals heterostructure construction may begin to further bridge the gap between graphene devices and the incorporation and use of other carbon allotropes such as carbon nanotubes and Buckyballs.

Bibliography

[1] Hull, A. W. *Phys. Rev.* **10**, 661 (1917).

[2] Bernal, J. D. *Proc. Royal Soc. A* **106**, 749 (1924).

[3] Wallace, P. R. *Phys. Rev.* **71**, 622 – 634 (1947).

[4] McClure, J. W. *Phys. Rev.* **108**, 612 – 618 (1957).

[5] Slonczewski, J. C. and Weiss, P. R. *Phys. Rev.* **109**, 272 – 279 (1957).

[6] Fradkin, E. *Phys. Rev. B* **33**, 3263 – 3268 (1986).

[7] Kroto, H. W., Heath, J. R., O'Brien, S. C., Curl, R. F., and Smalley, R. E. *Phys. Rev. B* **91**, 1213 – 1235 (1991).

[8] Iijima, S. *Phys. Rev. B* **354**, 56 – 58 (1991).

[9] Novoselov, K., Geim, A. K., Morozov, S. V., Jiang, D., Dubunos, S. V., Grigorieva, I. V., and Firsov, A. A. *Science* **306**, 666 – 669 (2004).

[10] Novoselov, K. S., Jiang, D., Schedin, F., Booth, T. J., Khotkevich, V. V., Morozov, S. V., and Geim, A. K. *Proc. Natl Acad. Sci. USA* **102**, 10451 – 10453 (2005).

[11] Lee, C., Wei, X. D., Kyser, J. W., and Hone, J. *Science* **321**, 385 – 388 (2008).

[12] Nair, R. R., Blake, P., Grigorenko, A. N., Novoselov, K. S., Booth, T. J., Stauber, T., Peres, N. M. R., and Geim, A. K. *Science* **320**, 1308 – 1308 (2008).

[13] Dean, C. R., Young, A. F., Meric, I., Lee, C., Wang, L., Sorgenfrei, S., Watanabe, K., Taniguchi, T., Kim, P., Shepard, K. L., and Hone, J. *Nat. Nano.* **5**, 722 – 726 (2010).

[14] Splendiani, A., Sun, L., Zhang, Y. B., Li, T. S., Kim, J., Chim, C. Y., Galli, G., and Wang, F. *Nano Lett.* **10**, 1271 – 1275 (2010).

[15] Kuc, A., Zibouche, N., and Heine, T. *Phys. Rev. B* **83**, 245213 (2011).

[16] Guzman-Verri, G. G. and Voon, L. C. L. Y. *Phys. Rev. B* **76**, 075131 (2007).

[17] McCann, E. and Fal'ko, V. I. *Phys. Rev. Lett.* **96**, 086805 (2006).

[18] Ohta, T., Bostwick, A., Seyller, T., Horn, K., and Rotenberg, E. *Science* **313**, 951 – 954 (2006).

[19] Zhang, Y. Y., Wang, C. M., Cheng, Y., and Xiang, Y. *Carbon* **48**, 4511 – 4517 (2011).

[20] Zhang, Y. B., Tang, T. T., Girit, C., Hao, Z., Martin, M. C., Zettl, A., Crommie, M. F., Shen, Y. R., and Wang, F. *Phys. Rev. Lett.* **459**, 820 – 823 (2009).

[21] Zhou, S. Y., Gweon, G. H., Fedorov, A. V., First, P. N., Heer, W. A. D., Lee, D. H., Guinea, F., Neto, A. H. C., and Lanzara, A. *Nat. Mat.* **6**, 770 – 775 (2007).

[22] Novoselov, K. S., McCann, E., Morozov, S. V., Fal'ko, V. I., Katsnelson, M. I., Zeitler, U., Jiang, D., Schedin, F., and Geim, A. K. *Nat. Phys.* **2**, 177 – 180 (2006).

[23] Feldman, B. E., Martin, J., and Yacoby, A. *Nat. Phys.* **5**, 889 – 893 (2009).

[24] Geim, A. K. and Grigorieva, I. V. *Nature* **499**, 419 – 425 (2013).

[25] Novoselov, K. S., Fal'ko, V. I., Colombo, L., Gellert, P. R., Schwab, M. G., and Kim, K. *Nature* **490**, 192 – 200 (2013).

[26] Hwang, E. H., Adam, S., and Sarma, S. D. *Phys. Rev. Lett.* **98**, 186806 (2007).

[27] Ishigami, M., Chen, J. H., Cullen, W. G., Fuhrer, M. S., and Williams, E. D. *Nano Lett.* **7**, 1643 – 1648 (2007).

[28] Ortix, C., Yang, L. P., and van den Brink, J. *Phys. Rev. B* **86**, 081405 (2012).

[29] Kindermann, M., Uchoa, B., and Miller, D. L. *Phys. Rev. B* **86**, 115415 (2012).

[30] Wallbank, J. R., Patel, A. A., Mucha-Kruczyński, M., Geim, A. K., and Fal'ko, V. I. *Phys. Rev. B* **87**, 245408 (2013).

[31] Saito, R., Dresselhaus, G., and Dresselhaus, M. *Physical properties of carbon nanotubes*. Imperial College Press, London, (1998).

[32] McCann, E. and Koshino, M. *Rep. Prog. Phys* **76**, 056503 (2013).

[33] Gava, P., Lazzeri, M., Saitta, A. M., and Mauri, F. *Phys. Rev. B* **79**, 165431 (2009).

[34] Chung, D. D. L. *Jour. Mat. Sci.* **37**, 1475 – 1489 (2002).

[35] McCann, E. *Phys. Rev. B* **74**, 161403 (2006).

[36] Park, C., Ryou, J., Hong, S., Sumpter, B. G., Kim, G., and Yoon, M. *Phys. Rev. Lett.* **115**, 015502 (2015).

[37] Ashcroft, N. W. and Mermin, N. D. *Solid state physics*. Holt, Rinehart and Winston, London, (1977).

[38] Bistritzer, R. and MacDonald, A. H. *Proc. Nat. Acad. Sci* **108**, 12233 – 12237 (2011).

[39] Mucha-Kruczyński, M., Wallbank, J. R., and Fal'ko, V. I. *Phys. Rev. B* **93**, 085409 (2016).

[40] Wallbank, J. R., Patel, A. A., Mucha-Kruczyński, M., Geim, A. K., and Fal'ko, V. I. *Phys. Rev. B* **87**, 245408 (2013).

[41] Kubota, Y., Watanabe, K., Tsuda, O., and Taniguchi, T. *Science* **317**, 932 – 934 (2007).

[42] Shi, Z. W., Jin, C. H., Yang, W., Ju, L., Horng, J., Lu, X. B., Bechtel, H. A., Martin, M. C., Fu, D. Y., Wu, J. Q., Watanabe, K., Taniguchi, T., Zhang, Y. B., Bai, X. D., Wang, E. G., Zhang, G. Y., and Wang, F. *Phys. Rev. B* **93**, 085409 (2016).

[43] Mucha-Kruczyński, M., Wallbank, J. R., and Fal'ko, V. I. *Phys. Rev. B* **88**, 205418 (2013).

[44] Farjam, M. and Rafii-Tabar, H. *Phys. Rev. B* **79**, 045417 (2009).

[45] Wallbank, J. R., Mucha-Kruczyński, M., and Fal'ko, V. I. *Phys. Rev. B* **88**, 155415 (2013).

[46] Leech, D. J. and Mucha-Kruczyński, M. *Phys. Rev. B* **94**, 165437 (2016).

[47] Esaki, L. and Tsu, R. *IBM Jour. of Res. and Dev.* **14**, 61 (1970).

[48] Tsu, R. *Superlattice to Nanoelectronics.* Elsevier Science, Amsterdam, (2011).

[49] Park, C. H., Yang, L., Son, Y. W., Cohen, M. L., and Louie, S. G. *Phys. Rev. Lett.* **101**, 126804 (2008).

[50] Barbier, M., Vasilopoulos, P., and Peeters, F. M. *Phys. Rev. B* **81**, 075438 (2010).

[51] Killi, M., Wu, S., and Paramekanti, A. *Phys. Rev. Lett.* **107**, 086801 (2011).

[52] Burset, P., Yeyati, A. L., Brey, L., and Fertig, H. A. *Phys. Rev. B* **83**, 195434 (2011).

[53] Tan, L. Z., Park, C. H., and Louie, S. G. *Nano Lett.* **11**, 2596 – 2600 (2011).

[54] Dubey, S., Singh, V., Bhat, A. K., Parikh, P., Grover, S., Sensarma, R., Tripathi, V., Sengupta, K., and Deshmukh, M. M. *Nat. Mater.* **13**, 3990 – 3995 (2013).

[55] Xue, J., Sanchez-Yamagishi, J., Bulmash, D., Jacquod, P., Dashpande, A., Watanabe, K., Taniguchi, T., Jarillo-Herrero, P., and LeRoy, B. J. *Nat. Mater.* **10**, 282 – 285 (2011).

[56] Pletikosic, I., Kralj, M., Pervan, P., Brako, R., Coraux, J., N'Diaye, A. T., Busse, C., and Michely, T. *Phys. Rev. Lett.* **102**, 056808 (2009).

[57] Martoccia, D., Willmott, P. R., Brugger, T., Bjorck, M., Gunther, S., Schleputz, C. M., Cervellino, A., Pauli, S. A., Patterson, B. D., Marchini, S., Wintterlin, J., Moritz, W., and Greber, T. *Phys. Rev. Lett.* **101**, 126102 (2008).

[58] Ponomarenko, L. A., Gorbachev, R. V., Yu, G. L., Elias, D. C., Jalil, R., Patel, A. A., Mishchenko, A., Mayorov, A. S., Woods, C. R., Wallbank, J. R., Mucha-Kruczyński, M., Piot, B. A., Potemski, M., Grigorieva, I. V., Novoselov, K. S., Guinea, F., Fal'ko, V. I., and Geim, A. K. *Nature* **497**, 594 – 597 (2013).

[59] Hunt, B., Sanchez-Yamagishi, J. D., Young, A. F., Yankowitz, M., LeRoy, B. J., Watanabe, K., Taniguchi, T., Moon, P., Koshino, M., Jarillo-Herrero, P., and Ashoori, R. C. *Science* **340**, 1427 – 1430 (2013).

[60] Dean, C. R., Wang, L., Maher, P., Forsythe, C., Ghahari, F., Gao, Y., Katoch, J., Ishigami, M., Moon, P., Koshino, M., Taniguchi, T., Watanabe, K., Shepard, K. L., Hone, J., and Kim, P. *Nature* **497**, 598 – 602 (2013).

[61] Gorbachev, R. V., Song, J. C. W., Yu, G. L., Kretinin, A. V., Withers, F., Cao, Y., Mishchenko, A., Grigorieva, I. V., Novoselov, K. S., Levitov, L. S., and Geim, A. K. *Science* **346**, 448 – 451 (2014).

[62] Wallbank, J. R., Mucha-Kruczyński, M., Chen, X., and Fal'ko, V. I. *Annalen Der Physik* **527**, 359 – 376 (2015).

[63] Cheianov, V. V., Fal'ko, V. I., Syljuasen, O., and Altshuler, B. L. *Sol. St. Comm.* **149**, 1499 – 1501 (2009).

[64] Giovannetti, G., Capone, M., van den Brink, J., and Ortix, C. *Phys. Rev. B* **91**, 121417 (2015).

[65] Ren, Y., Deng, X., Qiao, Z., Li, C., Jung, J., Zeng, C., Zhang, Z., and Niu, Q. *Phys. Rev. B* **91**, 245415 (2015).

[66] Venderbos, J. W. F., Manzardo, M., Efremov, D. V., van den Brink, J., and Ortix, C. *Phys. Rev. B* **93**, 045428 (2016).

[67] Castro, E. V., Novoselov, K. S., Morozov, S. V., Peres, N. M. R., Santos, J. M. B. L. D., Nilsson, J., Guinea, F., Geim, A. K., and Neto, A. H. C. *Phys. Rev. Lett.* **99**, 216802 (2007).

[68] Eisberg, R. and Resnick, E. *Quantum Physics of Atoms, Molecules, Solids, Nuclei and Particles.* John Wiley and Sons, (1985).

[69] Jiang, Z., Henriksen, E. A., Tung, L. C., Wang, Y. J., Schwartz, M. E., Han, M. Y., Kim, P., and Stormer, H. L. *Phys. Rev. Lett.* **98**, 197403 (2007).

[70] Kuzmenko, A. B., Crassee, I., van der Marel, D., Blake, P., and Novoselov, K. S. *Phys. Rev. B* **80**, 165406 (2009).

[71] Schrieffer, J. R. and Wolff, P. A. *Phys. Rev.* **149**, 491 (1966).

[72] Zolyomi, V., Drummond, N. D., and Fal'ko, V. I. *Phys. Rev. B* **89**, 205416 (2014).

[73] dos Santos, J. M. B. L., Peres, N. M. R., and Neto, A. H. C. *Phys. Rev. Lett.* **99**, 256802 (2007).

[74] Shallcross, S., Sharma, S., Kandelaki, E., and Pankratov, O. A. *Phys. Rev. B* **81**, 165105 (2010).

[75] Madelung, O. *Semiconductors: Group IV Elements and III-V Compounds.* Springer Verlag, Berlin, (1991).

[76] Zolyomi, V., Drummond, N. D., and Fal'ko, V. I. *Phys. Rev. B* **87**, 195403 (2013).

[77] Britnell, L., Gorbachev, R. V., Jalil, R., Belle, B. D., Schedin, F., Katnelson, M. I., Eaves, L., Morozov, S. V., Mayorov, A. S., Peres, N. M. R., Neto, A. H. C., Leist, J., Geim, A. K., Ponomarenko, L. A., and Novoselov, K. S. *Nano Lett.* **12**, 1707 – 1710 (2012).

[78] Feenstra, R. M., Jena, D., and Gu, G. *Jour. App. Phys.* **111** (2012).

[79] Britnell, L., Gorbachev, R. V., Jalil, R., Belle, B. D., Schedin, F., Mishchenko, A., Georgiou, T., Katnelson, M. I., Eaves, L., Morozov, S. V., Peres, N. M. R., Leist, J., Geim, A. K., Novoselov, K. S., and Ponomarenko, L. A. *Science* **335**, 947 – 950 (2012).

[80] Britnell, L., Gorbachev, R. V., Geim, A. K., Ponomarenko, L. A., Mishchenko, A., Greenaway, M. T., Fromhold, T. M., Novoselov, K. S., and Eaves, L. *Nat. Comms.* **4**, 1794 (2013).

[81] Mishchenko, A., Tu, J. S., Cao, Y., Gorbachev, R. V., Wallbank, J. R., Greenaway, M. T., Morozov, V. E., Morozov, S. V., Zhu, M. J., Wong, S. L., Withers, F., Woods, C. R., Kim, Y. J., Watanabe, K., Taniguchi, T., Vdovin, E. E., Makarovsky, O., Fromhold, T. M., Fal'ko, V. I., Geim, A. K., Eaves, L., and Novoselov, K. S. *Nat. Comms.* **9**, 808 – 813 (2014).

[82] Greenaway, M. T., Vdovin, E. E., Mishchenko, A., Makarovsky, O., Patane, A., Wallbank, J. R., Cao, Y., Kretinin, A. V., Zhu, M. J., Morozov, S. V., Fal'ko, V. I., Novoselov, K. S., Geim, A. K., Fromhold, T. M., and Eaves, L. *Nat. Phys.* **11**, 1057 – 1062 (2015).

[83] Fallahazad, B., Lee, K., Kang, S., Xue, J. M., Larentis, S., Corbet, C., Kim, K., Movva, H. C. P., Taniguchi, T., Watanabe, K., Register, L. F., Banarjee, S. K., and Tutuc, E. *Nat. Lett.* **15**, 428 – 433 (2015).

[84] Kang, S., Fallahazad, B., Lee, K., Movva, H., Kim, K., Corbet, C. M., Taniguchi, T., Watanabe, K., Colombo, L., Register, L. F., Tutuc, E., and Banerjee, S. K. *IEEE Elec. Dev. Lett.* **36**, 405 – 407 (2015).

[85] Georgiou, T., Jalil, R., Belle, B. D., Britnell, L., Gorbachev, R. V., Morozov, S. V., Kim, Y. J., Gholinia, A., Haigh, S. J., Makarovsky, O., Eaves, L., Ponomarenko, L. A., Geim, A. K., Novoselov, K. S., and Mishchenko, A. *IEEE Elec. Dev. Lett.* **8**, 100 – 103 (2013).

[86] Wallbank, J. R., Ghazaryan, D., Misra, A., Cao, Y., Tu, J. S., Piot, B. A., Potemski, M., Pezzini, S., Wiedmann, S., Zeitler, U., Lane, T. L. M., Morozov, S. V., Greenaway, M. T., Eaves, L., Geim, A. K., Fal'ko, V. I., Novoselov, K. S., and Mishchenko, A. *Science* **353**, 575 – 579 (2016).

[87] Xiao, D., Yao, W., and Niu, Q. *Phys. Rev. Lett.* **99** (2007).

[88] Rycerz, A., Tworzydlo, J., and Beenakker, C. W. J. *Nat. Phys.* **3**, 172 – 175 (2007).

[89] Shimazaki, Y., Yamamoto, M., Borzenets, I. V., Watanabe, K., Taniguchi, T., and Tarucha, S. *Nat. Phys.* **11**, 1032 (2015).

[90] Gunlycke, D. and White, C. T. *Phys. Rev. Lett.* **106**, 136806 (2011).

[91] Lane, T. L. M., Wallbank, J. R., and Fal'ko, V. I. *Appl. Phys. Lett.* **107**, 203506 (2015).

[92] Novoselov, K. S., Geim, A. K., Morozov, S. V., Jiang, D., Katnelson, M. I., Grigorieva, I. V., Dubonos, S. V., and Firsov, A. A. *Nature* **438**, 197–200 (2005).

[93] Zhang, Y. B., Tan, Y. W., Stormer, H. L., and Kim, P. *Nature* **438**, 201–204 (2005).

[94] Roy, T., Liu, L., de la Barrera, S., Chakrabarti, B., Hesabi, Z. R., Joiner, C. A., Feenstra, R. M., Gu, G., and Vogel, E. M. *Appl. Phys. Lett.* **104**, 123506 (2014).

[95] Friedman, A. L., van't Erve, O. M. J., Li, C. H., Robinson, J. T., and Jonker, B. T. *Nat. Comm.* **5**, 3161 (2014).

[96] Friedman, A. L., van't Erve, O. M. J., Li, C. H., Robinson, J. T., and Jonker, B. T. *AIP Adv.* **6**, 056301 (2016).

[97] Gradshteyn, I. S., Ryzhik, I. M., Jeffery, A., and Zwillinger, D. *Table of integrals, series and products*. Oxford : Academic, (2007).

[98] Scheunert, G., Heinonen, O., Hardeman, R., Lapicki, A., Gubbins, M., and Bowman, R. M. *App. Phys. Rev.* **3**, 011301 (2016).

[99] Yankowitz, M., Xue, J. M., Cormode, D., Sanchaz-Yamagishi, J. D., Watanabe, K., Taniguchi, T., Jarillo-Herrero, P., Jacquod, P., and LeRoy, B. J. *Nat. Phys.* **8**, 382–386 (2012).

[100] Hass, J., Varchon, F., Millan-Otoya, J. E., Sprinkle, M., Heer, W. A. D., Berger, C., First, P. N., Magaud, L., and Conrad, E. H. *Phys. Rev. Lett.* **100**, 125504 (2008).

[101] Esaki, L. *Phys. Rev.* **109**, 603–604 (1958).

[102] Kim, K., Yankowitz, M., Fallahazad, B., Kang, S., Movva, H. C. P., Huang, S. Q., Larentis, S., Corbet, C. M., Taniguchi, T., Watanabe, K., Banerjee, S. K., LeRoy, B. J., and Tutuc, E. *Nano Lett.* **16**, 1989–1995 (2016).

[103] Haigh, S. J., Gholinia, A., Jalil, R., Romani, S., Britnell, L., Elias, D. C., Novoselov, K. S., Ponomarenko, L. A., Geim, A. K., and Gorbachev, R. *Nat. Mat.* **11**, 764–767 (2012).

[104] Lee, S. H., Choi, M. S., Lee, J., Ra, C. H., Liu, X., Hwang, E., Choi, J. H., Zhong, J. Q., Chen, W., and Yoo, W. J. *Appl. Phys. Lett.* **104**, 053103 (2014).

[105] Wang, E. Y., Lu, X. B., Ding, S. J., Yao, W., Yan, M. Z., Wan, G. L., Deng, K., Wang, S. P., Chen, G. R., Ma, L. G., Jung, J., Fedorov, A. V., Zhang, Y. B., Zhang, G. Y., and Zhou, S. Y. *Nat. Phys.* **12**, 1111 (2016).

[106] Yang, W., Lu, X., Chen, G., Wu, S., Xie, G. B., Cheng, M., Wang, D. M., Yang, R., Shi, D. X., Watanabe, K., Taniguchi, T., Voisin, C., Placais, B., Zhang, Y. B., and Zhang, G. Y. *Nano Lett.* **16**, 2387–2392 (2016).

[107] Li, G. H., Luican, A., dos Santos, J. M. B. L., Neto, A. H. C., Reina, A., Kong, J., and Andrei, E. Y. *Nat. Phys.* **6**, 109–113 (2010).

[108] Yan, W., Liu, M. X., Dou, R. F., Meng, L., Feng, L., Chu, Z. D., Zhang, Y. F., Liu, Z. F., Nie, J. C., and He, L. *Phys. Rev. Lett.* **109**, 126801 (2012).

[109] Tan, Z. J., Yin, J., Chen, C., Wang, H., Lin, L., Sun, L. Z., Wu, J. X., Sun, X., Yang, H. F., Chen, Y. L., Peng, H. L., and Liu, Z. F. *ACS Nano* **10**, 6725–6730 (2016).

[110] Kim, Y., Herlinger, P., Moon, P., Koshino, M., Taniguchi, T., Watanabe, K., and Smet, J. H. *ACS Nano* **16**, 5053–5059 (2016).

[111] Pierucci, D., Henck, H., Avila, J., Balan, A., Naylor, C. H., Patriarche, G., Dappe, Y. J., Silly, M. G., Sirotti, F., Johnson, A. T. C., Asensio, M. C., and Ouerghi, A. *Nano Lett.* **16**, 4054–4061 (2016).

[112] Koren, E., Leven, I., Lortscher, E., Knoll, A., Hod, O., and Duerig, U. *Nat. Nano.* **11**, 752–757 (2016).

[113] Brihuega, I., Mallet, P., Gonzalez-Herrero, H., de Laissardiere, G. T., Ugeda, M. M., Magaud, L., Gomez-Rodriguez, J. M., Yndurain, F., and Veuillen, J. Y. *Phys. Rev. Lett.* **109**, 196802 (2012).

[114] Jung, J., Laksono, E., DaSilva, A. M., MacDonald, A. H., Mucha-Kruczyński, M., and Adam, S. *Phys. Rev. B* **96**, 085442 (2017).

[115] Robinson, J. T., Schmucker, S. W., Diaconescu, C. B., Long, J. P., Culbertson, J. C., Ohta, T., Friedman, A. L., and Beechem, T. E. *ACS Nano* **7**, 637–644 (2013).

[116] Campos-Delgado, J., Algara-Siller, G., Santos, C. N., Kaiser, U., and Raskin, J. P. *Small* **9**, 3247–3251 (2013).

[117] Kim, K., Coh, S., Tan, L. Z., Regen, W., Yuk, J. M., Chatterjee, E., Crommie, M. F., Cohen, M. L., Louie, S. G., and Zettl, A. *Phys. Rev. Lett.* **108**, 246103 (2012).

[118] Bistritzer, R. and MacDonald, A. H. *Proc. Nat. Acad. Sci. USA* **108**, 12233–12237 (2011).

[119] Morell, E. S., Correa, J. D., Vargas, P., Pacheco, M., and Barticevic, Z. *Phys. Rev. B* **82**, 121407 (2010).

[120] Nam, N. N. T. and Koshino, M. *Phys. Rev. B* **96**, 075311 (2017).

[121] Kim, K., DaSilva, A., Huang, S., Fallahazad, B., Larentis, S., Taniguchi, T., Watanabe, K., LeRoy, B. J., MacDonald, A. H., and Tutuc, E. *Proc. Nat. Acad. Sci. USA* **114**, 3364 (2017).

[122] Bae, C. J., McMahon, J., Detz, H., Strasser, G., Park, J., Einarsson, E., and Eason, D. B. *AIP Adv.* **7**, 035113 (2017).

[123] Oughaddou, H., Enriquez, H., Tchalala, M. R., Yildirim, H., Mayne, A. J., Bendounan, A., Dujardin, G., Ali, M. A., and Kara, A. *Prog. In Surf. Sci.* **90**, 46–83 (2015).

[124] Bianco, E., Butler, S., Jiang, S. S., Restrepo, O. D., Windl, W., and Goldberger, J. E. *ACS Nano* **7**, 4414–4421 (2013).

[125] Manzeli, S., Ovchinnikov, D., Pasquier, D., Yazyev, O. V., and Kis, A. *Nat. Rev. Mat.* **2** (2017).

[126] Si, C., Sun, Z. M., and Liu, F. *Nanoscale* **8**, 3207–3217 (2016).

[127] Choi, S. M., Jhi, S. H., and Son, Y. W. *Phys. Rev. B* **81**, 081407 (2010).

[128] Kim, K., Lee, Z., Maline, B. D., Chan, K. T., Aleman, B., Regan, W., Gannett, W., Crommie, M. F., Cohen, M. L., and Zettl, A. *Phys. Rev. B* **83**, 245433 (2011).

[129] Xie, X., Ju, L., Feng, X. F., Sun, Y. H., Zhou, R. F., Liu, K., Fan, S. S., Li, Q. L., and Jiang, K. L. *Nano Lett.* **9**, 2565–2570 (2009).